Spring 5-17-2010

Chasing Shadows in the Outer Solar System

Federica Bianco
University of Pennsylvania, biancof@sas.upenn.edu

Chasing Shadows in the Outer Solar System

Abstract
The characteristics of the populations of objects that inhabit the outer solar system carry the fingerprint of the processes that governed the formation and evolution of the solar system. Occultation surveys push the limit of observation into the very small and distant outer solar system objects, allowing us to set constraints on the structure of the Kuiper belt, Scattered disk and Sedna populations. I collected, reduced, and analyzed vast datasets looking for occultations of stars by outer solar system objects, both working with the Taiwanese American Occultation Survey (TAOS) collaboration and leading the MMT/Megacam occultation effort. Having found no such events in my data, I was able to place upper limits on the Kuiper belt, scattered disk and Sedna population. These limits and their derivation are described here.

Degree Type
Dissertation

Degree Name
Doctor of Philosophy (PhD)

Graduate Group
Physics & Astronomy

First Advisor
Charles R. Alcock

Second Advisor
Pavlos Protopapas

Third Advisor
Matthew Lehner

Keywords
Solar System, Kuiper Belt, Sedna, Occultations, Fresnel Diffraction, Fast Photometry

Subject Categories
Astrophysics and Astronomy | Instrumentation | The Sun and the Solar System

CHASING SHADOWS IN THE OUTER SOLAR SYSTEM

Federica Bianco

A DISSERTATION

in

Physics and Astronomy

Presented to the Faculties of the University of Pennsylvania

in Partial Fulfillment of the Requirements for the degree of Doctor of Philosophy

2010

Charles R. Alcock

Supervisor of Dissertation

Ravi Sheth

Graduate Group Chairperson

Acknowledgments

I ain't no physicsist, but i know what matters!

Popeye

The work presented in Chapers 3, 4 & 5 was accomplished with the collaboration of the entire TAOS team: C. Alcock (Harvard-Smithsonian Center for Astrophysics), T. Axelrod (Steward Observatory), Y.-I. Byun (Department of Astronomy, Yonsei University), W. P. Chen (Institute of Astronomy, National Central University, Taiwan), N. K. Coehlo (Department of Statistics, University of California Berkeley), K. H. Cook (Institute for Geophysics and Planetary Physics, Lawrence Livermore National Laboratory), R. Dave (Initiative in Innovative Computing at Harvard), I. de Pater (Department of Astronomy, University of California Berkeley), J. Giammarco (Department of Astronomy and Physics, Eastern University; Department of Physics, Villanova University), D.-W. Kim (Department of Astronomy, Yonsei University), S.-K. King (Institute of Astronomy and Astrophysics, Academia Sinica), T. Lee (Institute of Astronomy and Astrophysics, Academia Sinica), M. J. Lehner (Institute of Astronomy and Astrophysics, Academia Sinica; Department of Physics and Astronomy, University of Pennsylvania; Harvard-Smithsonian Center for Astrophysics), H.-C. Lin (Institute of Astronomy and Astrophysics, Academia Sinica), J. J. Lissauer (Space Science and Astrobiology Division, NASA Ames Research Center), S. L. Marshall (Kavli Institute for

Particle Astrophysics and Cosmology), S. Mondal (Aryabhatta Research Institute of Observational Sciences), P. Protopapas (Initiative in Innovative Computing at Harvard), J. A. Rice (Department of Statistics, University of California Berkeley), M. E. Schwamb (ivision of Geological and Planetary Sciences, California Institute of Technology), J.-H. Wang (Institute of Astronomy and Astrophysics, Academia Sinica; Institute of Astronomy, National Central University, Taiwan), S.-Y. Wang (Institute of Astronomy and Astrophysics, Academia Sinica), C.-Y. Wen(Institute of Astronomy and Astrophysics, Academia Sinica), and Z.-W. Zhang (Institute of Astronomy, National Central University, Taiwan),

This work was supported in part by the NSF under grant AST-0501681 and by NASA under grant NNG04G113G to Harvard University. Observations reported in Chapter 2 were obtained at the MMT Observatory, a joint facility of the Smithsonian Institution and the University of Arizona. Work at National Central University was supported by the grant NSC 96-2112-M-008-024-MY3. Work at Academia Sinica Institute of Astronomy & Astrophysics was supported in part by the thematic research program AS-88-TP-A02. Work at Yonsei University was supported by Korea Astronomy and Space Science Institute. The work of N. Coehlo was supported in part by NSF grant DMS-0636667 to the University of California Berkeley. Work at Lawrence Livermore National Laboratory was performed in part under USDOE Contract W-7405-Eng-48 and Contract DE-AC52-07NA27344. Work at SLAC was performed under USDOE contract DE-AC02-76SF00515. Work at NASA Ames was supported by NASA's Planetary Geology & Geophysics Program. This research has made use of SAOImage DS9, developed by Smithsonian Astrophysical Observatory.

As for the rest:

mamma e papa, la vita mi ha portato lontano, e c'è sempre troppo poco tempo,

molte cose da dire e fare che ci scoraggiamo e non diciamo o facciamo mai. vi voglio bene e mi mancate. e vi sono grata per tutte le opportunità che mi avete dato.

momdadhobogregberngeorge, thanks for being patient.

greg again, for covering up for me, walking the dog for me, making phone calls for me, cleaning up for me, driving around for me... and keeping irony going, most of the times. i could have not done this – or much of anything else really – without you.

Of course Charles, for finding the time, despite the many many more things that should have come ahead of my questions and doubts, family, government, telescope building. I know you lost many hours of sleep. And for the support in times of crisis, of which there were many, such as when almost got deported.

Pavlos, a very tolerant man. special thanks for keeping me calm at times and keeping me creative at others.

Matt, for escorting me in many Taiwan trips, helping me ordering the right liquor in Chinese, facilitating intercultural communication, teaching me that fewer is better, when it comes to lines of code, and wanting to have as little as possible to do with my fits: it worked to control them.

Working on this thesis gave me the great opportunity to travel to Asia many times, and for that I am grateful.

ABSTRACT

CHASING SHADOWS IN THE OUTER SOLAR SYSTEM

Federica Bianco

Charles R. Alcock

The characteristics of the populations of objects that inhabit the outer solar system carry the fingerprint of the processes that governed the formation and evolution of the solar system. Occultation surveys push the limit of observation into the very small and distant outer solar system objects, allowing us to set constraints on the structure of the Kuiper belt, Scattered disk and Sedna populations. I collected, reduced, and analyzed vast datasets looking for occultations of stars by outer solar system objects, both working with the Taiwanese American Occultation Survey (TAOS) collaboration and leading the MMT/Megacam occultation effort. Having found no such events in my data, I was able to place upper limits on the Kuiper belt, scattered disk and Sedna population. These limits and their derivation are described here.

Contents

List of Tables

List of Figures

Chapter 1

Introduction

1.1 Historical note

It could be argued that interest in the solar system initiated scientific thinking. All ancient cultures that left a written or graphical record left some representation of the Sun and the Moon, of the planets and the fixed stars. Dynamical theories of what was then thought of as the entire Universe are among the first records of most cultures. Early Americans, Greeks, Egyptians, Chinese, Babylonians, Indian, Celtic, and Islamic cultures, all generated *cosmological* theories to describe and explain the rising and setting of the sun, the phases of the moon, the motions of the planets across the sky, the immobile stars and the changing of seasons. The motions of solar system objects, which we now call ephemerides, were studied well enough by the ancient Egyptians that they were able to build enormous tomb structures that allow the Sun to shine in precisely once a year and only once a year. Mechanical tools (e.g.: the *Antikythera*) were designed to simplify the calculation of an ephemeris, and are considered today to be precursors to the modern calculators and computers (Write, 2007, and references therein).

Ancient Greek philosophers payed great attention to astronomy, and produced a variety of theories to describe the motion of objects in the sky, including some early heliocentric theories (Aristarchus of Samos, Batten 1981), untill the Aristotelian idea of concentric spheres prevailed and dominated in some form or another, until Copernicus and Galileo[1]. Galileo, Kepler, Newton, and later Kant, started investigating the forces which keep planets moving in their orbits, what holds them up in place and puts them in motion.

Remarkably, after over 2000 years of solar system science, we have probed only as little as 10^{-9} of the space occupied by the solar system: the inner portion, which contains over 99% of its mass. The outskirts of the solar system are however still unexplored. Outside of the orbit of Neptune the solar system is populated by small (thousands of kilometers down to dust grain size) icy bodies, arranged in different structures: the Kuiper belt, the Oort cloud, and the scattered disk. Our direct observational knowledge is limited to relatively large objects populating the Kuiper belt and the scattered disk.

1.2 Formation

In the current solar system formation and evolution scenario planets formed by gravitational instabilities in the protoplanetary nebula: a disk of gas and dust surrounding the Sun.

Throughout the remainder of this section I will refer to the solar system evolution model that came to be known as the *Nice model* (Gomes et al., 2005a; Morbidelli et al., 2005; Tsiganis et al., 2005; Levison et al., 2008, and references therein), one of the most successful scenarios to explain the current configuration of

[1] *Aristotle (Greek philosopher)* - Britannica Online Encyclopedia, Britannica.com. http://www.britannica.com/EBchecked/topic/34560/Aristotle. Retrieved March 2, 2010.

solar system objects. In this model the four giant planets, Jupiter, Saturn, Uranus, and Neptune, originally formed from the circumsolar disk of dust and gas on nearly circular orbits between 5 and 17 AU, a much more compact configuration than that which we see now. Gravitational instabilities in the disk caused accretion processes to form large planets out of the dust and small planetesimals inhabiting the disk. Outside of the planetary orbits there remained a disk of icy planetesimals, extending out to ~ 35 AU.

In the early chaotic solar system the planetesimals which were residing within the planetary orbits suffered occasional gravitational encounters with the outermost giant planets, which changed the planetesimal orbits, initially scattering them inward. In turn, the outermost giant planets began migrating outward to preserve angular momentum. As they were pushed into the inner regions of the solar system, the planetesimals began to interact with Jupiter, which on account of its much larger mass dramatically affected their orbital parameters at each encounter. The icy bodies that encounter Jupiter were sent onto highly elliptical orbits or ejected altogether from the solar system, and to compensate for the loss of angular momentum Jupiter migrated inward.

After several hundred million years Jupiter and Saturn crossed their 1:2 mean motion resonance and that suddenly increased their orbital eccentricities, destabilizing the entire solar system. Uranus's and Neptune's eccentricities were increased as a result of the interaction with Saturn, and as they migrated outward they pushed planetesimals outward as well, wiping the region which they transited clean of icy bodies. Through these interactions, the orbits of Uranus and Neptune were again circularized. Meanwhile the vast majority of planetesimals were shuffled and over 90% of the original planetesimals mass was removed.

Of the planetesimals that have been pushed outward by the migration of

Neptune, a large portion remained in low inclination orbits, and some of them got captured in mean motion resonances with Neptune. These formed the Kuiper belt, first predicted by Kenneth Edgeworth in 1943, and later by Gerard Kuiper in 1951. The Kuiper belt is a flat structure, extending from the orbit of Neptune (~ 30 AU) out to about 50 AU, where observations reveal an outer edge (Jewitt et al., 1998).

A fraction of the Kuiper belt planetesimals were excited, possibly through resonance and weak chaos associated to secular Kozai mechanisms (Volk & Malhotra, 2009), and their inclination distribution increased, forming the scattered disk and extended scattered disk. The scattered disk is a family of TNOs populated by objects with perihelia $q > 30$ AU and with inclinations as high as $i \sim 40°$. The extended scattered disk is a population of object whose perihelia is large enough to be decoupled from Neptune (see Figure 1.1).

Many planetesimals bounced in and out of the inner solar system by repeated encounters with Jupiter. These interactions increased the eccentricities e of their orbits. The planetesimals that were not ejected via this mechanism were hand off out to Neptune. Interactions with Neptune continued increasing the orbital sami-major axis while preserving the perihelion distance of these planetesimals. Once their orbits reached $\sim 3,000$ AU the influence of the mean gravitational field of the Galaxy became important, and their perihelia lifted from the region of influence of Neptune. The inclination distribution of planetesimals in orbit farther than $3,000$ AU increased dramatically: these planetesimals formed the Oort cloud, an isotropic structure of icy bodies which might extend farther out than 10^5 AU (Duncan et al., 1987).

The existence of a cloud of icy bodies in the out skirts of the solar system was originally proposed by J. Oort in 1950 (Oort, 1950), in order to explain the long period the comets we observe. Long period comets are indeed Oort cloud objects at

their perihelion passage and they provide the only observational evidence we have of the Oort cloud.

Figure 1.1 shows a schematic partition of the perihelion and semi-major axis phase space and the TNO families that occupy it. The classical Kuiper belt (KB) lies on the bottom left corner of the plot. An empty square shows the position of the median perihelion and semi-major axis of the classical and resonant KBOs. At $q > 30$ AU and $a > 50$ AU lays the scattered disk (SD). The extended scattered disk comprises objects with perihelia larger than $q \sim 38$ AU, which are decoupled from Neptune. The inner Oort cloud start outward of $a = 3,000$ AU and the outer Oort cloud at $a > 20,000$AU. The reader is cautioned that this schematic separation in $q - a$ space is only for reference. Other families are here ignored, such as the resonant populations, Plutinos, and Centaurs. Furthermore, the TNO taxonomy is *not* unique, and TNO nomenclature is often based on other variable, $q - e$, $q - i$, color, etc. (Barucci et al., 2005; Gladman et al., 2008, and references therein)

The Nice model model is able to explain many features of our solar system: it reproduces the current planetary orbits, the existence of objects in the Kuiper belt and in resonance with Neptune, the asteroid belt, as a relic of the planetary nebula not affected by the migration of Uranus and Neptune. It is however unable to explain the existence of an outer edge in the Kuiper belt, it predicts more mass to be left in the solar system than we know of, and it *cannot explain the the existence of Sedna.*

Sedna was discovered in 2004 (Brown et al., 2004). None of the formation mechanisms in the literature at the time of discovery were able to place orbits in this region of the perihelion and semi-major axis phase space: this region is inaccessible to objects coming from the Kuiper belt as well as for objects being kicked out from

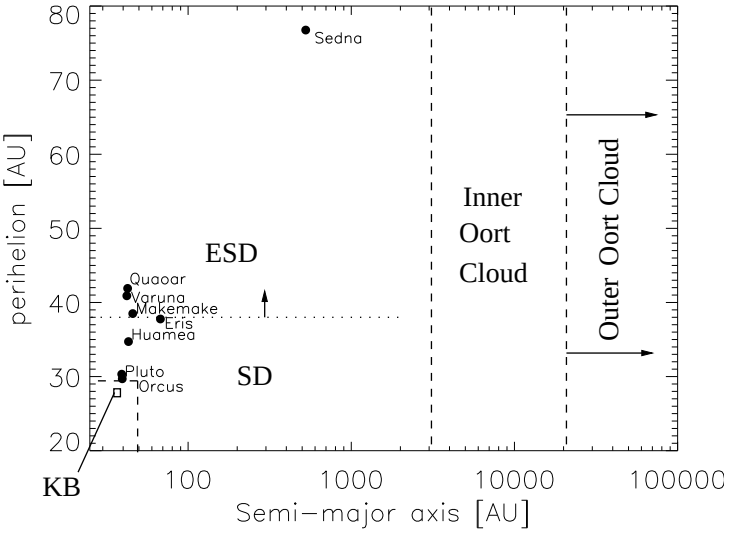

Figure 1.1: Schematic partition of the perihelion and semi-major axis phase space. Five distinct dynamical families are identified: the Kuiper belt (KB) in the bottom left corner, the scattered disk (SD), the extended scattered disk (ESD), the inner and outer Oort cloud. The largest observed TNOs are shown (black circles), as well as the median values of q and a of the Kuiper belt (open square).

the inner solar system. To date no surveys have detected any other object in orbit similar to Sedna, and its existence is still unexplained in the current formation and evolution scenarios without invoking the presence of a perturbation from an external body (see Section 5).

1.3 Observational techniques to explore the outer solar system

Populated by small and cold bodies the outer solar system is among the most challenging observational targets in astrophysics today. Direct detection of Trans Neptunian Objects (TNOs) is a difficult task. These objects typically range from $\sim$ 1000 km in diameter, to sizes as small as dust grains. They do not shine, but

are seen in reflected Sun light, thus getting fainter as $\sim \Delta^4$, where Δ is the distance to the Earth. Furthermore, they move across the sky at a rate of ~ 3 arcsec/hour, making it impossible to increase their detectability just by increasing the integration time, and rendering any technique used to increase the depth of a survey, such as stacking, much harder to perform.

The very first Kuiper belt object to be observed was Pluto (134340 Pluto), discovered in 1930 by Clyde Tombaugh. Pluto has a mean magnitude $R \sim 14$, and a diameter of about 2,390 km. For its size, Pluto is exceptionally bright due to a high albedo of about 50%. Classified as a planet until 2006, Pluto is today the second largest known KBO after Eris (136199 Eris), which has a diameter of about 2,500 km and an apparent magnitude of $R \sim 18.4$. Eris was discovered in 2005 (Brown et al., 2005).

Over 30 years passed between the first detection of Pluto and the discovery of the next KBO. Jewitt and Luu announced the "Discovery of the candidate Kuiper belt object" in a Nature paper on August 30th 1992, the object known as 15760 1992 QB1. Six months later they reported a second object in the Kuiper belt region, 181708 1993 FW. Today (March 2, 2010) 1099 observed TNOs are cataloged by the Minor Planet Center[2], which keeps track of all TNOs and minor planet observations and creates ephemerides to predict their position in time. The rate of TNO discoveries, however, peaked in 2001 and it has been decreasing ever since (see Figure 1.2, left).

To date all observed TNOs are brighter than $R > 30$. Figure 1.2, right, shows the R-magnitude distribution of known KBOs. The majority of the observed objects are in the magnitude range $23 \leq R \leq 26$; the median magnitude of observed TNOs is $\langle R \rangle \sim 23.5$. Figure 1.3, from Fuentes & Holman (2008), shows the

[2] *http://www.cfa.harvard.edu/iau/mpc.html*

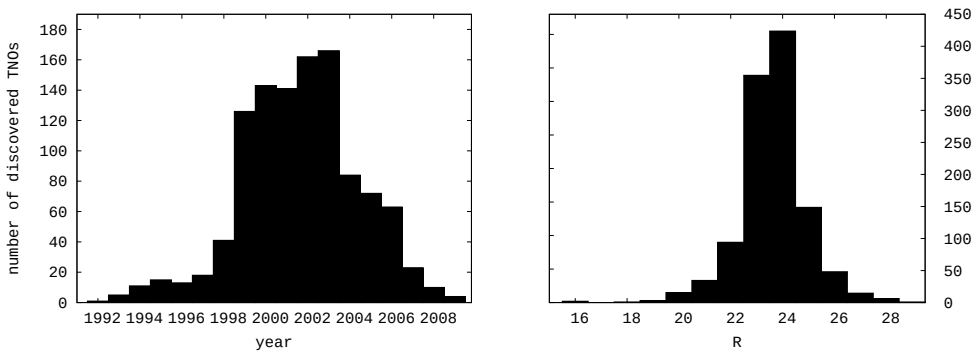

Figure 1.2: Left: number of discovered TNOs per year. Right: number of observed TNOs as a function of R magnitude. The vast majority of observed TNOs have apparent magnitude in the range $22 \leq R \leq 26$. Brighter KBOs are rare and fainter KBOs, although more numerous, are hard to detect

cumulative size distribution of KBOs as a function of R magnitude. Most observed KBO are individually plotted. The density of observed KBOs with $23 \leq R \leq 26$ allows a firm determination of the size distribution in this magnitude range (see Section 1.4). Only three objects have been observed that are fainter than magnitude $R = 26.5$: $R = 26.7,\ 28.0$ and 28.2, corresponding to diameters of respectively 44, 28 and 25 km assuming, as customary, an albedo of 4% (Bernstein et al., 2004).

Future all sky surveys such as Pan–STARRS[3] and LSST[4] will discover many more $R < 26$ objects (Jewitt, 2003), and data mining projects are in progress to detect faint targets in archival HST data (Fuentes et al., 2009a). The observational barrier at $R \sim 30$ is however hard to overcome.

1.3.1 Diffraction dominated occultations of bright stars

Bailey (1976) proposed that small TNOs could be seen indirectly at their passage across the line of sight to a star. This event, today known as an *occultation*, would produce a variation in the flux of the observed star which in principle can

[3] *http://pan-starrs.ifa.hawaii.edu/public/science-goals/solar-system.html*
[4] *http://lsst.org/lsst/science/scientist_outer_solar_system*

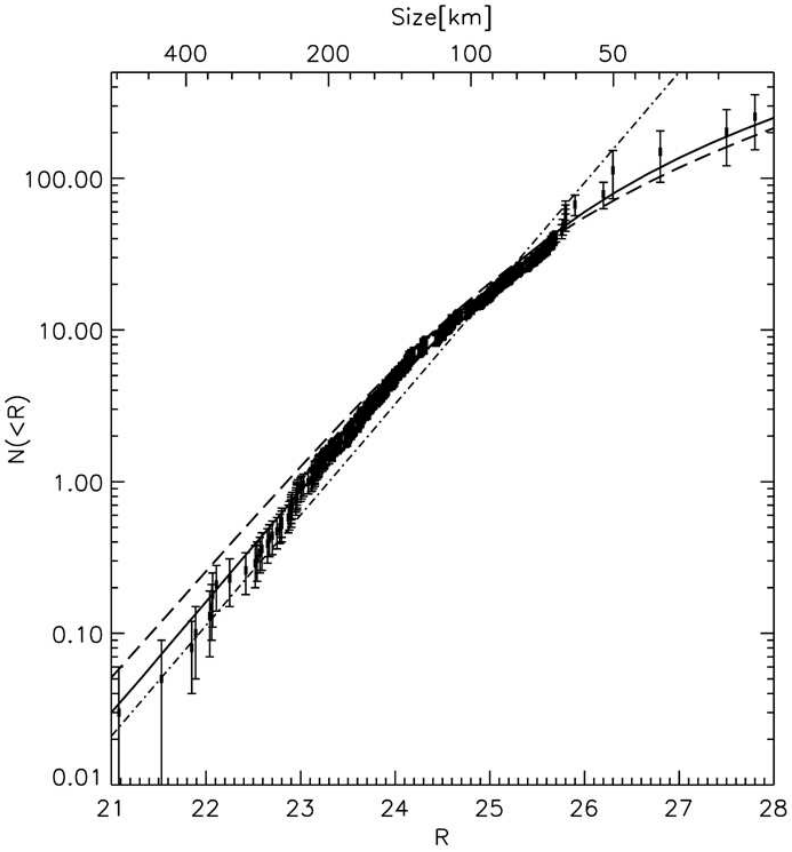

Figure 1.3: From Fuentes & Holman (2008), this plot shows the size distribution of large KBOs as a function of magnitude (converted in diameter on the top axis). The data-points include most KBOs observed directly to date.

be observed, much like in planetary transit surveys. The dramatic difference from planetary transit surveys is however in the geometry of the system: in this technique a distant star, often an unresolved point source, is occulted by a *near-by* object with a finite angular size. Noticeably, for the events of interest, the geometry of the system is such that occultations by outer solar system objects too small to be observed directly are typically diffraction dominated events.

If we consider a roughly kilometer size object in the Kuiper belt (30-50 AU) we have the case of a light wave obstructed by an object at finite distance, where the diffractor size is large compared to the wavelength. In this regime diffraction is properly described in terms of the Huygens–Fresnel principle. The discussion that follows is based on Born & Wolf (1980) and on Roques et al. (1987).

Modeling the occulting object as a flat opaque screen S, and neglecting the scattering of light at the edges of the occulter, the diffraction amplitude a_S of a monochromatic plane wave at wavelength λ can be derived at the observing point 0 by the Fresnel–Kirckoff diffraction formula as follows: assume the occulter S lays on a plane P perpendicular to the line of sight, at a distance D from the observer (and infinitely far from the source of light in the plane wave approximation), then

$$a_S(0) \;=\; N \int\int_{P-S} \frac{e^{\left(\frac{2i\pi}{\lambda}\sqrt{X^2+Y^2+D^2}-D\right)}}{\sqrt{X^2+Y^2+D^2}}\,(1+\cos\theta)\,\mathrm{d}X\mathrm{d}Y, \qquad (1.1)$$

where $P-S$ is the plane of the occulting screen, θ the angular distance from the center of the diffractor, and X and Y the Cartesian distance from the center of the screen S and the point perpendicular to the line of sight on the plane P (see Figure 1.4). This intensity is normalized to $a_S(0) \;=\; 1$ away from the objects by setting $N \;=\; 1/2\lambda i$.

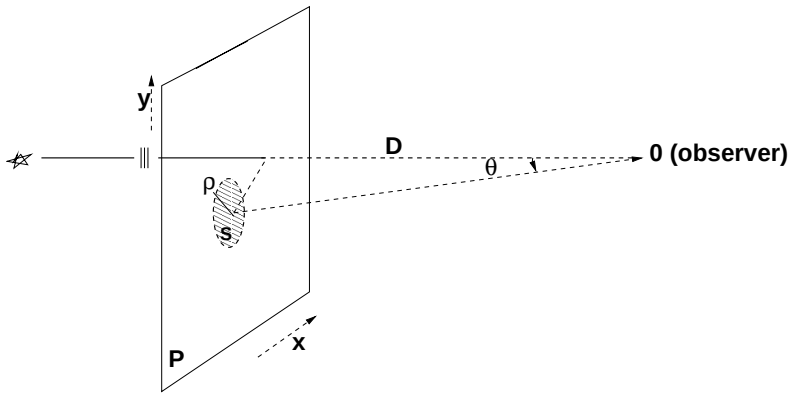

Figure 1.4: Schematic representation of an occultation. The occulter S is modeled as a circular disk laying on the plane P. The occultation is observed by an observer laying at the origin 0.

When the occulter approaches the line of sight, $D \gg \sqrt{X^2 + Y^2}$, then

$$a_S(0) \;=\; 1 - \frac{2N}{D} \int\int_S e^{\left(\frac{i\pi}{\lambda D}(X^2+Y^2)\right)}\; dX\; dY. \tag{1.2}$$

If the occulter is a circular screen with radius ρ we can conveniently move to polar coordinates $(R,\ \phi)$ centered on the center of the occulter, and thus the optical path difference is $X^2 + Y^2 \;=\; R^2 \;+\; r^2 \;-\; 2\; R\; r\; \cos\phi$ and Equation 1.2 can be expressed in terms of Bessel functions as follows:

$$\begin{aligned} a_\rho(0) &= 1 - \frac{2\pi \exp\left(\frac{i\pi r^2}{\lambda D}\right)}{i\lambda D} \int_0^\rho \exp\left(\frac{i\pi}{\lambda D} R^2\right) J_0\left(\frac{2\pi}{\lambda D} r R\right) R\; dR \qquad (1.3) \\ J_0(x) &= \frac{1}{\pi} \int_0^\pi \cos x\;\; \sin t\; dt \end{aligned}$$

where J_0 the Bessel function of order 0.

In units of Fresnel scale, $F = \sqrt{\lambda D/2}$, the integral above can be expressed as:

$$a_\rho(0) \;=\; 1 \;+\; i\pi e^{i\pi r/2} \int_0^\rho e^{i\pi/2R^2} J_0\left(\pi r R\right) R\; dR \tag{1.4}$$

and by $\frac{d}{dx}\left(x^{n+1}J_{n+1}(x)\right) = x^{n+1}J_n(x)$ and the Lommel functions:

$$U_n(\mu,\nu) = \sum_{k=0}^{\infty}(-1)^k\left(\frac{\mu}{\nu}\right)^{n+2k}J_{n+2k}(\pi\mu\nu),$$

we get that outside of the geometrical shadow, or for $r \geq \rho$,

$$a_\rho(0) \;=\; 1 \;+\; i\pi\exp\frac{i\pi(r^2+\rho^2)}{2}\left(U_2(\rho,r)+iU_1(\rho,r)\right), \tag{1.5}$$

while inside the geometrical shadow ($r < \rho$), using $\frac{d}{dx}\frac{J_n(x)}{x^n} = -\frac{J_{n+1}(x)}{x^n}$ we have:

$$a_\rho(0) \;=\; \exp\frac{i\pi(r^2+\rho^2)}{2}\left(U_0(\rho,r)-iU_1(\rho,r)\right). \tag{1.6}$$

Finally it follows that, the measured intensity of a star at wavelength λ is described by:

$$I_\rho(\eta) = \begin{cases} U_0^2(\rho,\eta)+U_1^2(\rho,\eta) & \eta \leq \rho \\ 1+U_1^2(\rho,\eta)+U_2^2(\rho,\eta) & \eta \geq \rho \\ \quad -2U_1(\rho,\eta)\sin\frac{\pi}{2}(\rho^2+\eta^2) & \\ \quad +2U_2(\rho,\eta)\cos\frac{\pi}{2}(\rho^2+\eta^2) & \end{cases}. \tag{1.7}$$

These equations describe a pattern around the center of a point source star, characterized by an alternation of bright and dark fringes centered on the KBO. During the transit of the KBO along the line of sight this translates into a modulated lightcurve (see Figure 1.5). This basic model is further complicated by the finite size of the star, the possibly non-circular shape of the occulter and non-monocromatic observations. Some of these points will be addressed in the following chapters. Note that this description predicts that the flux in the center of the diffraction pattern will be exactly equal to 1 for a circular occulter of size smaller

than the Fresnel scale occulting at $b = 0$ impact parameter. This point in the diffraction pattern is called *Poisson spot* in honor of Poisson, who predicted it [5].

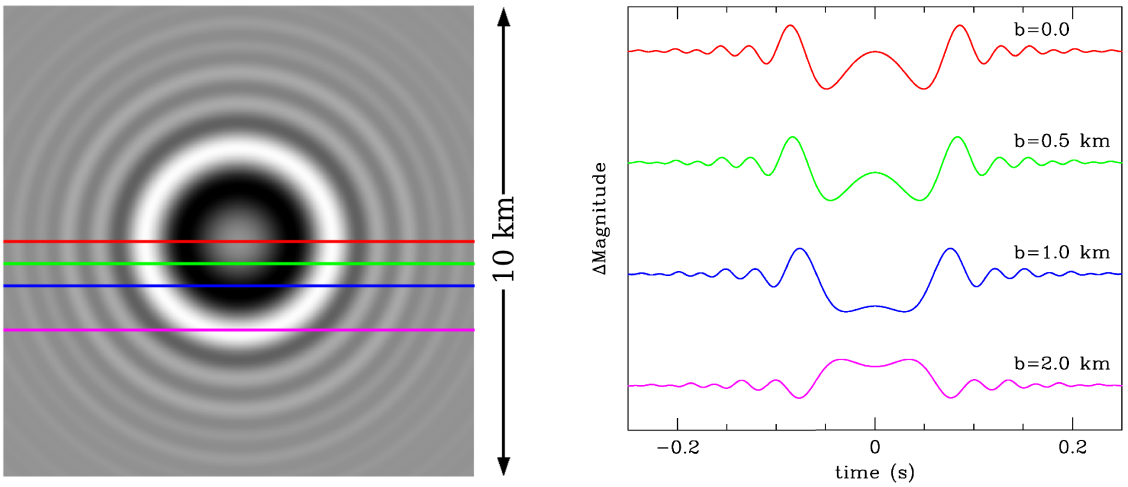

Figure 1.5: Diffraction pattern produced by a $D = 3$ km KBO at 42 AU and theoretical diffraction lightcurves (in magnitude variation) produced by the observation of this occultation at different impact parameters (right). The impact parameters are marked by horizontal lines on the left panel.

The presence of diffraction effects in the event of an occultation is welcome to the observer for two reasons. The transit of an outer solar system object along the line of sight is a very brief event. The relative velocity of the objects is dominated by the velocity at which the earth orbits, $v_{\rm E} \sim 30$ km s^{-1}, and depending upon the observing angle (the *elongation*) TNOs would transit across the line of sight at a speed of a few to ~ 25 km/s. Thus a TNO of diameter $D = 1$ km would transit in front of a background star in 0.04-1 sec. This is a fast rate for precision astrophysical observations, at the limits of feasibility for ground based surveys. Diffraction however assures that the physical size of the event is no smaller than the Fresnel scale, which at the closer end of the Kuiper belt is about 1 km in visible light. In a diffraction dominated occultation, the overall flux reduction is dominated

[5]Ironically the prediction served Poisson, a strong believer in the particle nature of light, to confute Fresnel's theory of light as waves, since at the time the brightening at the center of a shadow had not been observed.

by the size of the KBO, while the duration of the event depends upon the relative velocity $v_{\rm rel}$ and the size of the diffraction pattern H. The relative velocity of KBO can be approximated to:

$$v_{\rm rel} = \left| v_{\rm E} \left(\cos\epsilon - \sqrt{\frac{\Delta_{\rm E}}{\Delta}\left(1 - \left(\frac{\Delta_E}{\Delta}\sin\epsilon\right)^2\right)} \right) \right|, \tag{1.8}$$

where $\Delta_{\rm E}$ the distance of the Earth from the Sun, and ϵ the angle from opposition (Liang et al., 2004; Nihei et al., 2007). We define the cross section of the event H as the diameter of the first Airy ring: the first (and brightest) bright fringe in the occultation pattern (Born & Wolf, 1980). H it is limited by the Fresnel scale for sub-kilometer KBOs and by the size of the object for large KBOs as follows (Nihei et al., 2007):

$$H = \left[\left(2\sqrt{3}F \right)^{\frac{3}{2}} + D^{\frac{3}{2}} \right]^{\frac{2}{3}} + \Delta\theta, \tag{1.9}$$

where the additive term $\Delta\theta$ accounts for the finite angular size of the star. When observing at opposition, the relative velocity $v_{\rm rel}$ of an object orbiting the Sun at 40 AU is about 25 km and the typical duration of an occultation by sub-kilometer KBOs is ~ 0.2 s.

Furthermore the occultation features contain information about the system that generated the event, with potential for disentangling the size, the distance and shape of the occulter (although much of this information is not yet accessible in present occultation surveys). Figure 1.6 shows the region of diameter and semi-major axis space where most TNOs reside. The current limit of direct observations is shown at $R = 30$. The Fresnel scale is also shown: all objects that lay below the dashed line would generate diffraction phenomena during an occultation. The angular size for a magnitude $V = 13$ G0V star is shown: as the angular size of the

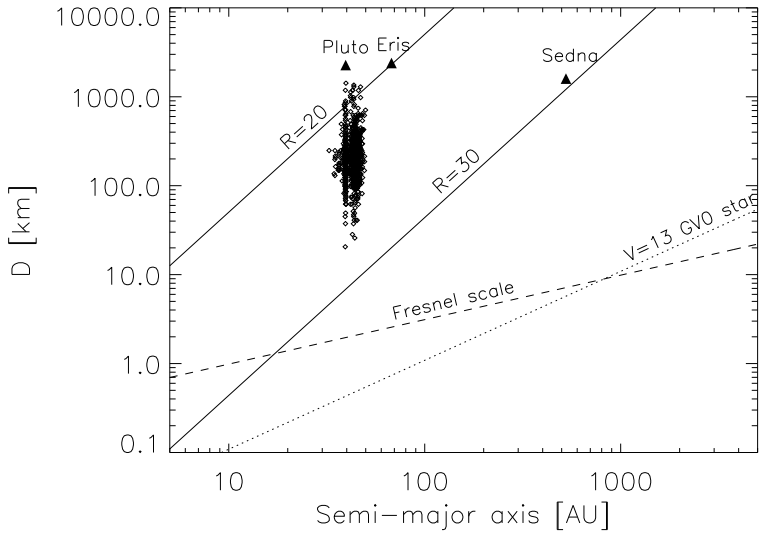

Figure 1.6: Diameter versus semi-major axis. The black diamonds show the known KBOs. The triangles indicate several of the larger, well-known outer Solar System objects at their semi-major axes. The solid lines indicate contours of constant brightness in reflected sunlight, assuming an albedo value of 0.04. The long dashed line shows the Fresnel scale as a function of distance assuming $\lambda = 650$ nm. Occultations by objects below this line are diffraction dominated. The dotted line is the angular size of a V=13 G0V star as a function of distance. The limit of direct observations is shown at $R = 30$.

star becomes comparable to the Fresnel scale the diffraction features are smoothed out (see Chapter 3 and Nihei et al. 2007).

1.4 The story told by the small KBOs

Probing the very small ($D \leq 10$ km) region of the KBO size spectrum and the regions of the solar system outside of the Kuiper belt could have profound consequences on our understanding of the formation and on the evolution of the solar system.

The Kuiper belt has been shaped by accretion and disruption processes throughout the history or the solar system. With small orbital eccentricities the

relative velocities of the objects in the early Kuiper belt were sufficiently low to allow accretion processes to form kilometer and much larger objects. Later, when the velocity dispersion increased as the KBO population was stirred up by the gravitational effects of the larger planets and planetoids, only large objects were able to continue growing through impacts, whereas collisions among smaller bodies resulted in disruption. The details of these processes depend on the internal strength of the KBOs and on the orbital and dynamical evolution of the gas giant planets. The size distribution of KBOs, therefore, contains information on the internal structure and composition of the KBOs – and hence information on the location and epoch in which they formed – and about planetary migration (Pan & Sari, 2005; Kenyon & Bromley, 2004; Kenyon et al., 2008, and references therein).

Direct observations have detected KBOs as faint as magnitude $R \sim 28.2$ (Bernstein et al., 2004), which corresponds to about 24 km in diameter assuming a 4% albedo. The KBO size distribution can be characterized using its brightness distribution. The latter is well described by a power law $\Sigma(< R) = 10^{\alpha(R-R_0)}$ deg^{-2}, with an index $\alpha = 0.6$ and $R_0 = 23$ (Fraser & Kavelaars 2008, Fuentes & Holman 2008) for objects brighter than about $R = 25$, or $D \sim 100$ km. This is the region of the size spectrum which reflects the early history of agglomeration. Kenyon & Windhorst (2001) pointed out that the intensity of the infrared Zodiacal background sets limits on the extrapolation of a straight power law to smaller sizes. The relatively shallow size distribution of Jupiter Family Comets (JFCs, Tancredi et al. 2006), which are believed to originate in the Kuiper belt, and the cratering of Triton observed by *Voyager 2* (Stern, 1996), all point to a flatter distribution for small KBOs[6]. In 2004 evidence surfaced that a break in the power law occurs

[6]The relationship between the cratering of Triton and the Kuiper belt size distribution is questioned in Schenk & Zahnle (2007).

at a diameter larger than 10 km: Bernstein et al. (2004) conducted deep Hubble Space Telescope observations with the Advanced Camera for Surveys which led to the discovery of only 3 new objects fainter than R = 26, about 4% of the number expected from a single power law distribution extrapolated to $R = 29$. While this work remains the state of the art for deep direct surveys of the outer solar system, recent campaigns have observed many more faint objects down to magnitude $R = 27$, which with the assumption of a 4% albedo corresponds to about 40 km in diameter[7] (Fraser & Kavelaars 2008, Fuentes & Holman 2008, Fuentes et al. 2009b, and Fraser & Kavelaars 2009). These recent data allowed them to locate a break in the power law size distribution in the diameter range $D = 30 - 120$ km.

The range of the size spectrum of Kuiper belt objects (KBOs) between tens of kilometers and meters in diameter is particularly interesting as models predict here the occurrence of transitions between different strength and gravitation regimes that would leave a signature in the size distribution (Pan & Sari 2005, Kenyon & Bromley 2004, Benavidez & Campo Bagatin 2009, and references therein). Occultation surveys allow us to reach farther then the current limits of direct observations, and into this very region of interest, and they are the only observational method presently expected to be able to detect such small objects in the outer solar system.

While occultation surveys were first proposed in 1976, only recently have results been reported. This observational technique requires sub-second photometric measurements which have only recently become possible. Chang et al. (2006) conducted a search for KBO occultations in the archival Rossi X-ray Timing Explorer (RXTE) observations of Scorpius-X1, the brightest X-ray source in the sky. RXTE is a satellite dedicated to the observation of X-ray astronomical sources, able

[7]The magnitude of KBOs is converted into diameter by assuming a nominal 4% albedo throughout this work, except for the Fraser & Kavelaars 2008 result where the authors assumed an albedo of 6%.

to provides high cadence ($\geq$ μsec) time series of X-ray sources. Chang et al. (2006) explored nearly 90 hours of Sco-X1 data collected between 1996 to 2002 by RXTE, and reported a surprisingly high rate of occultation–like phenomena: dips in the lightcurves compatible with occultations by objects between 10 and 200 m in diameter. Jones et al. (2008) showed that most of the dips in the Sco-X1 lightcurves may be attributed to artificial effects of the response of the RXTE photo-multiplier after high energy events, such as strong cosmic ray showers. Only 12 of the original 58 candidates cannot be ruled out as artifacts, but are hard to confirm as events (Jones et al., 2008; Chang et al., 2007; Liu et al., 2008). New RXTE/PCA data of Sco X-1 provided a less constraining upper limit to the size distribution of KBOs (Liu et al., 2008).

Several groups have conducted occultation surveys in the optical regime. Roques et al. (2006) and Bickerton et al. (2008) independently observed narrow fields at 45 Hz and 40 Hz, respectively, with frame transfer cameras. Such cameras allowed them to obtain high signal-to-noise ratio (SNR) fast photometry on two stars simultaneously. Both surveys expect a very low event rate due to the limited number of stars and the limited exposure, and neither survey has claimed any detection of objects in the Kuiper belt at this time[8]. An upper limit for KBOs with $D \geq 1$ km was derived by Bickerton et al. (2008) by combining the non-detection result of the surveys of Chang et al. (2007), Roques et al. (2006), and Bickerton et al. (2008).

In my graduate studies I participated in two campaigns to detect occultation events in star time–series. This effort is described in the following chapters. Chapters 2-4 describe the effort on the determination of the size distribution of KBOs. The survey I conducted at the MMT with the Megacam imager is described in Chapter 2. TAOS (Taiwanese American Occultation Survey) is a dedicated auto-

[8]Roques et al. report 3 possible occultations from objects outside of the Kuiper belt.

mated multi-telescope survey (Lehner et al., 2009b). TAOS reported no detections but placed the strongest upper limit to date to the surface density of small KBOs, which is reported in Zhang et al. (2008). My work on the first 3.75 years of TAOS data, a substantially larger dataset than the one used in Zhang et al. (2008), is described in Chapters 3 and 4. Chapter 5 describes a search in progress for Sedna-like and scattered disk objects in the TAOS data. Finally I summarize the conclusions and discuss perspectives for the future of this work.

Chapter 2

The sub-km end of the Kuiper Belt size distribution

We conducted a search for occultations of bright stars by Kuiper belt Objects (KBOs) to estimate the density of sub-km KBOs in the sky. We report here the first results of this occultation survey of the outer solar system conducted in June 2007 and June/July 2008 at the MMT Observatory using Megacam, the large MMT optical imager. We used Megacam in a novel shutterless *continuous–readout* mode to achieve high precision photometry at 200 Hz, which with point-spread function convolution results in an effective sampling of ∼30 Hz. We present an analysis of 220 star hours at signal-to-noise ratio of 25 or greater. The survey efficiency is greater than 10% for occultations by KBOs of diameter $D \geq 0.7$ km, and we report no detections in our dataset. We set a new 95% confidence level upper limit for the surface density $\Sigma_N(D)$ of KBOs larger than 1 km: $\Sigma_N(D \geq 1 \text{ km}) \leq 2.0 \times 10^8 \text{ deg}^{-2}$, and for KBOs larger than 0.7 km $\Sigma_N(D \geq 0.7 \text{ km}) \leq 4.8 \times 10^8 \text{ deg}^{-2}$.[1]

[1]This work appeared in The Astronomical Journal, Volume 138, Issue 2, pp. 568-578 (2009), with title *A Search for Occultations of Bright Stars by Small Kuiper Belt Objects Using Megacam on the MMT* and it was co-authored by P. Protopapas (Harvard-Smithsonian Center for Astrophysics, Initiative in Innovative Computing at Harvard), B. A. McLeod (Harvard-Smithsonian

2.1 Introduction

The survey I report here was conducted using Megacam (McLeod et al., 2006, Figure 2.2) at the 6.5 m MMT Observatory at Mount Hopkins, Arizona. The use of Megacam in *continuous–readout* mode (see Section 2.2) on a field of view of $24' \times 24'$ allowed us to monitor over $\sim$ 100 stars at 200 Hz over the course of two observational campaigns conducted in June 2007 and June-July 2008. This peculiar use of a conventional CCD camera allowed us to reach the high speed photometric sampling necessary to detect occultations by small outer solar system objects without compromising the number of star targets monitored. Our survey is

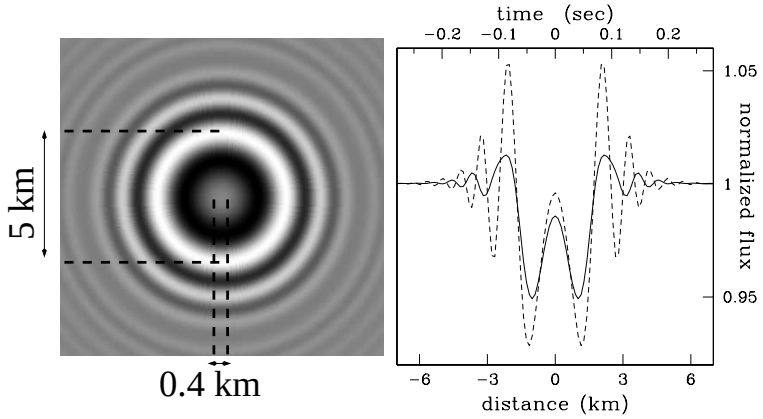

Figure 2.1: A simulated diffraction pattern (left panel) generated by a spherical $D = 1$ km KBO occulting a magnitude 12 F0V star. The MMT/Megacam system bandpass (Sloan r' filter and camera quantum efficiency) is assumed. The size of the KBO and the size of the Airy ring – a measure of the cross section of the event – are shown for comparison. The right panel shows the diffraction signature of the event (assuming central crossing: impact parameter b = 0) as a function of the distance to the point of closest approach (bottom scale). The top scale shows the time-line of the event assuming an observation conducted at opposition (relative velocity $v_{\rm rel} = 25$ km s^{-1}). The occultation is sampled at 200 Hz (dashed line), and at 30 Hz, the effective sampling rate after taking PSF effects into account (solid line, see Section 2.3).

Center for Astrophysics), C. R. Alcock (Harvard-Smithsonian Center for Astrophysics), M. J. Holman (Harvard-Smithsonian Center for Astrophysics), M. J. Lehner (Institute of Astronomy and Astrophysics - Academia Sinica, University of Pennsylvania, Harvard-Smithsonian Center for Astrophysics)

sensitive to occultations by outer solar system objects of diameter $D \sim 700$ m or larger.

In our survey, the bandpass of the observation is centered near $\lambda = 500$ nm and, at distance $\Delta \sim 40$ AU, the Fresnel scale F is $F \sim 1.2$ km. Any occultation caused by objects in the Kuiper belt of a few kilometers in diameter or smaller will exhibit prominent diffraction effects. Figure 2.1 shows a diffraction pattern generated by a $D = 1$ km KBO (left) and the diffraction feature that would be imprinted in a star lightcurve observed by our system (right).

We report no detections in 220 star hours. Our MMT survey is designed

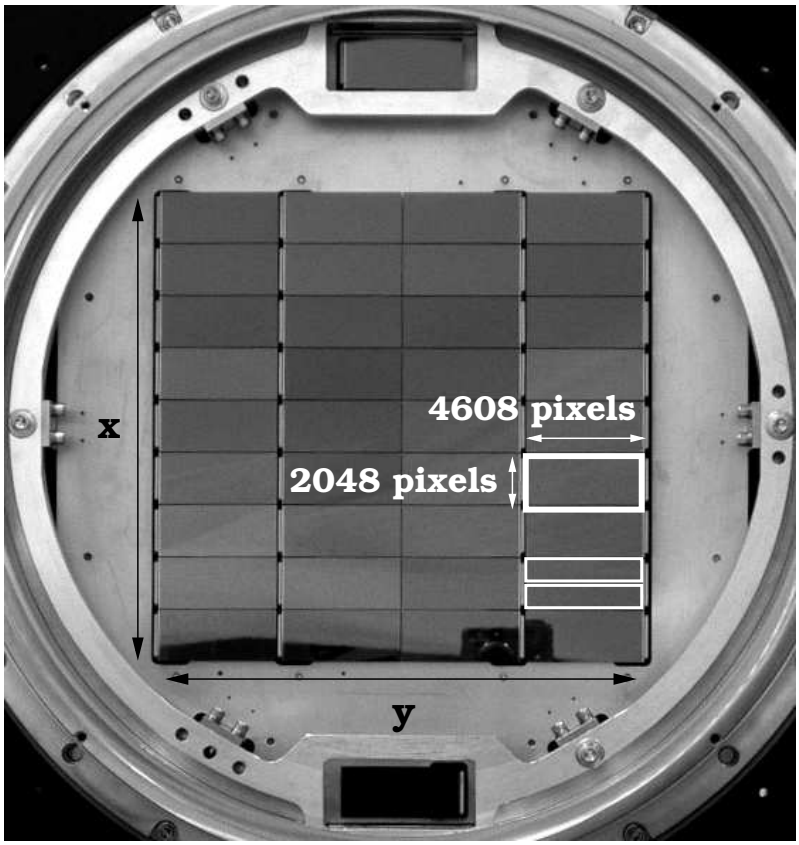

Figure 2.2: Megacam focal plane (McLeod et al., 2006). A thick rectangle outlines a single CCD in the 9x4 CCDs mosaic. Two halves of each CCD (thin rectangles) are read into two separate amplifiers; each amplifier generates a separate output image in our observational mode. The x and y axis, as they would appear in a resulting image, are also shown.

to be complementary to TAOS and to reach smaller size limits, and unlike TAOS it would allow us to estimate the size of a detected occulting KBO. We expect further work on adaptive photometry and de-trending to significantly improve our sensitivity, perhaps allowing us to detect KBOs as small as $D \geq 300$ m. I discuss the improvements we are developing on this analysis in Section 6.1. The preliminary analysis we present here allows us to derive upper limits for objects $D \geq 700$ m.

In the next section I describe the novel observational mode adopted for this survey. In Section 2.3 I describe the data acquired and analyzed for this paper. Details of the data extraction and reduction, which required custom packages, are addressed in the same section. Section 2.4 describes the characteristics of the noise of our current datasets, and our noise mitigation approach. Section 2.5 describes the detection algorithm. In Section 2.6 I derive our upper limit to the density of KBOs. I also compare in detail the achievements of our survey to those of previous surveys.

2.2 Fast Photometry with a Large telescope: The Continuous – Readout Mode

Achieving sub-second photometric sampling is a challenge in optical astronomy. CCD cameras can perform fast photometric observations by reading out small sub-images, limiting the observations to very small portions of the sky (e.g., Marsh & Dhillon 2006, Bickerton et al. 2008). This is the approach adopted by Roques et al. (2006), and Bickerton et al. (2008), who observed two stars at one time. Due to the rarity of occultation events, however, one would want to maximize the number of targets and the total exposure to increase the number of detections. TAOS achieves sub-second photometric observation on up to 500 targets with the

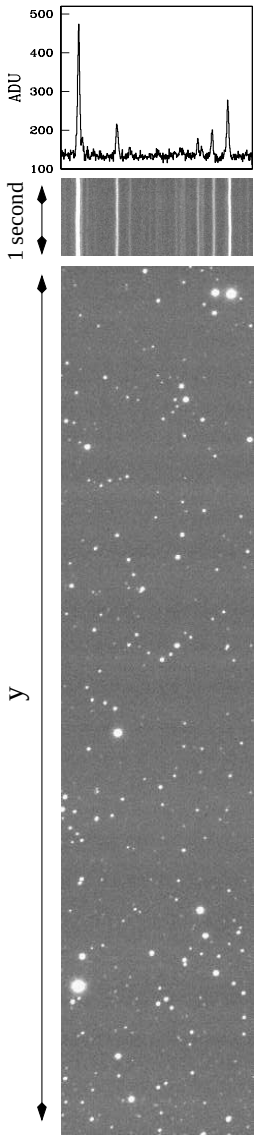

Figure 2.3: Conventional stare mode image (one half of a CCD) of one of our fields (bottom panel). A series of rows from continuous–readout mode (center panel) from the same CCD and field, where the rows are stacked together in a single image. The flux profile of the central row of this segment of continuous–readout data is plotted in the top panel.

zipper mode readout technique (Lehner et al., 2009b), but they sample at $\leq$ 5 Hz rate. Our continuous–readout technique allows us to observe the entire field of view of the camera at 200 Hz.

Megacam, the MMT optical imager, is a mosaic camera comprising thirty-

six CCDs – each with an array of 2048×4608 pixels – with a $24' \times 24'$ field of view (Figure 2.2). The standard readout speed of each CCD is 0.005 sec/row with 2×2 binning. For this survey, we operated the camera in shutterless continuous–readout mode; that is, we kept the shutter open while scrolling and reading the charges at the standard readout speed, tracking the sky at the sidereal rate. Each star is represented in each row that is read out of the camera, and the flux from a star in a row represents a photometric measurement of that star sampled at 200 Hz. Stacking each read row into a single image each star time–series forms a streak along the readout axis ($y-$axis). A small portion of our data is shown in Figure 2.3.

In this observational mode the flux from the sky background is added continuously as the charge is transferred from one end of the CCD to the other, so the sky is exposed $2304 \times 0.005 \ = \ 11.52$ sec for every 0.005 sec integration on each star image (where 2304 is the effective number of rows in each 2×2 binned CCD). In this mode the photon limited SNR is typically ~ 180 for an r' magnitude 10 star.

When observing multiple targets simultaneously one can notice that the lightcurves are affected by common fluctuations, or *trends*, due for example to weather patterns (Kim et al., 2008, and references therein). In our observational mode, however, additional flux variations are caused by wind-induced resonant oscillations of the telescope. While the image motion along the x axis of the focal plane (transverse to the readout direction) can be resolved (see Section 2.3.1), the image motion parallel to the direction of the CCD readout induces an effective variation in the exposure time of a star for a given row. These fluctuations are common to all stars in the field (with possible position dependencies) and therefore, in principle, they are completely removable. We discuss the de-trending of our data in Section 2.3.1. Other sources of noise that affect continuous-readout mode data are discussed in Section 2.4. The typical duration of a set of contiguous data was 10–15

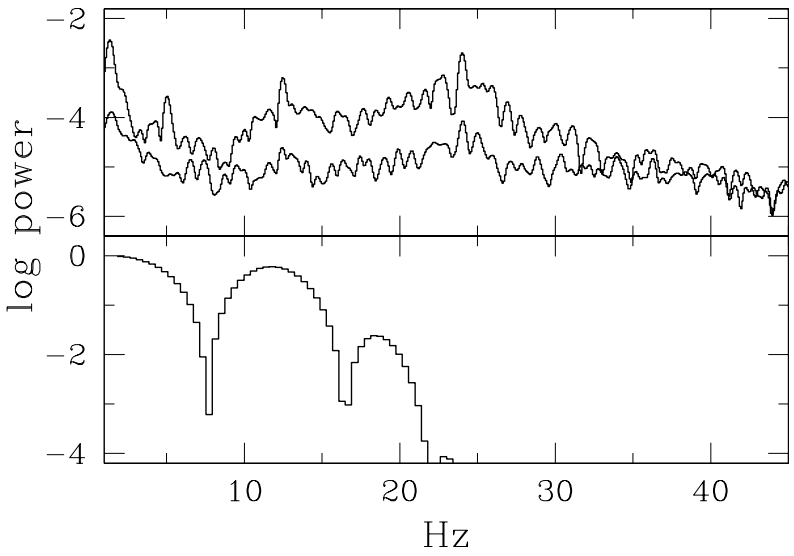

Figure 2.4: Top: power spectrum of one of our lightcurves before and after de-trending the lightcurve to remove noise (see Section 2.3.1). Bottom: power spectrum of the occultation time–series for a 1 km KBO at 40 AU occulting a F0V $V = 12$ star.

minutes (after which the data load on the buffer would become prohibitive). For each amplifier, a single FITS[2] file is created wherein all of the rows read out during a data run are stored as a single image. For a typical run each FITS output image contains 100K to 130K rows, corresponding to about 150–200 Mb of data.

2.3 Data

We selected observing fields within 2.8° of the ecliptic plane, where the concentration of KBOs is highest (Brown, 2001). In order to maximize the number of targets we selected our fields at the intersection of the ecliptic and galactic planes (RA $\sim 19^{\rm h}0000^{\rm s}$, Dec $\sim -21^o00'00''$). We conducted our observations in June-July, when our fields were near opposition (elongation angle $\varepsilon = 180°$) and the relative velocity of the KBOs is highest (Roques et al., 1987; Nihei et al., 2007; Bickerton

[2]Flexible Image Transport System, *http://fits.gsfc.nasa.gov/*.

Table 2.1. MMT/Megacam survey observed fields

RA	Dec	λ[a] (deg)	ε range[b] (deg)
17^h0000^s	$-21°15'00''$	1.5	174–160
17^h1500^s	$-20°15'00''$	2.8	176–163
18^h0000^s	$-21°15'00''$	2.2	171–173
18^h0000^s	$-21°30'00''$	1.9	171–173
18^h0000^s	$-21°45'00''$	1.7	172–173
19^h0000^s	$-22°00'00''$	0.7	158–172

[a]ecliptic longitude

[b]range of elongation angles

et al., 2009), thus maximizing the event rate per target star. Pointing information for our fields is summarized in Table 2.1. The RA and Dec of each observed field are listed together with the ecliptic latitude (λ) and a maximum range of elongation angles at which the filed might have been observed.

We also observed control fields. These were chosen on the galactic plane at a high ecliptic latitude; we expect a negligible rate of occultations by KBOs in these fields. These data allow us to assess our false positive rate. Since we report no detections the analysis of these fields is not discussed further in this paper. All of our observations were conducted in Sloan r' filter (Smith et al., 2002). A set of about 7 hours on target fields was collected in 5 half nights in June 2007 and a similar number of hours was collected on control fields. A set of about 7 hours on target fields and about 6 hours on control fields was collected in 7 half nights in June-July 2008. Out of the 2007 dataset 100.61 star hours at SNR $\geq$ 25 are considered in this paper. From the 2008 dataset we use here 118.93 star hours. Information on our dataset is summarized in Table 2.2. The minimum signal-to-noise ratio of 25, is

Table 2.2. MMT/Megacam survey data set parameters.

Start Date	2007 June 6
End Date	2007 June 10
Exposure at SN$\geq$ 25	100.61 star-hours
Number of lightcurves with SN$\geq$ 25	990
Number of Photometric Measurements	7.2×10^7
Start Date	2008 June 27
End Date	2008 July 1
Exposure at SNR$\geq$ 25	118.93 star-hours
Number of lightcurves with SNR$\geq$ 25	527
Number of Photometric Measurements	8.5×10^7

chosen arbitrarily: 25 is the minimum SNR of the surveys of Roques et al. (2006) and Bickerton et al. (2008).[3] A SNR 25 limits our sensitivity to fluctuations greater than 4%. An occultation of a magnitude 12 F0V star by a KBO of $D = 400$ m diameter would produce a 4% effect. Our efficiency tests, however, revealed our sensitivity rapidly drops below 10% for objects smaller than $D = 700$ m, due to residual non-Gaussianity in our time–series photometric data. We discuss this in Section 2.4.

2.3.1 Data extraction and reduction

Extraction

Custom algorithms have been developed for the data extraction and reduction. For each field a preliminary *stare mode* (conventional) image is collected before each series of high-speed runs. At the beginning of our analysis the stare

[3]Note however that this SNR level is obtained here for 200 Hz, whereas Roques et al. (2006) and Bickerton et al. (2008) observed at 45 Hz and 40 Hz.

mode image is analyzed using SExtractor (Bertin & Arnouts, 1996) to generate a catalog of bright sources. This catalog is used to identify the initial position and brightness of each star in the focal pane. In order to analyze the continuous readout data, we first determine the sky background for each CCD and each row. To do so we calculate the mean of the flux counts in each row after removing the measurements that are three σ's or more above the mean (3σ-clipping) iteratively until the mean converges. This removes most of the pixels in the row containing flux from resolved stars. Next, a subset of stars that are bright and isolated is selected from the stare–mode catalog and used to determine the x-displacement of the focal plane. The focal plane is split into two halves, 9×2 chips each, that are analyzed separately. We select eight stars, two near each of the four corners of each half-focal plane. This allows us to characterize the global motion of the targets even in the presence of small rotational modes or spatial dependency (see Section 2.4). For each star ($\star$), and at each time–stamp (t), we calculate $\mu_\star(t)$ and $\sigma_\star(t)$, respectively the centroid offset from the original position and the standard deviation of the star image, assuming a Gaussian profile. Note that, for a given time-stamp, flux from different stars will appear on different rows due to the y-positions of the stars on the focal plane. A 1-D Gaussian

$$F_\star \;=\; I_\star \;\exp\left(-\frac{(x-\mu_\star(t))^2}{2\sigma_\star^2(t)}\right) \;+\; I_{bg} \tag{2.1}$$

(where $F_\star$ is the total star flux, $I_\star$ the flux at the peak and $I_{\rm bg}$ the sky) is fit for each of the eight stars to each row of the star–streak. Thus the x-displacement $\bar{\mu}(t)$ for all the stars in the field at time–stamp t is estimated to be the weighted average

of the star displacements:

$$\bar{\mu}(t) = \frac{\sum_{\star=1}^{8} \omega_\star(\mu_\star(t) - \mu_\star(t_0))}{\sum_{\star=1}^{8} \omega_\star}, \tag{2.2}$$

where $\mu_\star(t_0)$ is the star initial x-position and $\omega_\star$ is the weight used for that star.

In order to weight our average we use the correlation of the entire x–displacement time–series $\mu_\star$ with respect to the rest of the star set:

$$\omega(i,j) = \frac{1}{T}\sum_{t=0}^{T} \frac{(\mu_i(t) - \langle\mu_i\rangle)(\mu_j(t) - \langle\mu_j\rangle)}{s_i^2(t)\ s_j^2(t)}, \tag{2.3}$$

$$\omega_\star = \frac{1}{7}\sum_{j\neq\star} \omega(\star, j); \tag{2.4}$$

where s^2 is the variance of the displacement throughout the duration T of the time–series. The weight $\omega_\star$ is the square of the Pearson's correlation coefficient (Rice, 2006, pag. 406), a measure of the correlation of the displacement time–series for one star with the other seven. All star lightcurves in the field are then extracted by aperture photometry adjusting time–stamp by time–stamp the center of the aperture according to the x-motion derived in this stage, and with a fixed aperture size which is proportional to the average FWHM in the run.[4]

De-trending

The lightcurves thus extracted show evident semi–periodic and quasi– sinusoidal flux variations that can be associated with oscillatory modes of the telescope

[4]We attempted to extract the lightcurves with both fixed aperture size and variable aperture size, using the FWHM calculated by Gaussian fitting as a point by point estimator of the aperture size. The fixed aperture extraction proved to be more reliable than the variable aperture extraction, which induced further noise in our lightcurves.

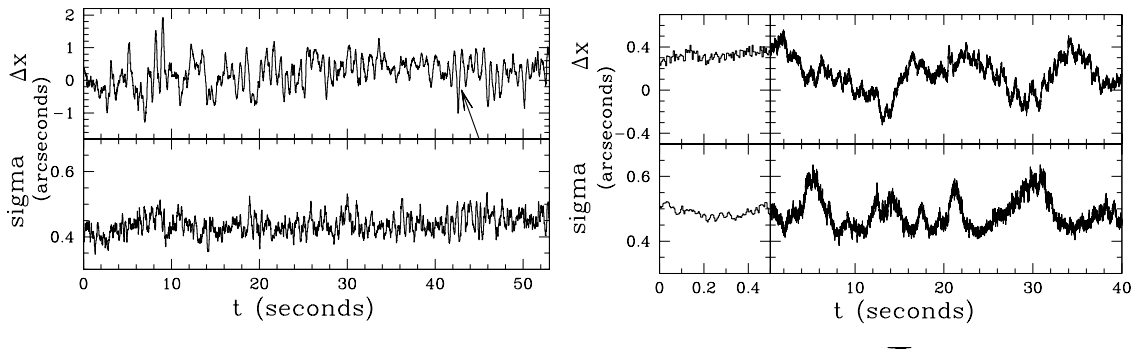

Figure 2.5: Image motion and PSF over time: mean of the x displacements for eight bright isolated stars, at the four corners of the half-focal plane for two data runs (top left and right panels). PSF width from the Gaussian fit averaged over the same set of stars (bottom left and right). On the left we used the same run used to generate Figure 2.8. The arrow points to the displacement feature marked in Figure 2.8. On the right the x-displacement and the PSF width for another run, with the first 0.5 seconds shown on the left at higher time resolution. Note how in the second run the x-displacements are less prominent (note the different y scale) but the amplitude of the variability of the PSF is larger.

in the y direction. In particular, a Fourier analysis generally reveals two strong modes, roughly consistent among runs, one with period near 0.04 seconds and the other near 0.5 seconds. Fourier spectra for one of our lightcurves, before and after processing it, are shown in Figure 2.4 (top). Because these fluctuations affect the whole CCD plane, they are common to all stars and can be removed to achieve greater photometric precision. We now want to identify and remove these trends from our lightcurves, a process that we call *de-trending*.

The general algorithm we used for de-trending is described in Kim et al. (2008). The method takes advantage of the correlation among lightcurves to extract and remove common features. Since we can identify distinct semi–periodic modes we de-trend high and low frequencies separately (typically $\nu > 10$Hz and $\nu < 10$Hz).

We first smooth the lightcurves, to remove all but the frequencies that we want to de-trend, by applying a low–pass or high–pass filter. We then select a subset of N_τ *template* lightcurves (f_τ) that show the highest correlation in the lightcurve

features. N_τ is typically about 15. A master trend lightcurve τ is generated as the weighted average of the normalized template lightcurves:

$$\tau(t) = \frac{1}{N_\tau} \frac{\sum_{j=1}^{N_\tau} \sigma^2(f_{\tau,j})\ f_{\tau,j}(t)/\langle f_{\tau,j}\rangle}{\sum_{j=1}^{N_\tau} \sigma^2(f_{\tau,j})} \tag{2.5}$$

where the notation $\langle f_{\tau,j}\rangle$ denotes the mean flux of $f_{\tau,j}(t)$ over the duration T of the lightcurve, and the weight $\sigma^2(f_{\tau,j})$ is the variance of the lightcurve in time; $\tau(t)$ has mean value of unity and it represents the correlated fluctuations in all lightcurves.

The main trend is physically associated with an over-under exposure phenomenon due to global image motion along the y axis, which causes the effective exposure time to vary (see Section 2.2), therefore scaling the flux. In order to remove these common trends we divide point by point the flux of each original lightcurve f by the trend master lightcurve. To improve the de-trending effectiveness we allow a free multiplicative factor A_f (a scaling factor) for each lightcurve as follows:

$$f_{\mathrm{d},A_f}(t) \ = \ f(t) \left[\left(\frac{1}{\tau(t)} - 1 \right) A_f \ + \ 1 \right]; \tag{2.6}$$

f_{d,A_f} is the de-trended lightcurve.

We optimize our de-trending by selecting A_f to minimize the variance of the de-trended lightcurve f_d with respect to $f_\mathrm{c} \ = \ f - f_\mathrm{s} + \langle f_s \rangle$, which is the original lightcurve cleaned of the frequency to be de-trended. We apply a high–pass (low–pass) filter to f to obtain f_s if we want to de-trend the low (high) frequencies. A_f is then optimized by setting:

$$\frac{\partial}{\partial A_f} \sum_{t=1}^{T} \left(f_{\mathrm{d},A_f}(t) \ - \ \langle f_\mathrm{c} \rangle \right)^2 = 0, \tag{2.7}$$

which minimizes the second moment of the de-trended lightcurve with respect to f_c. The optimal value of A_f can be calculated analytically.

We set no constraints on A_f, and for all of our runs the optimal values of A_f proved to be close to 1 (which is what we expect in the presence of global trends) except for pathological cases where the flux of the star was buried in noise and the raw and de-trended SNR were extremely low. These lightcurves would not pass SNR cuts and were never considered in any of our analysis.

Examples of the results obtained by our de-trending algorithm are displayed in Figures 2.6 and 2.7. In Figure 2.6 the top two panels show lightcurves for two independent sources in our field, and the bottom two panels show the same lightcurves after de-trending. Note that the top star is ~ 2.5 magnitudes brighter than the other and this is reflected in the lower SNR of the fainter source (bottom panel). Figure 2.7 shows one of our lightcurve before (top) and after de-trending (bottom). The raw lightcurve is implanted with an occultation by a $D = 1$ km KBO occulting a $V = 9$ F0V star. The diffraction feature is completely lost in the trends and becomes evident only after de-trending. In the bottom panel we show the lightcurve de-trended without allowing for the optimization factor A_f at the top (plotted at the top at an arbitrary offset) and with optimization factor $A_f = 1.15$ for the low frequencies and $A_f = 1.05$ for the high frequencies, shown at the bottom. The introduction of an optimization factor improves the SNR of the de-trended lightcurve from SNR $= 30.0$ to SNR $= 30.7$. For this particular run improvements of up to 7% in SNR were achieved by optimizing the de-trending.

Note that, while we used smoothed versions of our lightcurves to identify the trends and to optimize the de-trending, we do not smooth or filter our lightcurves to improve the SNR, thus preserving all intrinsic features (including potential occultations). Figure 2.4 shows the power spectrum of one of our lightcurves before

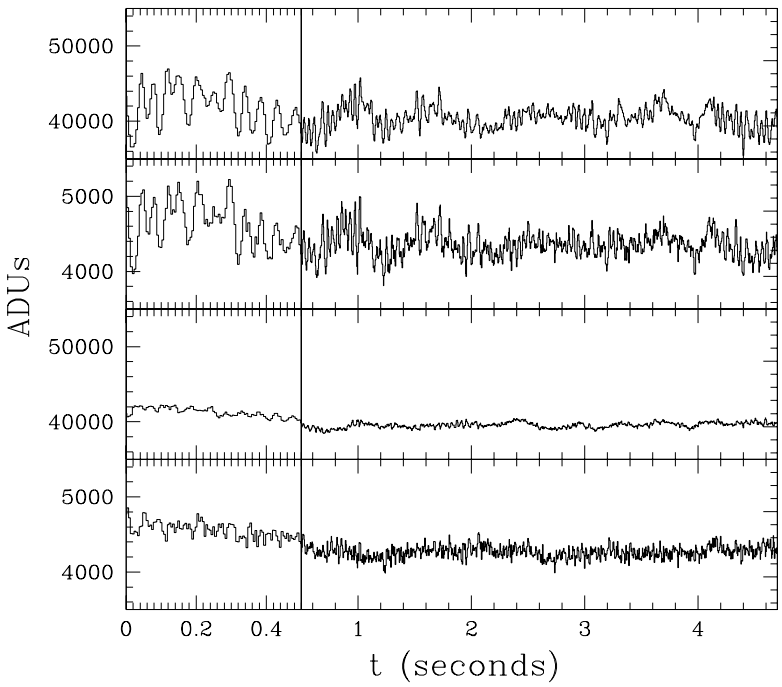

Figure 2.6: Lightcurves of two independent stars in one of our fields. The left-hand plots show a 0.5-second chunk of the time series; the following 4-seconds are shown on the right at a lower time resolution. The top two panels show the lightcurves before de-trending. Common modes are visible at multiple time scales. The bottom two panels show the lightcurves after de-trending. The top lightcurve is the same used in Figure 2.4

and after de-trending it (top). The power spectrum of an occultation time-series generated by a 1 km KBO occulting a F0V star of magnitude $V = 12$ is shown in the bottom panel. Our de-trending greatly reduced the power at all frequencies: the cumulative power for this particular lightcurve at frequencies $\nu \leq 40$ Hz is suppressed by a factor of 40. Because the oscillations are not perfectly correlated among our stars (see Section 2.4) some residual power is visible. Smoothing however would would significantly reduce the strength of the occultation features, that show power at all frequencies $\nu < 20$ Hz.

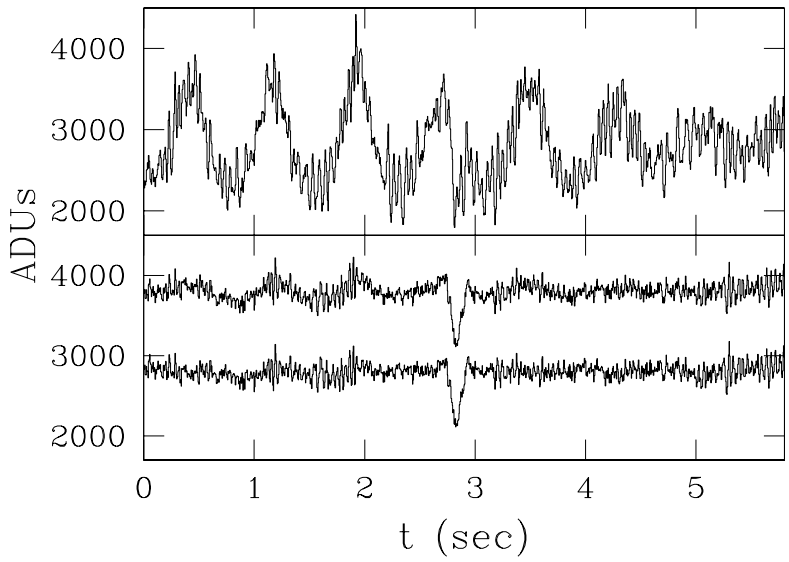

Figure 2.7: Raw lightcurve on which the occultation signature of a 1 km KBO occulting a magnitude $V = 9$ F0V star has been implanted (top) and the same lightcurve after de-trending (bottom). In the bottom panel the top lightcurve is de-trended without optimization (plotted at the top at an arbitrary offset) and the bottom lightcurve is de-trended with optimization factor $A_f = 1.15$ for the low frequencies and 1.05 for the high frequencies.

2.4 Residual noise in the time-series

With a SNR $\gtrsim$ 25 we can detect fluctuations of a few–percent. In an 0.005 sec exposure the flux for a magnitude $r' = 14$ star observed by Megacam is about 10^3 e^-, which after taking into account the contribution to the noise of the background should lead to a Poisson limited SNR of about 25. While we were able to remove a large portion of the noise that originally affected our data, we typically cannot reach the Poisson-limit. We have identified five possible sources of noise in our data:

- **Contamination by nearby sources**. Overlap of stars along the x axis (perpendicular to the read-out direction) within a chip, causes reciprocal contamination in our readout mode and some of the stars in our fields are therefore

compromised and excluded from our analysis. Furthermore, oscillations of the images along the x axis causes the relative distance between the star–streaks to change, which causes occasional merging. Note that while these oscillations are simultaneous in time domain, they do not occur in the same row in the recorded image. In each row the star images of two objects that are at a different y position on the CCD plane will not belong to the same time-stamp, therefore the oscillations – while simultaneous – will show a y offset. This is shown in Figure 2.8. The merging of streaks causes artificially high counts. Aperture photometry with a fixed aperture does not address this issue properly and fitting photometry on individual streaks is a computationally expensive, inefficient method which is also unstable in the presence of multiple sources close to each other.

- **Unresolved sources**. Sources that are too faint to be visible in our 0.005 sec exposures generate a diffuse background. For the data in Figure 2.3 the sky level calculated as the $3\sigma-$clipped mean of the row counts is 140.5 ADUs. The stare mode image sky level was 48 ADUs for a 5 sec exposure, which would lead to a prediction of 110 ADUs for our 0.005×2304 sec effective continuous–readout exposure. The discrepancy is due to the presence of unresolved streaks associated with faint stars across the field. Summing all the counts in the stare mode image and rescaling by the exposure time of each row we get a number very close to the sum of all counts in a row of continuous-readout data. This contamination introduces extra Poisson noise, but more importantly it introduces non-Poissonian noise as well, since the unresolved sources are affected by the same trends the bright stars display. Our data shows evidence of off–phase correlation that might be induced by unresolved sources.

- **Positional dependency in the motion and trends**. While we treat all of the stars in the field as an ensemble that moves in a solid fashion along the x and y axes, the image motion might also have a rotational component. This would lead to position dependencies in the motion that are not accounted for by our aperture centering algorithm. We have not seen evidence of dependency on the distance to the center of the focal plane in either motion or trends, but we cannot exclude that occasional rotational modes of the telescope would occur. Differential image motion and flux fluctuations might also be induced by atmospheric seeing. Both of these effects might cause the star–streak to move out of the photometric aperture leading to artificially low counts. The aperture size must be chosen to be such that errors due to contamination by nearby sources and errors due to streaks exiting the aperture are simultaneously minimized. Furthermore in the presence of thin clouds, variations in the transparency might generate trends that would affect different sources at different times as the clouds move across the image. Positional dependencies or variations in transparency might contribute to the off–phase correlation of our data.

- **Scintillation**. Young's scaling law (Young, 1967),

$$\sigma \;=\; \frac{0.09A^{2/3}(\sec Z)^{1.75}exp(-\frac{h}{h_0})}{\sqrt{2\ \Delta t}}, \tag{2.8}$$

  describes the error due to the low–frequency component of scintillation, with $\sigma = (\Delta I/I)$ and where A is the telescope aperture, Z the angle from zenith, h is the height of the turbulence layer, and ΔT the integration time. Competing effects are in place in our survey: the large aperture mitigating the noise, and the low air mass contributing to noise degradation. Using the above

equation and representative data from La Palma (Dravins et al., 1998) we estimate that the noise contribution from scintillation is $\sigma_I \leq 0.01$, i.e., not the dominant source of residual noise. Note however that this relation holds for integration time on scales of seconds or longer. When including the effects of high–frequency scintillation the dependency on the aperture is expected to be steeper:

$$\sigma_I^2 \propto A^{-7/3}(\sec Z)^3 \int_0^\infty C_n^2(h)h^2 dh, \tag{2.9}$$

where C_n is the refraction coefficient for the turbulent layer (see Dravins et al. 1997 and references therein).

As compared to the other occultation surveys the term associated to the telescope aperture ($A^{-7/6}$) in the SNR variance is a factor 20 lower than the same factor for the TAOS survey, 4.5 times lower than the same factor for Bickerton et al. (2008) and 1.4 than for the Roques et al. (2006) survey.

- **Convolution of the time series with finite PSF**. The finite size of the PSF (typically two to three pixels, although it occasionally was as large as seven) causes consecutive measurements to be correlated. This effect is not a source of noise *per se*, but it changes the spectral characteristics of the noise. The scale of this phenomenon shows up in an auto-correlation analysis with high power at a lag of about seven pixels. This is effectively a kernel convolution of our time series that smooths the signal, including possible occultation signals, so that while we sample the images at 200 Hz we would expect an occultation signature to be effectively sampled at ≈ 30 Hz (see Section 2.5). Note that this is close to, but slightly short of, the critical Nyquist sampling for occultations dominated by diffraction (Bickerton et al., 2009).

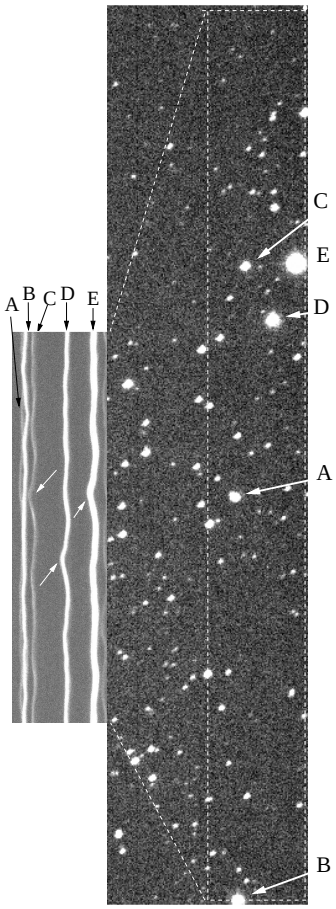

Figure 2.8: A stare mode image (right) read out from a single amplifier and a corresponding ~ 10 second chunk of high frequency data (left). A few bright stars and the corresponding streaks are indicated by letters. White arrows in the left panel point to a distinctive synchronous displacement feature in the data, visible clearly in three of the streaks, in order to focus the reader's attention to the non-parallelism of simultaneous features in our data, which is due to offset in the original y position.

While we achieved significant noise reduction with our de-trending, our SNR is typically a factor of two to three lower than the Poisson–limit. Our noise is characterized by high kurtosis, which is indicative of non–Gaussianity. Residual low frequency fluctuations (about 100 points period) are still noticeable in many of our time series (see Figure 2.6). Possible improvements are discussed in Section 6.1.

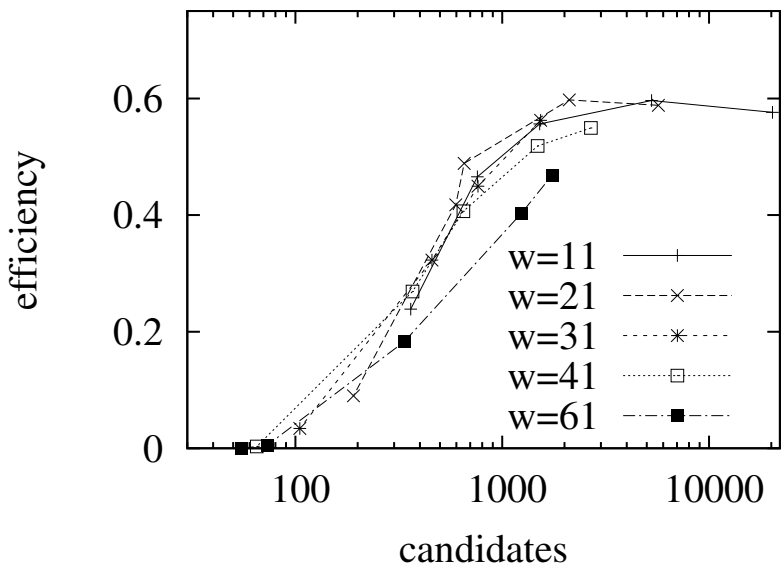

Figure 2.9: Efficiency plotted against the number of unidentified candidates (mostly false positives). Each line represents a different window size w, and each point represents the value of the efficiency at threshold θ = 0.08, 0.10, 0.15, 0.20, 0.30, the number of false positives monotonically grows with decreasing θ (larger values of θ on the left). All lines (all w values) show a plateau at different thresholds.

2.5 Search for events and efficiency

2.5.1 Detection algorithm

The signature of an occultation, sampled at any rate $\gtrsim$ 20 Hz, is very distinctive: it shows several fluctuations prior to the Airy ring peak, then a deep trough and possibly a Poisson spot feature, followed by a second Airy ring rise and more fluctuations (see Figure 1.5). The prominence of these features depends upon the magnitude and spectral type of the background star, which together determine the angular size, as well as the size and the sphericity of the occulter, distance to the occulter, and impact parameter (Nihei et al., 2007).

One possible approach to detecting occultations in our lightcurves is to take advantage of this peculiar shape, for example using correlation of templates, as in

Bickerton et al. (2008). Given the size of our dataset, however, we chose to utilize a search algorithm general enough to capture any fluctuation of some significance, but which requires less computational power. We scan our time series for any fluctuation lasting longer than a duration w, and on average greater than a threshold θ from the local mean, which is calculated over a window W of 300 data points surrounding w. Windows w of 11, 21, 31, 41 and 61 points were considered, in combination with thresholds of 0.10, 0.15, 0.20, 0.30. We define the local intensity $I_{\rm l}(i)$ as the ratio of the flux in the local window w and in the surrounding window W. If the flux in w is suppressed by more than our threshold θ from the local mean (mean over W),

$$I_{\rm l}(i) \;=\; \frac{\sum_{j=i-w/2}^{i+w/2} f_j/w}{\sum_{j=i+W/2}^{i+W/2} f_j/W} \leq 1 \;-\; \theta, \tag{2.10}$$

then w is considered as a candidate. This is similar to the Equivalent Width algorithm, which is used in spectral analysis, and for rare event searches by Roques et al. (2006) and Wang et al. (2009). Overlapping candidates are then removed and the center of the window w that displayed the largest deviation is selected as a single candidate event. Note that this algorithm would in most cases trigger two separate events for the two halves of an occultation on opposite sides of the Poisson spot (Figure 1.5). These cases are later automatically recognized and accounted for as a single event. Different choices of w and θ will produce different detection efficiency and false positive rate. We select an optimized subset of combinations of w and θ to be used for our event detection. This optimization is described in the next section.

2.5.2 Efficiency

We test the efficiency of our search by implanting simulated occultations in our raw lightcurves. By using our true dataset instead of generating synthetic data we do not introduce any assumptions about the nature of our time series. We run the implanted lightcurves through the same pipeline as the original lightcurves: de-trending them and searching for significant deviations from the mean flux. In order to achieve better sampling of our efficiency the entire dataset was implanted with one occultation per lightcurve at each KBO size we tested:

$$D = 0.5, 0.6, 0.7, 0.8, 0.9, 1.0, 1.3, 2.0, 3.0 \text{ km}, \tag{2.11}$$

and the efficiency was assessed for each size separately. The finite PSF width of the star induces correlations among consecutive time stamps. Given the typical PSF size in our data (see Figure 2.5) measurements are considered independent if separated by more than about seven pixels. Therefore, to modulate the original time series by the occultation signal we multiply the star flux by a synthetic occultation lightcurve sampled at 30 Hz.[5]

For the purpose of our efficiency simulations we assume all objects are at 40 AU, since we expect our occultations to be within the Kuiper Belt. There is little difference in the diffraction feature between 35 and 50 AU. The differences in spectral power between the star types do not impact the occultation features as

[5]Since the occultation typically suppresses the flux, multiplying by the occultation signal reduces the noise by a factor proportional to the occultation flux decrease, causing us to overly suppress the Poisson noise by a factor of the square root of the modulation. Furthermore, sources of noise that are not proportional to the photon counts (such as sky background and read noise) should remain constant during an occultation event, but this noise is reduced by a factor of the flux modulation when the event is added to the lightcurve in this way. However, since we expect to have a very high recovery efficiency for any occultation which generates effects $\geq 20\%$, where the underestimation would become significant, we do not expect this effect to impact our efficiency estimation.

observed by our system, so we simulate all of our occultations assuming an F0V type star. The angular size of the star affects the shape of the occultation by smoothing the diffraction features. It is therefore important to properly sample the angular size space. We find that, given the objects in our fields, imposing a flat prior to the magnitude distribution between $V = 8$ and $V = 11$ adequately samples our angular size range. The flat prior slightly overestimates the average cross section H of the events, but this effect is more than compensated by the loss in efficiency due to the fact that, for stars with larger angular sizes, the occultation signal is smoothed out as the diffraction pattern is averaged over the surface of the star, making the event harder to detect (Nihei et al., 2007). Overall our estimate of our detection rate is conservative.

To characterize our efficiency we implant occultations at random impact parameters $b \in [0, H(D)/2]$. However, we first want to choose the most appropriate window size and threshold combinations, and for that we implant occultations by $D = 1$ km KBOs in the reduced impact parameter space $b \in [0,\ 0.3 \cdot H(D)]$. This set of modified lightcurves is used to optimize our parameters to maximize our efficiency and minimize the number of false positives simultaneously. Although our generic detection approach can reach high efficiency (nearly 100% for 1 km KBOs at zero impact parameter), it also produces a large number of candidates, most of which are expected to be false positives. The combination of w and θ values generated efficiencies ranging between 94% (at w=11 and $\theta = 0.1$) and 0 (at w=61 and $\theta = 0.3$) and the number of candidates ranged between 0 and over 1000. Figure 2.9 shows the behavior of the efficiency as a function of number of candidates. Different window sizes are represented by different lines and the different thresholds are marked by the points along each line. Typically, after a rapid increase in efficiency with the decreasing threshold, the efficiency stabilizes, while the number of candidates keeps

growing: we want to choose our parameters near this point, where the efficiency is highest and any less stringent choice would only increase the number of our false positives. We select combinations of w and θ that yield both an efficiency $> 50\%$ and a ratio of efficiency to candidates < 0.5. The following are the accepted windows-threshold combinations: $(w,\ \theta) = (21,\ 0.15)$, $(31,\ 0.20)$, and $(11,\ 0.25)$. Events found in any run with these selection parameters were considered as candidates. We reached an overall efficiency of 82% at $D = 1$ km for lightcurves implanted with synthetic occultations at varying impact parameters between 0 and $H/2$.

The efficiency of our search is summarized in the top panel of Figure 2.10, as a function of KBO size. We also plot the corresponding effective solid angle $\Omega_{\rm e}(D)$, defined as:

$$\Omega_{\rm e}(D) = \sum_{*} \frac{H(D,\theta_*)}{\Delta}\ \frac{v_{\rm rel}}{\Delta}\ T_*\ \epsilon(D,\ \theta_\star), \tag{2.12}$$

where $H(D,\theta_*)$ is the cross section of the event, which depends on both the diameter of the KBO and the star angular size as indicated by θ_*; $v_{\rm rel}$ is the relative velocity of the KBO, which depends on the elongation angle which is close to opposition for all of our observations (relative velocities ranging between 24 and 25 km s^{-1}); Δ is the distance to the occulter (assumed to be $\Delta = 40$ AU), T_* the exposure for the star target (duration of the lightcurve), and $\epsilon(D,\ \theta_\star)$ the recovery efficiency for that diameter: $\epsilon(D,\ \theta_\star) = 1$ if the implanted event was recovered, 0 otherwise. The sum is carried out over all of our lightcurves with $SNR \geq 25$. $\Omega_{\rm e}(D)$ represents the equivalent sky coverage of our survey for targets at diameter D, accounting for a partial efficiency. The center panel of Figure 2.10 shows the effective solid angle as a function of diameter. The bottom panel shows the effective solid angle multiplied by bracketing slopes for the size distribution: D^{-4} and D^{-2}, and it indicates the

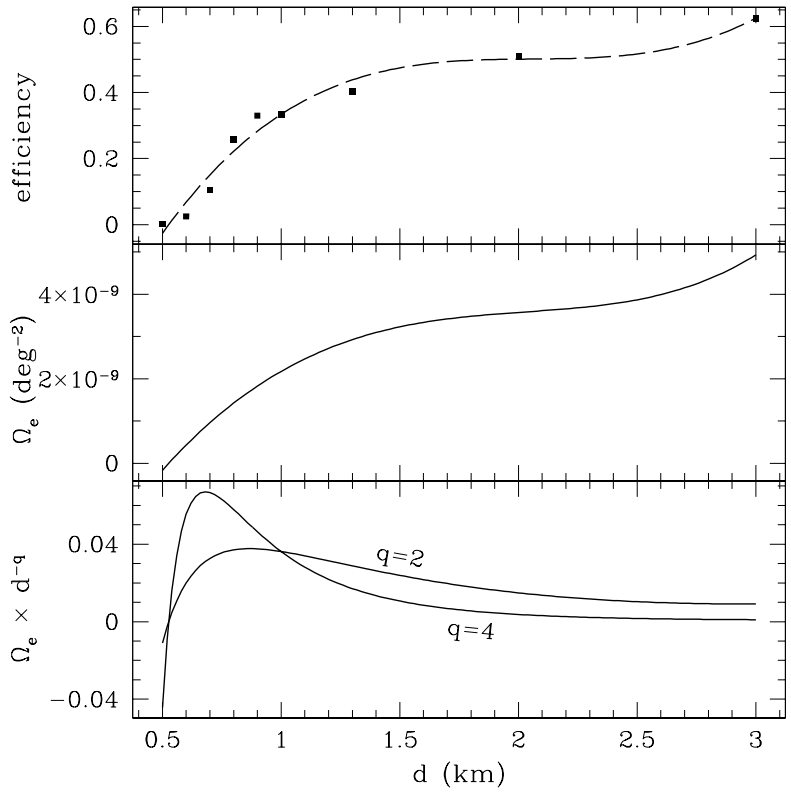

Figure 2.10: Efficiency of our survey as a function of KBO diameter (*top*). The *central* panel shows the effective solid angle of our survey and the *bottom* panel the effective solid angle multiplied D^{-2} and D^{-4}.

survey expects to see the largest number of detections near $D = 700$ m.

2.5.3 Rejection of false positives

At this stage we have more than a thousand candidates. However, most of the false positives can be removed in an automated fashion: we reject fluctuations that appear simultaneously in more than one lightcurve; those are most likely due to local weather or atmospheric patterns that were not corrected in the de-trending phase because they only affected a subset of lightcurves, and can be ruled out as serendipitous occultations. We also reject any fluctuation that does not have the right combination of depth and width. We empirically investigate the relationship

between the depth and the width of an occultation by a KBO, as it is seen by our system, taking advantage of our simulations. To define the depth and width of the events we fit synthetic occultation lightcurves with inverted top-hat functions with parameters δ (depth) and γ (width). Figure 2.11 shows the best fit values δ and the γ for occultations simulated in the diameter range $D = 0.1$ km to $D = 3.0$ km, impact parameters $b = 0$ to $H/2$ and magnitude range 8 to 11 for F0V stars (the same set that we used for our implantation with additional occultations from objects $D < 0.5$ km). The shaded region represents the area of this phase space where at least one occultation was best fit by parameter values δ and γ (and the intensity of the shade reflects the frequency of $\delta-\gamma$ best fits). We can automatically reject events outside the dashed polygon as incompatible with $D \leq 3.0$ km KBO occultations.[6] We are not sensitive to events shallower than a 10% flux drop.

At this point the absolute number of candidates is small (25). The remaining candidates are inspected visually (using DS9, Joye & Mandel 2003), and the lightcurves are extracted with a different photometric method (based on IRAF). All remaining candidates prove to be artifacts, mostly due to photometry. No candidates are left after this elimination process.

2.6 Upper limit to the size distribution of KBOs and scientific interpretation

We now compare our limit to the size distribution of KBOs to that of Bickerton et al. (2008). Bickerton et al. (2008) derived an upper limit to the surface density of KBOs of diameter $D \geq 1$ km. They considered the data obtained by their

[6]Note that the duration regime over which we recover events extend as far out as our largest window: $W = 61$ points or 300 ms.

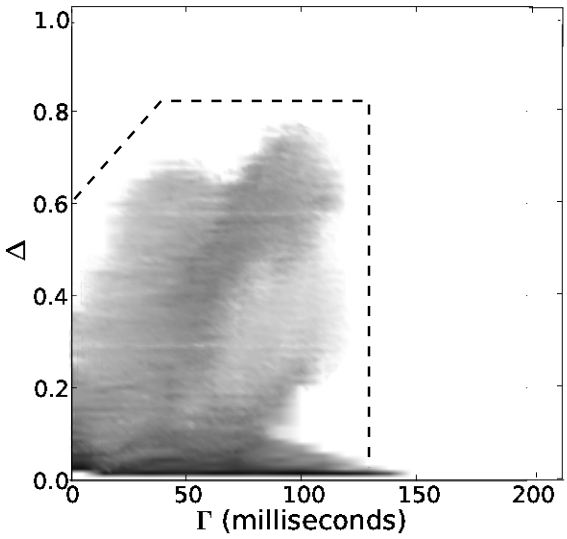

Figure 2.11: Phase space plot showing the regions of the *flux decrease–duration* space occupied by occultations by KBOs of diameter 0.1 to 3 km, as observed through the MMT/Megacam system bandpass. We simulated occultations from KBOs in the size regime 0.1–3.0 km, and we fit the occultations with an inverted top-hat function with parameters δ and γ. The intensity of the gray scale reflects the number of simulated occultations with best fit value δ and γ: white areas are void of occultations.

own survey together with the data published by Roques et al. (2006) and Chang et al. (2007), assuming 100% efficiency for each survey at 1 km, and obtaining a total effective coverage $\Omega_{\rm e} = 5.4 \times 10^{-10}$ deg^2. The cross section H used to calculate $\Omega_{\rm e}$ is set to validate the 100% efficiency assumption on a survey by survey basis. Our survey adds 7.0×10^{-9} deg^2 to the collective $\Omega_{\rm e}$, allowing us to derive a limit over an order of magnitude stronger than the limit set by Bickerton et al. (2008). Thus we set a comprehensive 95% confidence level upper limit on the surface density of $D \geq 1$ km KBOs at 40 AU of $\Sigma_N(D \geq 1 \text{ km}) \sim 2.0 \times 10^8$ deg^{-2}.

We can also derive a new upper limit for objects as small as 700 m, where our efficiency is ϵ ($D = 700$ m) $\sim$ 10%. We can set a 95% confidence upper limit of $\Sigma_N(D \geq 0.7 \text{ km}) \sim 4.8 \times 10^8$ deg^{-2}. These limits are shown in Figure 2.12, along with the TAOS model-dependent upper limit and the limit set by the RXTE X-ray survey.

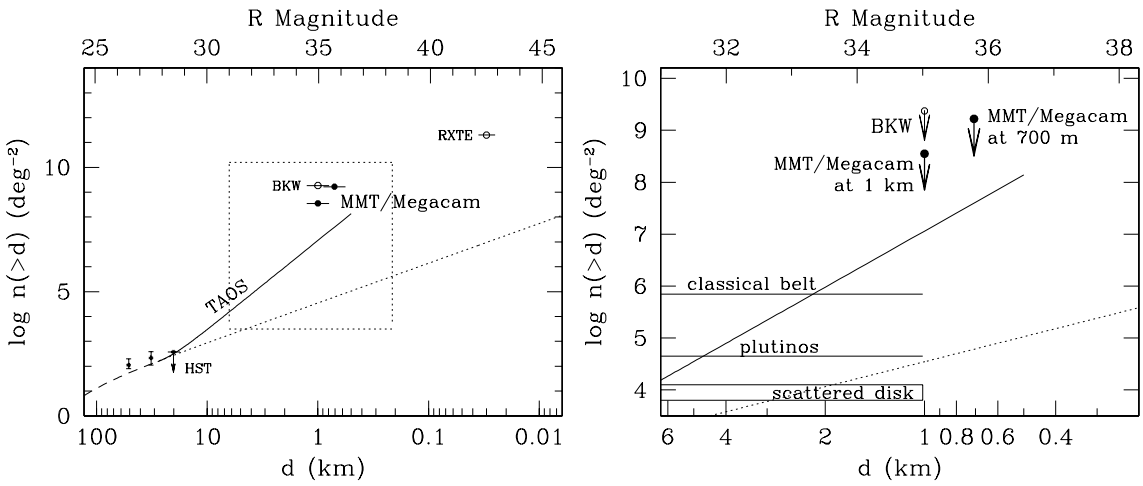

Figure 2.12: Upper limits to the surface density of KBOs. *Left panel.* The dashed line is the best fit to the Bernstein et al. (2004) survey, extrapolated to $D = 0.01$km. Three data-points reported by Bernstein et al. (2004) are plotted (HST, the faintest data from direct observations). The straight line is the TAOS upper limit to the slope of the small size end size distribution: $q < 4.6$ (Zhang et al., 2008). The result by Bickerton et al. (2008) is shown as an empty circle (BKW) as well as the X-ray result (Jones et al., 2008, RXTE). The upper limits set by our survey at $D = 1$ km and $D = 0.7$ km are shown as filled circles. The region relevant to our limit, enclosed in the square, is magnified on the right hand panel. *Right panel.* Upper limits to the surface density of KBOs, zooming in the 0.2–6 km region of the size spectrum where our survey can place limits. Symbols and labels are the same as for the left panel. The lower limits for JFC precursor populations are also shown (Levison & Duncan, 1997; Morbidelli, 1997; Volk & Malhotra, 2008).

2.6.1 Comparison with the results from the TAOS survey

Our survey aspires to be complementary to TAOS in that it potentially could detect objects as small as 300 m. However, at this stage of our work we are unable to push the detection limit below the TAOS sensitivity (500 m). Note that the recovery efficiency for TAOS at 700 m is $\epsilon_{\rm TAOS} \sim 0.3\%$, a factor of four lower than our efficiency.

The TAOS upper limit to the surface density of KBOs is presented as a model-dependent limit, under the assumption of a straight power-low behavior for the small end of the Kuiper belt size distribution; it is therefore not trivial to relate the two results, but it is clear that the number of star-hours a dedicated survey can

collect compensates for the loss in efficiency at the small size end, and TAOS is able to produce more stringent limits than our own. Our survey would however capture the details of the diffraction feature with exquisite sampling, while the information contained in the same occultation, as observed by TAOS, would be greatly reduced due to the slower sampling. This would allow us to set constraints on the size and distance of the occulter, while the size-distance-impact parameter space is highly degenerate in the TAOS data.

2.6.2 The Kuiper belt as reservoir of Jupiter Family Comets

The classical Kuiper belt, the scattered disk objects and the Plutinos have all been considered in dynamical simulations as possible reservoir of JFCs (see Volk & Malhotra 2008 and references therein). The inclination distribution of the JFCs strongly suggests a disk-like progenitor population, favoring the Kuiper belt over the Oort Cloud. Giant planets generate long term gravitational perturbations that causes weak orbital chaos, which explains the injection of comets to the JFCs region (Holman & Wisdom, 1993; Duncan et al., 1995; Levison & Duncan, 1997). The efficiency of this process depends on the dynamical characteristics of the progenitor family.

Simulations of the injection process lead to lower limits on the number of progenitors, which we can compare with our upper limit to the surface density of KBOs. Bernstein et al. (2004) discussed constraints on the progenitors of the JFCs on the basis of their HST/ACS survey. This survey is however only sensitive to objects greater than $\sim$ 20 km in diameter, while the precursors of the JFCs are likely to be in the size range $1 - 10$ km. This is the typical observed size of JFCs (Lowry et al., 2008) and it is likely that its progenitor population would consist of objects of similar size (or slightly larger) than the JFCs themselves.

In Figure 2.12 we show the lower limits to the KBO populations (classical belt and Plutinos) and scattered disk derived from dynamical simulations. We use the estimate of Levison & Duncan (1997) for a population of cometary precursors entirely in the classical Kuiper belt, of Morbidelli (1997) for Plutinos progenitors, and of Volk & Malhotra (2008) for a progenitor population in the scattered disk. As in Bernstein et al. (2004) we convert the population estimates for the Kuiper belt populations into a surface density by assuming for each population a projected sky area of 10^4 deg^2. Volk & Malhotra (2008) provide information on the fraction of time the objects in their simulation spend between 30 and 50 AU and within 3° of the ecliptic plane, and these fractions are used to calculate the minimum surface density of scattered disk objects expected in the region of sky typically observed by occultation surveys.

We are not presently able to exclude any of these populations as progenitors of the JFCs. Future occultation surveys, with improved sensitivity, should provide valuable information on the origin of JFCs.

Chapter 3

The TAOS survey and the 3.75-year dataset

We have analyzed the first 3.75 years of data from TAOS, the Taiwanese American Occultation Survey. TAOS monitors bright stars to search for occultations by Kuiper Belt Objects (KBOs). This dataset comprises 5×10^5 star-hours of multi-telescope photometric data taken at 4 or 5 Hz. No events consistent with KBO occultations were found in this dataset[1].

3.1 Introduction

The Taiwanese American Occultation Survey (TAOS) has been operating since 2005 with two, three, and now four telescopes simultaneously taking stellar photometry at 5 Hz[2]. The analysis of the first two years of TAOS data was described

[1] This work, together with Chapter 4, was accepted for publication by the Astronomical Journal under the title *The TAOS Project: Upper Bounds on the Population of Small KBOs and Tests of Models of Formation and Evolution of the Outer Solar System*, and it is the product of a collaboration with the TAOS team and with M. J. Holman (Harvard-Smithsonian Center for Astrophysics)

[2] A small subset of early data was collected at 4 Hz cadence, comprising about 5% of the data analyzed in this work.

in Zhang et al. (2008, hereinafter Z08) and it reported no detections. An upper limit was derived to the slope of the small size end of the KBO size spectrum. The TAOS system is described in detail in Lehner et al. (2009b). Using 50 cm aperture robotic telescopes in simultaneous observations and observing with the relatively low cadence compared to all other KBO occultation surveys (Section1.4), TAOS was designed to address the km-size region of the KBO size spectrum. TAOS has collected over 99% of the occultation data in the literature, and we will show that the marginal sensitivity to sub-km objects is more than compensated by the very large exposure of our star targets. Here we consider the first 3.75 years of TAOS data, a significantly larger dataset than the one explored in Z08. With these data we are able to begin constraining Kuiper belt formation and evolution models.

In Section 3.2 I describe the new dataset and our analysis. In Section 3.3 I briefly describe our photometry and detection algorithms, as well as our efficiency analysis. I also discuss our recovery efficiency as a function of observational parameters, our observing strategy, and I discuss the most productive strategies for TAOS and the other occultation surveys. In the next chapter I will describe the limits that this survey is able to place on the outer solar system and on its formation and evolution models.

3.2 3.75 years of TAOS data

TAOS is a dedicated survey that observes at a cadence of 5 Hz. The primary scientific goal of the survey is to estimate or set constraints on the number of KBOs in the region of the size spectrum that is currently too small to be observed directly: $D \lesssim 10$ km.

Here we present an expanded analysis of three-telescope TAOS data[3]. These data consist of photometric measurements of target star fields collected synchronously with all three telescopes. The dataset analyzed here was collected between January 2005 and August 2008. In a previous analysis of a subset of these data, Z08 reported an upper limit to the size distribution of KBOs under the assumption of a single power law for small KBOs. If one models the size distribution for objects smaller than $D = 28$ km, the smallest direct observation (Bernstein et al., 2004), as a single power law $dn/dD \propto D^{-q}$, where n is the surface density of objects, the slope of the distribution is limited to $q \leq 4.6$.

Throughout the remainder of this paper, a *data run* refers to a set of data collected in a uninterrupted observation of any field. For a single star in the field a set of three lightcurves belonging to one data run will be referred to as a *lightcurve set*, and each three-telescope measurement, at a single time point, will be referred to as a *triplet*. A *star–hour* refers to an hour of high-cadence, multi-telescope observations on a single target star.

The data set described in this paper amounts to amount to 5.0×10^5 star–hours, while the data set used in Z08 comprises of 1.5×10^5 star–hours. The details of this dataset, and of the dataset published in Z08, are summarized in Table 3.1. Over 90% of our data is collected within 10° of the ecliptic plane in order to maximize the rate of occultations.

TAOS uses the *zipper–mode* technique to read out the CCD cameras at high frequency. This method, described in Lehner et al. (2009b), enables high speed observations across the 3□° field of view of the TAOS telescopes, but it artificially increases the crowding of the field and the background. In zipper–mode readout

[3]The fourth telescope, TAOS C, became operational in August 2008. The results presented in this paper are based on analysis of all of the three-telescope data collected to this point.

each star in the field is represented in a subsection of the output image – which we call *rowblock* and which comprises 76 rows for our 5 Hz data – so that the field of view is entirely imaged in each rowblock. Note that the images of different stars in a rowblock, however, do not necessarily belong to the same time-stamp. The zipper–mode readout boosts the sky background by a factor of 27 at a 5 Hz readout rate. This limits the sensitivity of TAOS to stars as faint as $M_{\rm TAOS} = 13.5$, for which a signal–to–noise ratio (SNR) of ~ 7 can be achieved in a dark night. The magnitude and SNR distributions for the target stars in our survey are shown in Figure 3.1. On the left panel, the $x-$axis is the TAOS instrumental magnitude $M_{\rm TAOS}$, which is defined by a regression on the USNO-B magnitudes to be similar to $R_{\rm USNO}$. The correlation between instrumental magnitude and SNR is shown in Figure 3.2. The scatter in the relationship between SNR and $M_{\rm TAOS}$ is due to both changes in the sky background and in the weather conditions, and to different degrees of crowding in the fields. In Figure 3.3 we show the number of star–hours at different angles from opposition. The top scale indicates the velocity of a KBO at the center of a field at this elongation. We cover a large range of opposition angles; our field selection algorithm favors ecliptic fields near zenith. Most angles are positive because the weather at the site tend to improve after midnight. The effects of the angle from opposition on our efficiency and event rate, as well as the efficiency as a function of magnitude and crowding are discussed further in Section 3.3.5.

3.3 Analysis

In this section we describe the steps of the data analysis procedure, from photometry to efficiency simulations. In Section 3.3.1 we briefly describe the photometry package we developed to obtain lightcurves from our CCD images; in Sec-

Table 3.1. TAOS dataset parameters (3–telescope data)

	Z08	this work
Start Date	2005 February 7	2005 February 7
End Date	2006 December 31	2008 August 2
Light-curve Triplets	110,554	366,083
Exposure (star–hours)	152,787	500,339
Measurements[a]	7.8×10^9	2.7×10^{10}

[a]Individual telescope measurements.

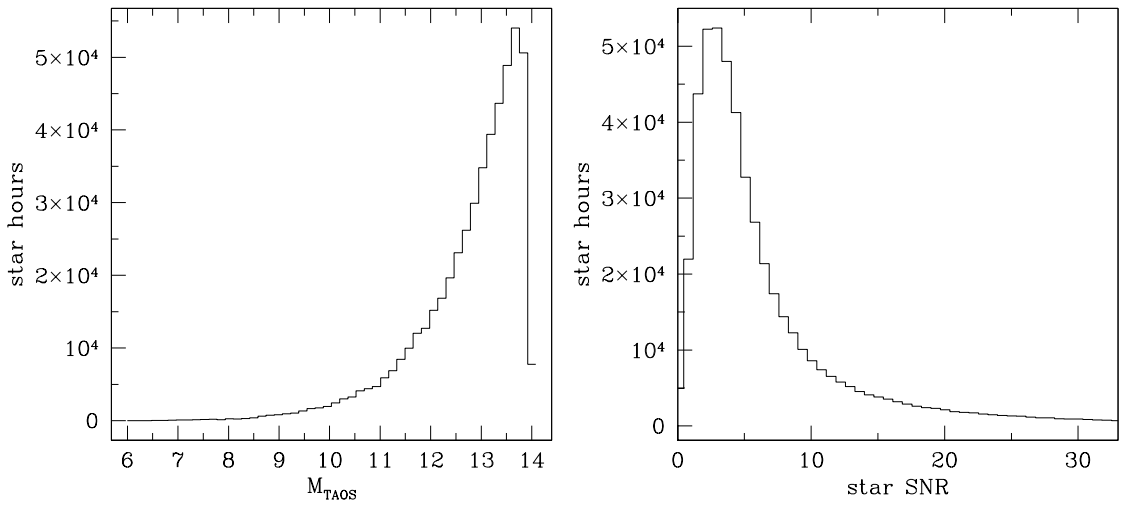

Figure 3.1: Distribution of magnitudes for the TAOS target stars, (bin size 0.16, left). SNR for the TAOS target stars, averaged over the duration of a run and over the three telescopes (bin size 0.73, right). A few targets at greater SNR and brighter magnitude, amounting to $< 5\%$ of the data, are not shown.

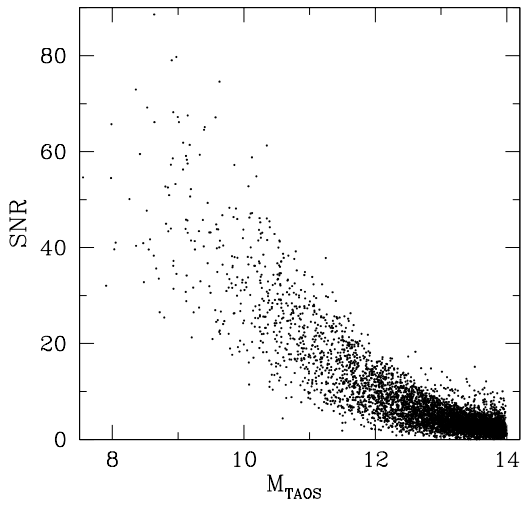

Figure 3.2: SNR versus TAOS instrumental magnitude $M_{\rm TAOS}$; only a random sample of 1% of all stars is shown for clarity.

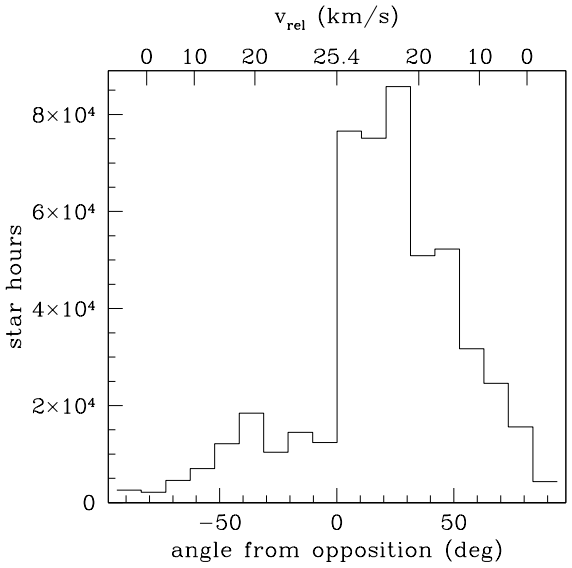

Figure 3.3: Distribution of angles from opposition for the TAOS targets. The top axis shows the relative velocity of a KBO at 43 AU, given the position of the field. The bin size is 10.5°.

tion 3.3.2 we describe our detection algorithm and the rejection of false positives. We then describe the efficiency tests: in Section 3.3.3 we show how we simulate occulation events to implant in our lightcurves, and in Section 3.3.4 we describe in detail how we identify the angular size of our target stars to simulate occultations correctly. In Section 3.3.5 we describe how we implant the occultations in our lightcurves and test the efficiency parameters, and finally in Section 3.3.6 we analyze the behavior of our efficiency as a function of various parameters relative to the occultation and the observing strategy.

3.3.1 Photometry

In order to detect occulations we need to identify brief flux changes in a star simultaneously observed by all telescopes. A custom aperture photometry package has been developed in order to analyze the zipper–mode TAOS images (Zhang et al., 2009). TAOS photometry is conducted in three phases: star identification and magnitude assignment, determination of the aperture size, and photometry.

In order to identify the star targets we collect conventional, or *stare–mode*, images of our target field at the beginning of each observing run. These images are analyzed using SExtractor (Bertin & Arnouts, 1996). The sources thus extracted are identified with USNO-B catalog sources (Monet et al., 2003) using the WCS tools (Mink, 2006). A magnitude regression between USNO-B R2 and the instrumental magnitude is computed for all stars with a USNO-B counterpart that are brighter than $M_{\mathrm{TAOS}} = 13.5$: those are hereinafter identified as targets.

Next, the best aperture size for each target star is empirically determined. Because of the problems caused by the artificial crowding of the zipper–mode images a different aperture size for each star is chosen so as to minimize contamination. For each star the SNR of the star is evaluated as a function of aperture size for the first

$\sim$ 1000 time-stamps and the size that generates the best SNR is chosen for that star. In this fashion, wherever near–by star images would contaminate the target, the aperture is naturally chosen conservatively. Square apertures are employed to increase the computational efficiency.

The initial position of the aperture for every target is estimated from the stare–mode image. Corrections are made to the aperture centers from time-stamp to time-stamp to account for small translational or rotational displacements of the field. The sky is estimated as the mode of the flux in each column in each rowblock, and then it is subtracted from the star flux. Note that the zipper–mode readout induces excess counts in the columns where bright stars are located since the charges are transferred with the shutter open between each exposure. Estimating the background column by column allows us to remove the sky background as well as the excess flux in these *streaks*. Time-stamp by time-stamp the flux for each targets is thus collected, composing a photometric time series for each target star.

3.3.2 Detection and false positive rejection

The *Fresnel scale* is defined as $F = (\lambda\Delta/2)^{\frac{1}{2}}$ where λ is the wavelength of observation, and Δ the distance to the occulter (Roques et al., 1987; Born & Wolf, 1980). For optical observations at the distance of the Kuiper belt (about 43 AU) the Fresnel scale is $F \approx$ 1.4 km. Diffraction effects are therefore important in the events that we are seeking. Occultations are manifested in the lightcurve of an observed star as an alternation of bright and dark features, typically with an overall suppression of the flux. Theoretical occultation lightcurves are shown in Figures 3.4 & 3.5. The signature of an occultation by a KBO of sub-kilometer size has a typical duration of about 0.2 second at opposition, and about a second near quadrature. A typical KBO occultation is then expected to result in the suppression of the flux for one

or a few consecutive points in a TAOS lightcurve. In order to ascertain the extra-terrestrial origin of a dip in a lightcurve TAOS observes simultaneously with multiple telescopes. This allows us to rule out, on the basis of simple parallax considerations, atmospheric scintillation phenomena which might mimic an occultation event and which could be a source of false positives in occultation surveys, as well as any non-atmospheric phenomena such as birds, airplanes, etc.

The statistical significance of a simultaneous low point in our lightcurves can be assessed rigorously, and the probability of a low measurement being drawn out of pure noise decreases with the number of telescopes observing the target, provided that the measurements for the telescopes are independent. The lightcurves are high-pass filtered to remove trends due to weather patterns and changes in atmospheric transparency. High-pass filtering the lightcurves preserves the information on time-scales relevant to occultation phenomena (one or a few points in a time series). The implementation of the filter is described in Z08. The filter produces a time series in which $h(t)$, the measurement taken at time t, represents the deviation from the local mean of the lightcurve in units of local standard deviation. Any run where the independence of the measurements after filtering cannot be rigorously established is removed from our dataset (Lehner et al., 2009a).

To detect events we rank–order the photometric measurement in each of our light-curves, from the lowest to the highest flux, independently for each telescope (labeled A, B and D). The i-th point in a lightcurve will be associated to rank $r_i^{\rm T}$ for telescope T. We then consider the rank triplets $(r_i^{\rm A},\ r_i^{\rm B},\ r_i^{\rm D})$. The probability distribution of the quantity $z_i = -\ln\{r_i^{\rm A}\ r_i^{\rm B}\ r_i^{\rm D}/N_{\rm p}^3\}$, with $N_{\rm p}$ the number of points in the lightcurve set, can be determined combinatorially. Knowing this, under the null hypothesis that there is no event in the triplet i, we can compute the probability for a random variable Z arising from this distribution $P(Z > z_i) = \xi$.

We set a threshold such that we expect fewer than 0.27 events in our dataset that are due to random fluctuations. For the dataset discussed in this paper we accept as events all data points that produce a rank product less likely than $\xi = 3.0 \times 10^{-11}$ to be drawn from a random distribution. Note that events generated by large KBOs, or for observations near quadrature, would affect more than one point in the lightcurve (Figure 3.5), and our rank–based search algorithm is most efficient when the dip in the lightcurve is isolated. Therefore, in addition to searching for single–point events, we also bin our lightcurves by 2, re-rank them and repeat the statistical tests described above. The probability of each data point is assessed for both unbinned and binned lightcurves. Each lightcurve is binned twice, with two different starting points. This increases the detectability of occultations by large KBOs and by KBOs transiting with low relative velocity. For a detailed discussion of our statistical analysis see Lehner et al. (2009a).

For a set of lightcurves of a given star, the ranks in the three telescopes should not be correlated for the statistical analysis described above to be valid. A three-dimensional scatter-plot of the rank triplets should thus uniformly populate a cube. We have devised two statistical tests to assess the quality of a data run which are based on this requirement. First, for each lightcurve set we divide the scatter-plot into a three-dimensional grid and count how many rank triplets are in each element. We expect the number in each element to be equal, and we thus compute a Pearsons χ^2 statistic to measure how far the distribution deviates from the expected uniform distribution. If any data runs show a significant deviation from the predicted distribution, the entire data run is rejected. Second, we are particularly concerned with any correlation which would produce a bias toward simultaneously low ranks. We thus look at the data in the grid element with the lowest ranks in all telescopes. The number of rank triplets in this grid element

follows the hypergeometric distribution (Rice, 2006, pg. 39). Once again, we test to see if the number of triplets in this grid element follows the predicted distribution for all of the lightcurves, and once again we reject any data run which shows a significant deviation. These tests will be described in detail in Lehner et al. (2009a). After removing the data runs that do not fulfill our independence requirement we have 8×10^5 star–hours of data.

For the next step we relax considerably the ultimate significance requirement described above, and select as *provisional candidates* those triplets that have $\xi \leq 1.0 \times 10^{-6}$. Note that the significance ξ refers to the probability that the point would be drawn from a random distribution, therefore the lower the value of ξ the higher the statistical significance of the event. Nearly 150,000 provisional candidates are found. We use all these measurements to identify and remove spurious regions of the lightcurves, and hence identify and reject false positive events which arise from sources other than random chance. The constraints described below allows us to recognize regions of lightcurves with atypical noise and contamination by transiting objects (satellites or meteors, which turn out to be the major source of false alarms), and to identify high-frequency fluctuations in the raw data that are not removed by the high-pass filter. These are the steps of our false positive rejection process:

- *Contiguity:* Contiguous candidates within a lightcurve and candidates that are within three time-stamps of each other are removed. Only the one rank triplet that has the highest significance in a series of contiguous or proximate points is considered as a candidate. This removes double–counted events: events caused by large KBOs or KBOs moving at low relative velocity would affect more than one contiguous point. Furthermore this removes events that are double–counted because they appear significant in both the binned and unbinned lightcurves. This eliminates about 40% of the candidates.

- *Simultaneity:* Candidates that appear in the lightcurves of more than one star simultaneously at the same time-stamp *or* within three rowblocks are considered to be false positives. We expect simultaneous count drops in time-domain to be primarily due to inaccurate aperture positioning in the photometry. In the rowblock domain simultaneous count drops might be due to inaccurate background determination or non-occultation events altering the baseline of the lightcurve at, or around, the candidate event, or by fast moving cirrus clouds or other phenomena which induce high frequency fluctuations in multiple lightcurves which are not removed by the high-pass filter. This cut removes about 60% of the remaining candidates.

- *Number of telescopes:* At this point we require all of our remaining candidates to have been observed by all three telescopes. Although we are only considering three-telescope runs in our analysis, for some targets the lightcurve might not be extracted in the photometry phase for all telescopes. Small differences in the field of view and in the field distortion might make one star target not visible to all telescopes if it is at the edge of the field or if the crowding induced by the zipper–mode readout caused overlap of the target with other stars (Lehner et al., 2009b). About 35% of the remaining candidates are thus removed. At this point there are still over 20,000 candidates left. Note that we do not count the star hours discarded by this cut in our total exposure of 5×10^5 star–hours.

- *Significance threshold:* We finally constrain ξ such as to expect fewer than 0.27 false positives in our dataset. This constraint depends on the size of the dataset: for the 9×10^9 triplets remaining $\xi < 3.0 \times 10^{-11}$ allows < 0.27 false positives due to random noise. Only 228 candidates remain.

The remaining candidates require visual inspection: first of the lightcurves, and for any remaining candidates, of the images. Most of the events are caused by the passing of bright objects, such as artificial satellites, meteorites or asteroids, that generate a variation in the background or baseline of the lightcurve responsible for causing artificially low counts in the neighborhood of the object. Many, but not all, of these false positives are removed by the simultaneity cut described above. In the presence of a bright object overlapping with a star–streak generated by the zipper–mode readout, the brightness of the streak is overestimated, thus too much flux is subtracted from the rowblock column causing an artificial flux drop in the star time series. In many instances the foreground object will also appear inside the star aperture artificially boosting its brightness. This flux drop will then be associated with a very high flux measurement following or preceding the event epoch, a signature that allows us to remove these false positives by inspecting the lightcurve. We also inspect the centroid position of the aperture. If the aperture position has moved significantly at the time-stamp of the candidate the candidate is rejected. Of the remaining candidates, 90% are rejected by visual inspection of the time series.

Finally we inspect the *images* of the remaining 23 candidates: they also were all associated with bright moving objects overlapping star streaks. No candidate events were left in our dataset at the conclusion of this process.

3.3.3 Occultation event simulator

It is necessary to assess the efficiency of our recovery algorithm in order to derive the number density of KBOs from the number of events in our survey. In order to measure our recovery efficiency we implant our data with synthetic occultations. By implanting into the actual lightcurves we do not make any assumption regarding the nature of the noise in our data. Note that our detection algorithm,

described in Section 3.3.1, which is based on rank statistics, is not affected by the spectral characteristics of the noise, as long as the noise is stationary (Lehner et al., 2009a). It is important to correctly characterize occultations by all objects we might detect, and for this we need to properly characterize all of our target stars as well as the effects of our telescope and camera system. Here we describe the steps of our algorithms to generate synthetic occultation features to be implanted in our lightcurves. Our simulator is also described in Nihei et al. (2007).

For a spherical occulter, and under the plane wave approximation, the intensity of a point on a diffraction pattern is uniquely determined by four parameters: the wavelength λ, the distance to the occulting object Δ, the diameter of the object D, and the perpendicular distance, x, of that point of the diffraction pattern from a line that passes through the star and the occulter. We can uniquely describe the intensity at any point of an occultation pattern (or lightcurve) as a function of two dimensionless quantities $\delta = D/F(\lambda,\ \Delta)$ and $\eta = x/F(\lambda,\ \Delta)$, where F is the Fresnel scale (Roques et al., 1987, and references therein).

The calculation of the intensity pattern requires significant computational time, as a result of the highly oscillatory nature of the integrals involved in the calculation (Nihei et al., 2007). We therefore compiled a *diffraction table*: a binary file that contains the intensity as a function of δ and η. We can generate a theoretical diffraction lightcurve by interpolating in this table. A gray scale representation of the diffraction table is shown in Figure 3.4, along with an example of a diffraction pattern for a $D = 3.0$ km KBO. Note the following features in the diffraction pattern: the Airy peaks, the brightest fringes at $\eta = \pm 2.4$ ($x = \pm 3.36$ km), and the *Poisson spot*, the central brightening (Roques et al., 1987).

We also need to simulate our telescope and camera system. The TAOS system uses wide bandpass filters with an approximately constant response between 500

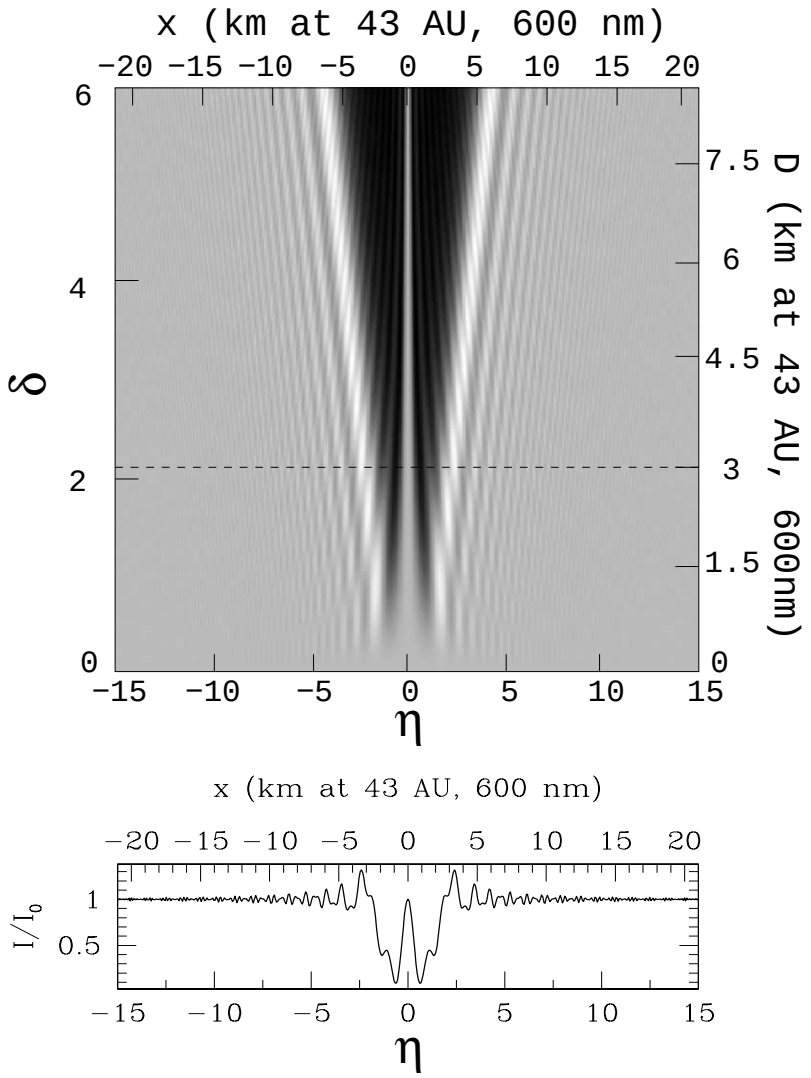

Figure 3.4: Diffraction table (*top*), the y-axis is the diameter (δ) of the occulter in Fresnel units, and the x-axis (η) is the distance from the center of the occultation in Fresnel units. Physical units are marked on the right and top axes in km, assuming KBOs at 43 AU and $\lambda = 600$ nm. The gray scale represents the intensity of the flux. At the bottom an occultation for a $D = 3$ km KBO, or $\delta = 2.16$, as extracted from the table. The location of the light-curve on the table is indicated by a dashed line

and 700 nm (Lehner et al., 2009b). In order to characterize the occultations properly as they would be seen by the TAOS telescopes we weight the stellar spectrum $s(\lambda)$ by the TAOS transmission $f(\lambda)$ (filter bandpass and camera quantum efficiency as a function of wavelength) and then we calculate the diffraction intensity point by point:

$$I_{D,\Delta}(x) = \int_{-\infty}^{\infty} s(\lambda) f(\lambda) I_{D,\Delta}(x, \lambda) d\lambda, \tag{3.1}$$

as described in Nihei et al. (2007). We found that the differences in the spectra among our target stars has a negligible impact on the shape of the occultation pattern as observed by our system. We therefore simulate all of our occultations assuming an F0V spectral type. A lightcurve generated with our simulator for a 3 km KBO at 43 AU occulting an F0V *point source* is shown in Figure 3.5, top.

We now have a diffraction lightcurve for our KBO occulting a point source. Most of our targets, however, have a finite size projected on the plane of the occulter in the sky. We have to take such finite source effects into account, since integrating the occultation over the disk of the star will, at times significantly, smooth the occultation features, while broadening the occultation pattern (and thus the event cross section). The determination of the angular size for our targets is discussed in Section 3.3.4.

Keeping the stellar type fixed, the angular size is modulated by changing the apparent magnitude of the star and we can use the point source lightcurve to integrate the occultation signature over the star disk. For every star and KBO pair for which we generated a point source lightcurve we generate finite source lightcurves for stars in the magnitude range $8 \leq V \leq 14$, with steps of 0.1 mag. A magnitude $V = 11$ finite source lightcurve generated from the point source in the top panel of Figure 3.5, is shown in the second panel, left. Note the smoothing of the diffraction

features.

We then proceed to implant occultation events in our data, which are then reprocessed in the same way we did to search for true events. To generate an event, we first determine the star parameters by identifying the star in the USNO-B catalog (Monet et al., 2003). The elongation angle of the observation determines the relative velocity of the KBO, together with the KBO distance (see Equation 1.8)

We choose the parameters for the occultation: we select a diameter according to a distribution that will allow us to have sufficient number of recoveries at all sizes, so as to be able to sample our efficiency properly (this will be discussed in Section 3.3.5), and we draw a random impact parameter and occultation epoch in the lightcurve. We generate the occultation lightcurve and implant its signal into our star lightcurve:

- We determine the angular size of the target star (see Section 3.3.4), match it to a previously generated finite source lightcurve and load the finite source lightcurve.

- We modify the lightcurve to account for a finite impact parameter b: for this we use the finite source lightcurve at impact parameter $b = 0$ as an input, calculating the intensity of the occultation signal at the new distance of each point by interpolating points of the finite source lightcurve. A lightcurve for an F0V, V=11 star and a 3 km KBO occulting at an impact parameter $b = 2$ km is plotted on the right hand side of the second panel of Figure 3.5.

- We then calculate the relative velocity of the KBO as a function of distance and angle from opposition. Knowing this we can confer time information to our occultation features, which were thus far expressed as a function of the distance to the point of minimum approach, and set the time-line of the event.

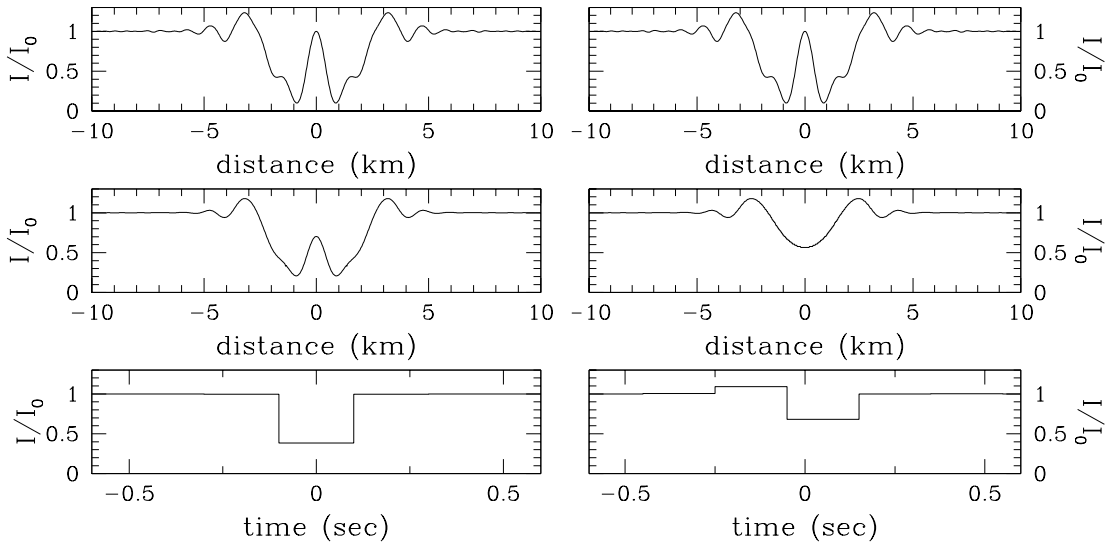

Figure 3.5: Steps of the generation of a simulated occultation event. Top, the left and right panels both show the same point source lightcurve for a 3 km KBO at 43 AU occulting an F0V star. Second row: finite source lightcurves for the same occultation parameters for a V = 11 star, corresponding to an angular size of 0.015 mas, for a zero impact parameter (left), and at an impact parameter of 2 km (right). Row three: the lightcurves in row two are integrated over intervals of 105 ms for the occultation above at opposition (left) and at 50° from opposition (right). The lightcurves are sampled at 5 Hz, with no time offset (left) and with a time offset of 50 ms (right).

- Finally we smooth the lightcurve to account for finite exposure intervals, and we sample the *finite exposure* lightcurve at the appropriate sampling rate. In this step we can account for dead-time in the sampling interval, which for TAOS is 47.5% at 5 Hz. We also allow an offset in time between the center of the finite sampled lightcurve and the integration bin. In the bottom row of Figure 3.5 the lightcurves for the event in row two are integrated over 105 ms second intervals and sampled at 5 Hz, the typical sampling rate of TAOS, for an event at opposition and with no time offset (left) and an event at 50° from opposition with an offset of 50 ms between the center of the sampling interval and the center of the occultation (right).

We now have a proper occultation signature, which can be implanted in

our light-curves.

3.3.4 Determination of the stellar angular size

The angular size of the target star is an important parameter in the generation of an occultation pattern. Our fields contain a variety of stellar types and a large range of angular sizes (Figure 3.6a).

Angular sizes have been related to the position of a star in the color-color or color-magnitude diagrams (e.g., van Belle 1999, Nordgren et al. 2002). We follow the work of Nordgren et al. (2002) and calculate the angular size of our star targets using the 2MASS J and K color (Cutri et al., 2003) to invert the set of equations:

$$F_K = (3.942 \pm 0.006) - (0.095 \pm 0.007)(J - K) \quad (3.2)$$

$$F_K = 4.2207 - 0.1K - 0.5 \log \theta \quad (3.3)$$

where F_K is the surface brightness of a star in K-band, which is related to its $J-K$ color, as well as to its unreddened apparent K magnitude and angular size θ. The relationship between the surface brightness and the color of a star (Equation 3.2) is calibrated using angular sizes measured directly by long baseline interferometry (Nordgren et al., 2002).

Not all of our target stars, however, are identified 2MASS objects, while in the photometry phase we have identified all of our targets with USNO-B objects. We therefore devised a method that relies on USNO-B R and B magnitude to calculate the angular sizes of our targets.

We first derive the angular size of a subset of targets identified with 2MASS objects using the above equations, and scale it to obtain the angular size the targets would have if their apparent magnitude were $R = 12$. We then considered the

USNO-B $B-R$ color for all of these targets and calculated a regression on these points. This generates a formula that allows us to go from the USNO-B color of any of our targets to 2MASS colors and thus predict angular sizes according to Equations 3.2 & 3.3, for an apparent magnitude $R = 12$. To calculate the true angular size we rescale from $R = 12$ to $R_{\rm USNO}$[4]. The angular sizes of a subset of TAOS targets, rescaled to $R = 12$, is plotted as derived from Equation 3.2 & 3.3 versus the USNO-B $B-R$ color (Figure 3.6b). Our regression on the data is plotted as well (solid line).

The scatter in the determination of the angular size via the method described above is large, as can be seen in Figure 3.6b. This is due to scatter in the USNO-B color (≈ 0.3 mag, Monet et al. 2003), to the (much smaller) scatter in the J and K magnitudes and to the scatter in the empirical determination of the relationship between θ and $J-K$ in Equation 3.2 & 3.3. We have not used any interstellar reddening corrections, and the angular size estimation of an unknown reddened star from the near-IR relationship would be relatively less affected compared to that in visual bands. Reddening is typically small for our targets though, since we are only considering objects brighter than $R \sim 13.5$.

The distribution of angular sizes is well reproduced. Figure 3.6a shows the distribution of angular sizes for a typical TAOS field, calculated via Equations 3.2 & 3.3, and Figure 3.6c shows the distribution of angular sizes in our efficiency simulation obtained via the USNO-B color. The distributions do overlap. About 2% of our simulated angular sizes fall in the region $\theta > 0.15$ mas and $R_{\rm TAOS} > 11$, where there are no observed objects. These objects have poor USNO-B color determination. Figure 3.6d shows the region of the $\theta - R_{\rm TAOS}$ space where simulated

[4]We do not use our instrumental magnitude for rescaling for consistency with what is used in the color determination.

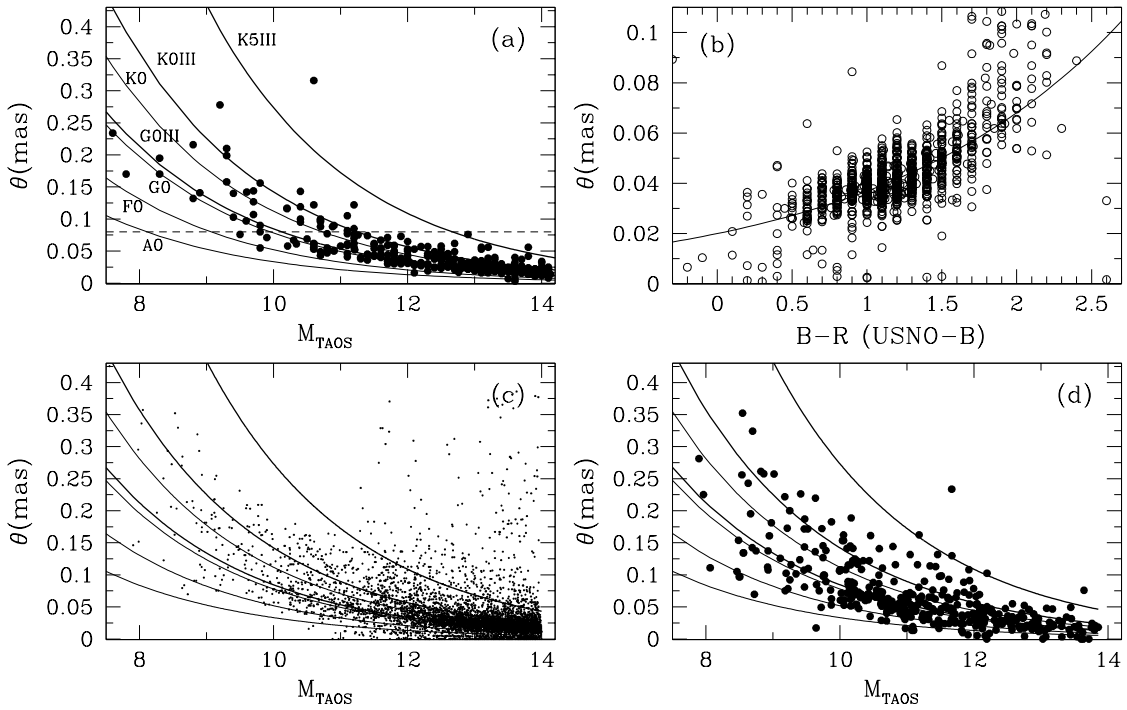

Figure 3.6: Angular size distribution for a typical TAOS field (field 120, RA: 13°.7, Dec: −10°.7) derived from the 2MASS $K - J$ colors (a). The curves show the theoretical behavior of the angular size for A0, F0, G0, K0 dwarf stars (thin lines) and G0, K0, K5 giants (thick lines). The size of the Fresnel scale at 43 AU is shown at 0.08 mas (dashed line). Best fit to the angular size distribution (b): x-axis is the USNO-B $B - R$ color and y is the angular size derived using Equations 3.2 & 3.3, converting all stars to apparent magnitude $R = 12$. Implanted angular sizes, derived from USNO-B the $B - R$ color for our simulation (c) and angular size of the star for which events are recovered (d); a random subset of 1% of our data is plotted in the bottom panel.

events *are recovered*. There are few recoveries in the region $\theta > 0.15$ mas and $R_{\rm TAOS} > 11$, so these stars do not contribute the the expected event rate.

3.3.5 Implantation and efficiency test parameters

We now assess our efficiency at detecting events in the Kuiper Belt. In order to sample properly the space of diameters to which the survey is sensitive we generate synthetic occultations by objects of diameter $D = 0.5$, 0.7, 1.0, 1.3, 2.0, 3.0, 8.0, and 30.0 km. For a 30 km diameter KBO the event falls in the geometric regime,

Table 3.2. Distribution of synthetic events

diameter (km)	implantations	recoveries
30.0	231	75
8.0	385	84
3.0	1078	73
2.0	2003	89
1.3	4393	73
1.0	13255	66
0.7	36222	40
0.5	447764	9

diffraction effects are therefore no longer significant and our efficiency stabilizes. Because our sensitivity decreases with decreasing diameter we implant progressively more objects at smaller diameters. The number of implantations at each size is designed to allow us to obtain a good sampling at all sizes. In Table 3.2 we report the number of objects implanted for each size in one of our efficiency runs, and the number of recoveries[5]. For objects within the Kuiper belt (about 30 to 60 AU), the differences induced by different distances are negligible in the occultation features as observed by TAOS. We therefore set the distance to $\Delta = 43$ AU.

Every occultation event is implanted at a random epoch in the lightcurve set. We also draw a random impact parameter between 0 and $H/2$, where we set H, a measure of the cross section of the event, to the size of the Airy ring and the projected size of the star, as descibed in Section 1.3.1 (Equation 1.3.1).

In order to implant these occultations we modulate the lightcurve by subtracting (adding) the amount of flux suppressed (augmented) by the occultation at each data-point: that is, the implanted lightcurve $f_{\rm occ}$ is generated as $f_{\rm occ}(t) = f(t) - (1 - d(t))\bar{f}$, where $\bar{f}$ is the local mean of the flux, and $d(t)$ is

[5]Four runs are conducted to reduce the error in the determination of our efficiency.

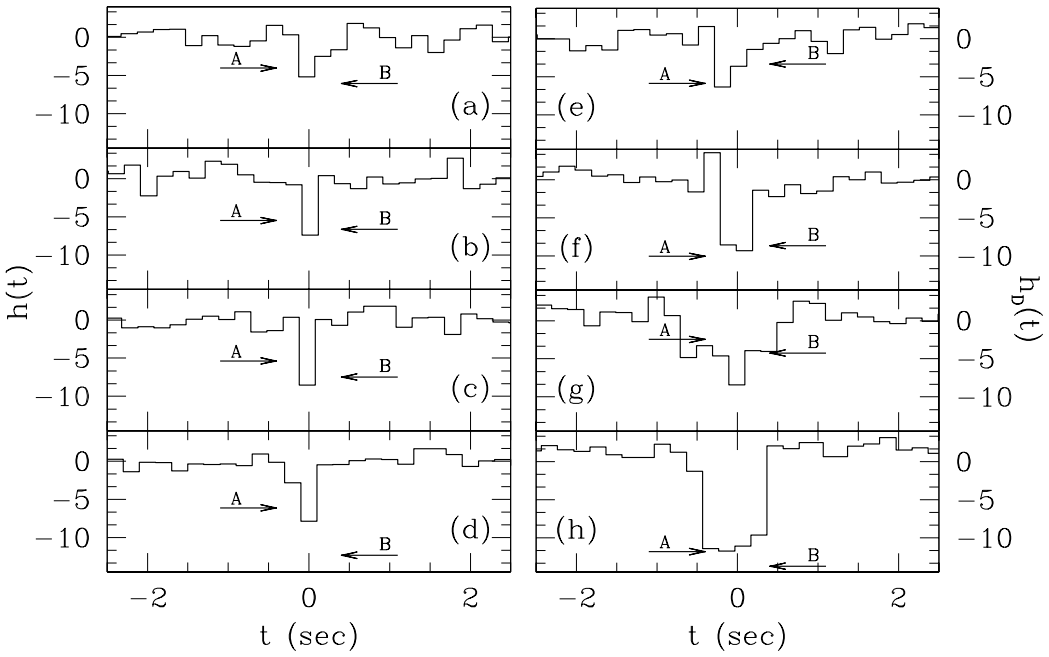

Figure 3.7: Implanted occultations recovered by our pipeline. On the left the lightcurves refer to star targets in a field near opposition (Field 158, RA: $18^{\rm h}$ $53^{\rm m}$ $44^{\rm s}$, Dec: -17° $23'$ $00''$) and on the right to a field at large angle from opposition (Field 22, RA: $4^{\rm h}$ $52^{\rm m}$ $43^{\rm s}$, Dec: -20° $51'$ $00''$).Each data-point $h(t)$ represents the deviation of that time-stamp from the local mean of the lightcurve in units of standard deviation. The lightcurve for telescope D is plotted in each panel, while the relevant measurement, $h(0)$, for telescope A and B are indicated by arrows with the height of the arrow representing the measurement at the center of the occultation $t = 0$. Each event is described in Table 3.3

the simulated event lightcurve with baseline $d(t) \to 1$ away from the event. This approach slightly overestimates the noise due to Poisson statistics where the flux is suppressed, giving us a conservative estimate of our efficiency. We implant exactly one occultation in each lightcurve in our dataset.

3.3.6 Analysis of the efficiency parameters

We now process our implanted lightcurves as we previously did to search for events, namely we filter, rank the lightcurves, and evaluate the significance ξ of each point in each lightcurve. We then remove the false positives as described in

Table 3.3. Parameter of implanted events in Figure 3.7

	D (km)	b (km)	$v_{\rm rel}$ (km/s)	SNR	$\theta_\star$ (mas)
(a)	0.7	0.50	25.4	39.8	0.03
(b)	1.0	0.50	14.9	29.4	0.03
(c)	3.0	1.19	25.4	12.8	0.03
(d)	8.0	2.7	25.4	9.4	0.006
(e)	0.7	0.22	8.2	10.2	0.03
(f)	1.0	0.94	7.7	10.8	0.03
(g)	3.0	1.18	3.1	12.9	0.006
(h)	8.0	2.93	8.1	15.7	0.04

Section 3.3.2. Our efficiency decreases rapidly with the KBO diameter: from nearly 33% at $D = 30$ km to 2×10^{-5} at $D = 0.5$ km. Note that at $D = 30$ km we ignore diffraction effects and the occultations are modelled to suppress the flux completely for several consecutive points, depending on the relative velocity, but our efficiency is still significantly less than 100%. Some of our lightcurves are too noisy to allow detections.

A set of synthetic events recovered by our pipeline in shown in Figure 3.7, and the parameters of each plotted event are given in Table 3.3. Various parameters affect our recovery efficiency. Our efficiency for the recovery of $D = 3.0$ km occulting KBOs is plotted in Figure 3.8 as a function of $M_{\rm TAOS}$, SNR, relative velocity $v_{\rm rel}$ and crowdedness of the field.

The efficiency as a function of SNR is plotted in Figure 3.8a –a few targets at SNR > 100 are left out of the plot. The efficiency decreases with magnitude (Figure 3.8c) by about a factor of five between magnitude 9 and 13. The dominant effect here is the decrease in SNR, though a competing effect occurs since lower magnitudes are associated with larger angular sizes, and our efficiency decreases with increasing angular size (Figure 3.6). Furthermore there are many more dim

than bright stars in the sky: Figure 3.8f shows the efficiency as a function of $M_{\rm TAOS}$ multiplied by the number of TAOS targets at that magnitude. The highest number of detections happen for stars with $M_{\rm TAOS} \sim 12.5$.

The behavior of our efficiency as a function of crowdedness, where the crowdedness is defined as the number of targets in that TAOS field brighter than $R_{\rm USNO} = 13.5$, is plotted in Figure 3.8b. The largest number of detections per field is achieved for fields with more than 1500 $R_{\rm USNO} < 13.5$ target stars.

Our efficiency as a function of the relative velocity of the KBO is plotted in Figure 3.8d. Observing at a pointing where the relative velocity of the KBOs is higher boosts the event rate of the survey. Our efficiency is however larger for smaller transiting velocities, particularly for small KBOs for which the time-line of the event is shorter than one of our data-points at opposition. Ultimately, the effective sky coverage of our survey depends linearly on both the efficiency and the velocity (see section 4.2). The efficiency multiplied by the relative velocity $v_{\rm rel}$ is plotted against $v_{\rm rel}$ in Figure 3.8f. Pointing near opposition increases the effective coverage of our survey, and thus it increases the event rate, for 3 km KBOs. The survey strategy can be optimized at different sizes taking into account the size dependent efficiency $\times$ $v_{\rm rel}$ as well as the expected KBO size distribution.

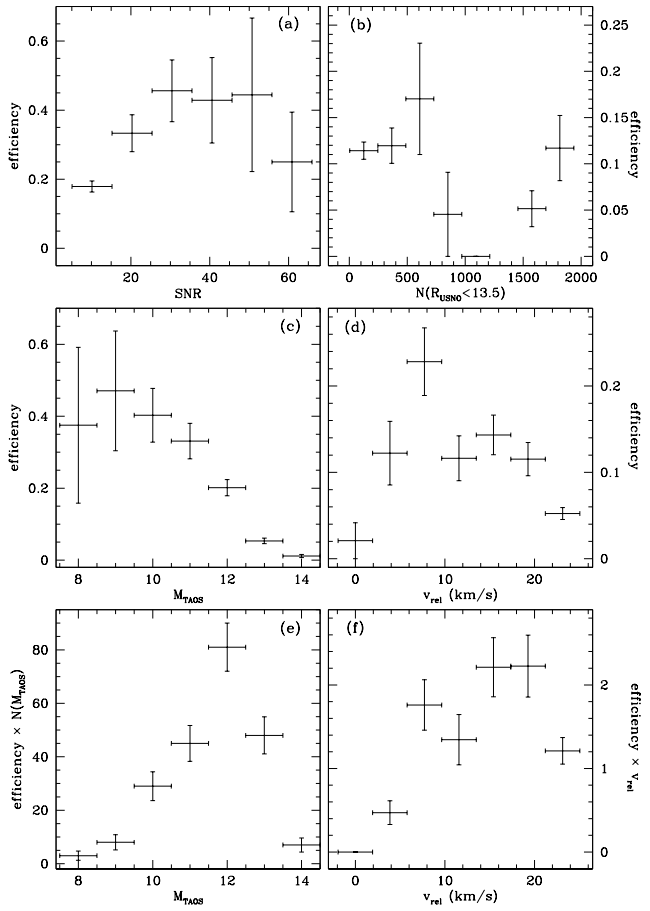

Figure 3.8: Recovery efficiency for 3 km KBOs. Panel (a): efficiency as function of SNR. Efficiency versus crowdedness of the field (b), defined as the number of targets brighter than $R_{\rm USNO} = 13.5$. Panel (c): efficiency versus magnitude $M_{\rm TAOS}$. In panel (e) the efficiency as a function of magnitude is weighted by the number of targets at that magnitude. Panel (d): efficiency versus relative velocity of the KBO targets. In panel (f) the efficiency versus relative velocity is weighted by the relative velocity. All error bars are calculated in a Poissonian fashion from the square root of the number of recoveries.

Chapter 4

Constraints on models of the Solar System formation and evolution from the TAOS data

We compute the number of events expected for the Kuiper belt formation and evolution models by Pan & Sari (2005), Kenyon & Bromley (2004), and Benavidez & Campo Bagatin (2009). We present a comparison with upper limits we derive from 3.75 years of TAOS data which constrains the parameter space of these models. This is the first direct comparison of models of the KBO size distribution with data from an occultation survey. Our results suggest that the KBO population is indeed strengthless and planetary migration played a role in the shaping of the size distribution[1].

[1]This work, together with Chapter 3, was accepted for publication by the Astronomical Journal under the title *The TAOS Project: Upper Bounds on the Population of Small KBOs and Tests of Models of Formation and Evolution of the Outer Solar System*, and it is the product of a collaboration with the TAOS team and with M. J. Holman (Harvard-Smithsonian Center for Astrophysics)

4.1 Introduction

In this chapter I describe the constraints on the KBO population derived from our analysis of 3.75 years of TAOS data, discussed in Chapter 3. In Section 4.2 I derive the effective coverage of our survey and model–independent limits to the number of objects in the Kuiper belt, and compare these results with those of similar surveys. In Section 4.3 I compare our upper limits to the estimates on the number of KBOs set by dynamical simulations for JFC progenitor populations. In Section 4.4 I briefly describe models for the formation and evolution of the Kuiper belts and I then derive and discuss constraints to these models.

4.2 Effective coverage and upper limits

We calculate the effective sky coverage of our survey, $\Omega_{\rm e}$, as:

$$\Omega_{\rm e}(D) = \frac{1}{w(D)} \sum_{*} \frac{H(D,\theta_*)}{\Delta} \, \frac{v_{\rm rel}}{\Delta} \, E_*, \tag{4.1}$$

where E_* is the exposure of the star target (the duration of the lightcurve set), $w(D)$ the weight factor for that diameter, i.e. the fraction of lightcurves implanted with occultations by KBOs of diameter D, and the sum is carried out only over the lightcurves where events are recovered. The effective coverage of our survey, which takes into account our efficiency, is plotted in Figure 4.1, for both the dataset published in Z08 (empty squares) and for the current work (filled squares).

We can use $\Omega_{\rm e}$ to calculate model-independent upper limits: at each size for which our efficiency calculation was conducted we calculate the number density of KBOs from the TAOS dataset as a *single-point* upper limit. These limits are shown as filled dots in Figure 4.2. Each point represents the maximum surface

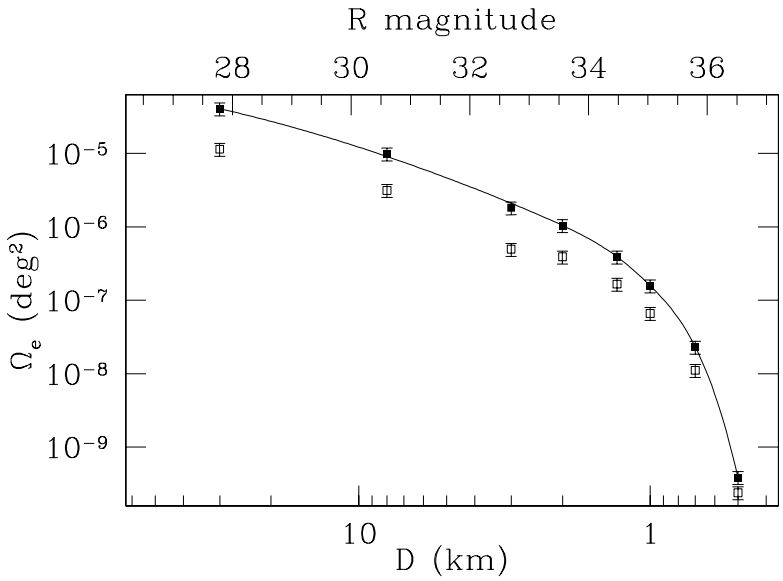

Figure 4.1: Effective solid angle for the first 2 years of TAOS data (Z08, empty squares) and for the current 3.75 year dataset (solid line and filled squares).

density of KBOs $\gtrsim D$. Note that these limits are *not* statistically independent of each other. Figure 4.2 also shows the similarly calculated upper limits of Bickerton et al. (2008) and Bianco et al. (2009a). This allows a direct comparison of the results from our survey with these earlier results and the improvement is obvious: nearly an order of magnitude at 700 m and over an order of magnitude at 1 km from the most recent results, those of Bianco et al. (2009a).

4.3 The Jupiter Family Comets progenitor population

The Jupiter Family Comets (JFCs) are believed to originate in the Outer Solar System. In this scenario the giant planets generate gravitational perturbations that affect the orbits of the Outer Solar System bodies, injecting them into the planetary region, where they are captured by Jupiter. The orbital inclination of the

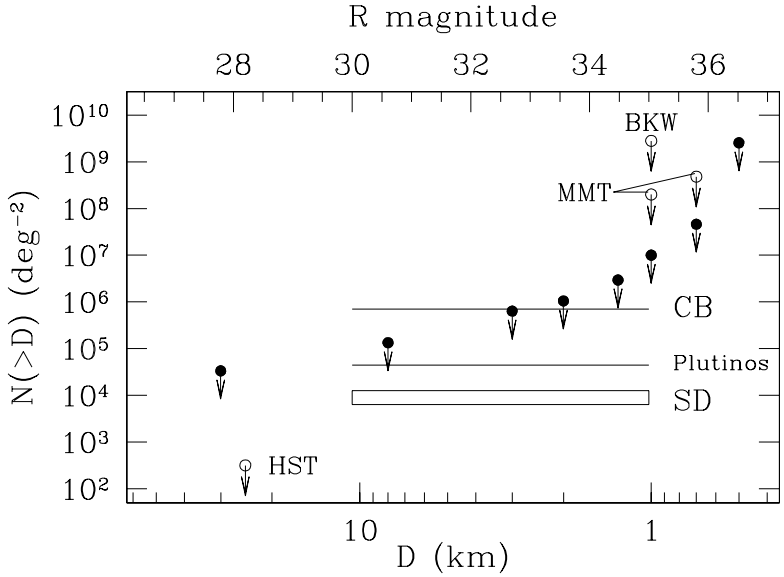

Figure 4.2: Upper limits from the TAOS survey (solid dots). Each point represents the upper limit to the number of KBO of that size or larger given the TAOS effective coverage. Similarly derived upper limits from Bickerton et al. (2008) at 1 km (BKW, empty circles) and Bianco et al. (2009a) at 1 km and 0.7 km (MMT, empty circles) are also plotted. The upper limit from Bernstein et al. (2004) is also plotted (HST). The estimates of the number of objects in the Classical Belt (CB), of Plutinos and scattered disk objects (SD) are plotted, as derived by Levison & Duncan (1997), Morbidelli (1997) and Volk & Malhotra (2008) respectively, assuming each family is the unique precursor of JFCs.

JFCs suggests that their precursor population has a disk-like distribution, favoring thus the Kuiper belt over the Oort Cloud as a reservoir (Volk & Malhotra, 2008, and references therein). The Classical Belt (CB), the Plutinos and the scattered disk (SD) have been considered as precursors in various studies. The dynamical characteristics of each population determines the efficiency of the injection process and the number of objects in each progenitor family can thus be derived on the basis of the density of JFCs, which is observationally constrained (see Tancredi et al. 2006, and references therein). Furthermore the size distribution of JFCs should reflect the size distribution of the progenitor population. Bernstein et al. (2004) and Bianco et al. (2009a) have pointed out that a better determination of the size distribution of the Kuiper Belt would help understand the origin of the JFCs.

We assume the JFC precursors are in the size range $1 - 10$ km as this is observed to be the typical size of JFCs (Lowry et al., 2008). We considered the estimates on the KBO populations (CB and Plutinos) and SD derived from dynamical simulations under the assumption that each population is the unique progenitor of the JFCs, and we compared them to the upper limits derived from our survey (Figure 4.2). We use the estimate of Levison & Duncan (1997) for a population of cometary precursors entirely in the CB, and that of Morbidelli (1997) for Plutino progenitors. These are converted into a surface density by assuming for each population a projected sky area of 10^4 deg^2, as was done by Bernstein et al. (2004). We consider the results of Volk & Malhotra (2008) for a progenitor population in the SD . We calculate the minimum surface density of SD objects expected in the region of sky typically observed by the TAOS survey. For this we use information on the fraction of time the objects spend between 30 and 50 AU and within 3° of the ecliptic plane as provided by Volk & Malhotra (2008). These estimates on the number of objects are shown in Figure 4.2 as horizontal lines.

Our results rule out the CB as unique precursor *if* all progenitors have $D \geq 3$ km. Occultation surveys are the only surveys that at present can probe this region of the size spectrum, and our preliminary result shows that future occultation surveys will be able to derive useful constraints on the origin of the JFCs.

4.4 Outer Solar System collisional models

The collisional and dynamical evolution of the Solar System shaped the size distribution of the Kuiper belt. In the *coagulation scenario* the Kuiper belt was first shaped out of collisions among the primordial planetesimals (Kenyon & Luu, 1999a). The belt was originally populated by very small dust grains, with small orbital eccentricities ($e \leq 0.01$) such as those we observe in circumstellar disks around other stars (Moro-Martin et al., 2007). Initially these small objects merge in collisions and slowly grow: 1 km KBOs in the Kuiper belt are thus formed. As their gravitational cross section grows larger than their geometric cross-section, *gravitational focusing* speeds up the growth rate of the largest bodies. This phase is referred to as runaway growth, and objects as large as hundreds of kilometers can form. One such population, shaped primarily through agglomeration processes is predicted by theory to have a power law distribution in diameter $dN/dD \propto D^{-q_{\rm L}}$ with power $q_{\rm L} \approx 4.5$ (Kenyon & Luu, 1999b). Direct observations of large KBOs confirm the power law behavior in this regime, the *gravitationally–dominated* region of the size spectrum, with a best fit of $q_{\rm L} = 4.25$ (Fraser et al. 2008, Fuentes & Holman 2008). The size distribution of these large objects, for which gravity dominates the internal strength, is remarkably insensitive to parameters such as Neptune stirring or the internal tensile strength of the KBOs.

Meanwhile, very large objects in the planetary region of the Solar Sys-

tem are also forming into planets, that are believed to undergo significant migrations (Tsiganis et al., 2005, and references therein). The orbits of the planetesimals are then stirred up via gravitational interaction to velocities such that further impacts will result in the disruption of the smaller objects: this is the *catastrophic collisions* phase (Davis & Farinella, 1997; Kenyon & Luu, 1999a; Morbidelli et al., 2008); the time scale to reach this phase is estimated to be between 10 Myr and 1 Gyr (Kenyon & Bromley, 2001). A second steady state occurs for very small objects (probably tens of meters and smaller) where the collisionally evolved population transitions to a *strength-dominated* regime. Here the collisional cascade will generate a size distribution which follows a power law with index $q_{\rm S} = 3.5$ (Dohnanyi, 1969; Kenyon & Luu, 1999a), also in a fashion that is largely independent on the details of the evolution of the protoplanets. Note that the study of collisions between icy bodies is still in its infancy, and future work in this field will permit assessing the behavior of colliding small strength-less or loosely bound particles (Leinhardt, 2008). Similarly, future work on coupling collisional and dynamical evolution codes, recently pioneered by Charnoz & Morbidelli (2007), should provide further insight in the behavior of the size distribution.

We will refer to the region in between these two regimes as the *intermediate* region. The extent of, and the size distribution in, the intermediate region are instead very sensitive to the formation and evolution parameters, and observational information on this region can be compared to evolution models. In this section, we present four models of the KBO size distribution dN/dD, three models from literature and a simple parametric model. On the basis of these models we calculate the number of events expected to be detected by the TAOS survey, which is given by:

$$N_{\rm exp} = \int \frac{dN}{dD}\, \Omega_{\rm e}\, dD.$$

Since no events were found in our survey, any model which predicts $N_{\rm exp} \geq 3$ is t ruled out by TAOS at the 95% confidence level.

4.4.1 Pan & Sari (2005)

Pan & Sari (2005, hereinafter PS05) derived a fully analytical model for the size distribution of KBOs by assuming the population is in a steady state and the mass is constant through the collisional processes. They assume for most of their model calculation that the internal strength of the objects is negligible (gravity dominated objects). This assumption is motivated by studies of comets and asteroids (PS05 and references therein). PS05 discuss the transition to the fully strength-dominated regime, where they model the size distribution as a power law with power index $q_{\rm S} = 3.5$ according to Asphaug & Benz (1996). This region however starts at $D \leq 300$ m and is entirely below the sensitivity of TAOS. Under these assumptions PS05 derive a double power law size distribution for objects $D \geq 300$ m:

$$\begin{aligned} dN/dD &\propto d^{-q_{\rm L}} \quad for \quad D > D_{\rm b}, \\ dN/dD &\propto d^{-q_{\rm I}} \quad for \quad D < D_{\rm b}. \end{aligned} \tag{4.2}$$

This model is shown in Figure 4.3, left. The slope q has value $q_{\rm L} = 5$ for large objects and $q_{\rm I} = 3$ for objects in the intermediate region. They are thus able to calculate self-consistently, as a function of time, the location of the break the power $D_{\rm b}$, which represents the size of the largest KBOs that experienced catastrophic collisions. The location of the break moves toward larger objects as the size distribution evolves; the authors predict the break near $D_{\rm b} = 40$ km. Note that in the intermediate region between $D_{\rm b}$ and the second break, which is the region that TAOS can probe, a realistic size distribution is expected to have an oscillatory behavior while preserving

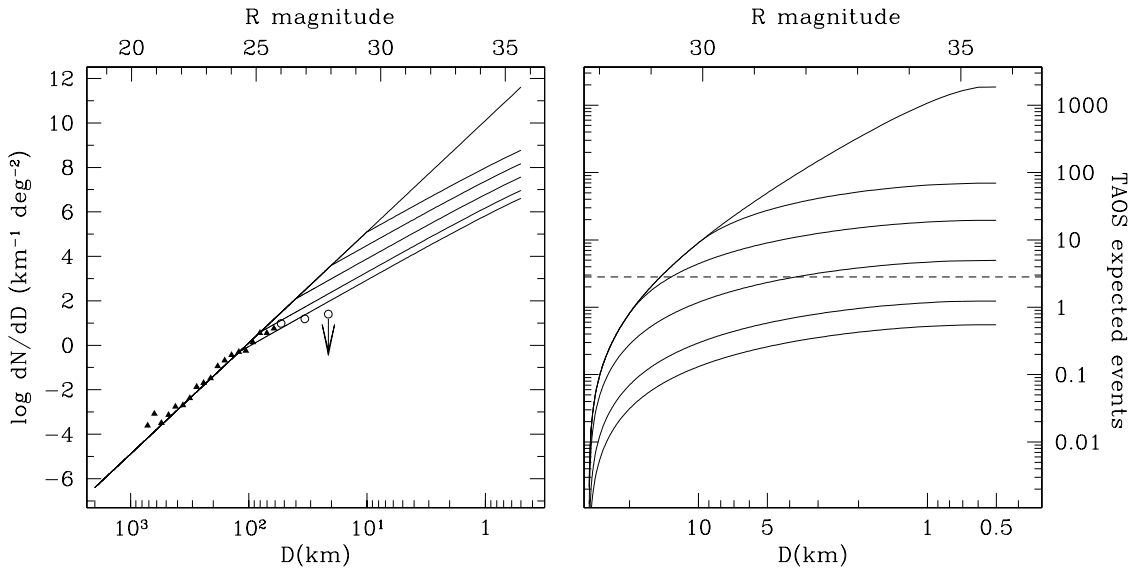

Figure 4.3: PS05 model and expected event rate for TAOS. *Left.* Triangles are the data from Fraser & Kavelaars (2008). Empty circles are the data from Bernstein et al. (2004). We use these direct observation data to set the location of the large end size distribution. The model is parametrized with two slopes, $q_{\rm L} = 5$ and $q_{\rm I} = 3$. The positions of the break are at $D_{\rm b}$ =100, 80, 40, 20, and 10 km. *Right.* Expected yield of events in 3.75 years of TAOS data. The horizontal dashed line represents the highest number of events allowed by no-detections (3 events at the 95% confidence level). Any model above this limit is ruled out by our survey.

an average slope of $q_{\rm I} = -3$ (PS05).

We parametrized the PS05 model with two slopes and a hard junction point. Distributions with break points $D_{\rm b}$ = 100, 80, 40, 20, and 10 km are shown in Figure 4.3. The left panel shows our parametrization of the model, and the corresponding predicted number of events for the TAOS data analyzed in this paper is plotted in the right panel[2].

On the basis of our no-detections result, break diameters of $D_{\rm b} < 51.3$ km are excluded at 95% confidence level. This is consistent with the data from direct observations and with the authors' interpretation of the model: in absence of stirring

[2]Note that the uppermost curve in the right panel of Figure 4.3, which corresponds to a simple extension of the large-size power law distribution, represents the naive expectation before Bernstein et al. (2004) appeared. This was the initial design target of the TAOS project. *TAOS has met and exceeded its original design goals!*

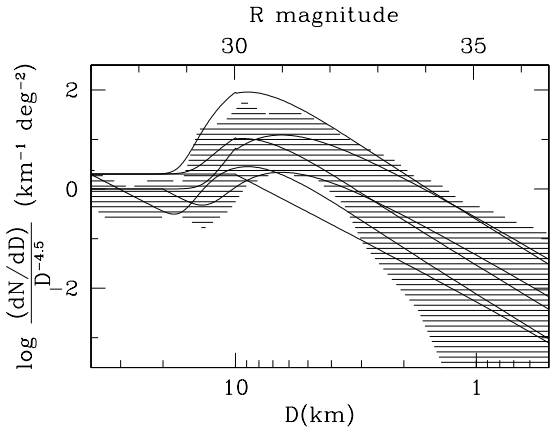

Figure 4.4: Our modeling of the KB04 results. The range of results of the simulations of KB04 is represented by the shaded region. A few of our models are plotted as solid lines. All models are normalized by the slope of the large KBO size distribution $D^-{-}4.5$.

by Neptune, the location of the break suggests that the KBO population is comprised of objects with little internal strength.

4.4.2 Kenyon & Bromley (2004)

Bernstein et al. (2004): here collisions destroy weak KBOs and models with Neptune stirring, or weakly bound KBOs produce a more significant dip. This feature is followed by an excess with respect to the nominal power law for 2-15 km KBOs which varies in amplitude between a factor of a few and a factor of a few tens, depending on the internal strength and presence of Neptune (see Figures 4.4 and Figures 4.5 & 4.6, left column). The size distribution remains sensitive to the details of the models down to about $D = 50$ m, where once again a power law behavior begins, with power $3 < q < 5$ in the strength-dominated regime.

We parametrize the KB04 suite of models to allow us to compare them directly to our survey. Specifically, we model the large size distribution as a power law with $q_{\rm L} = 4.5$ and the intermediate region with $q_{\rm I} = 2$. We also model the

excess (*bump*) around $D = 5$ km with a Gaussian, so that:

$$\frac{dN_{\rm ex}}{dD} = \frac{dN}{dD}\left(1 + I_{\rm ex}\exp -\frac{(D-\mu_{\rm ex})^2}{2.0\ \sigma_e}\right). \quad (4.3)$$

We fix the width of the Gaussian excess to $\sigma_e = 3.5$ km, we set the location to $\mu_{\rm ex} = 5.5$ km or $\mu_{\rm ex} = 1.6$ km. The intensity of the excess is determined by $I_{\rm ex}$; we consider models with an excess of $I_{\rm ex} = 0,\ 10$ and 100. Note that as the break diameter moves towards large sizes the models naturally simulate the small dip near 20 km. Our results are not sensitive to the presence of this depletion.

In Figure 4.4, the range of results of the KB04 simulations is shown as a shaded region and a few parameter choices for our model are shown as solid lines. The size distribution is shown scaled by the slope of the large size region ($D^{-4.5}$). Focusing on the region near the transition between primordial and collisionally evolved population, an excess near 5 km and a depletion near 25 km are both visible and well represented in our models. The behavior of the simulations at $D > 100$ km is not well fit by our models but this does not affect our event rate calculation, since the expected number of occultation by such large objects is negligibly small. Figure 4.5 shows the models with $\mu_{\rm ex} = 5.5$ km (left) and the corresponding expected number of events for the TAOS dataset (right) in absence of a bump (top) and for bump intensities $I_{\rm ex} = 10$ (center), $I_{\rm ex} = 100$ (bottom). Figure 4.6 shows the models with $\mu_{\rm ex} = 1.6$ km (left) and the corresponding event rates for the TAOS dataset (right) for a bump intensities $I_{\rm ex} = 10$ (top) and 100 (bottom). Both figures show models with break locations $D_{\rm b} = 60$, 40, 20, 10, and with no break.

For a bump centered at $\mu_{\rm ex} = 5.5$ km break points $D_{\rm b} > 75.3$ km are allowed for any combination of parameters. We can constrain the intensity of the excess: any break diameter smaller that 75.3 km is ruled out for models with a

$I_{\rm ex} = 100$, break diameters $D_{\rm b} < 32.6$ km are ruled out for $I_{\rm ex} = 10$ and breaks at $D_{\rm b} < 16.5$ km are ruled out in absence of the excess. When moving the break towards smaller sizes ($\mu_{\rm ex} = 1.6$ km), break locations are ruled out for $D_{\rm b} < 63.3$ km if $I_{\rm ex} = 100$, and $D_{\rm b} < 28.3$ km if $I_{\rm ex} = 10$. Note that the KB04 simulations show that models with weaker KBOs and Neptune stirring favor a location of the bump at smaller sizes.

All together our result strongly favors models that incorporate the effects of Neptune stirring and weaker KBOs, where the bulk strength Q_b is roughly $Q_b < 10^3$ erg g^{-1}.

4.4.3 Benavidez & Campo Bagatin (2009)

Recent simulations by Benavidez & Campo Bagatin (2009, BCB09 hereinafter) divide the Kuiper belt into three dynamical families – the CB, the Plutinos (Resonant Population) and the SD – and follow the collisional evolution of each, while taking into account the physics of the fragmentation of icy and rocky bodies at the typical relative velocities of KBOs. This suite of models ignores the effects of Neptune stirring. The models incorporate four scaling laws for fragmentation: a simple scaling driven by gravitational self-compression, two scaling laws which include both self-compression and the effects of strain-rate, as described by Farinella et al. (1982), with different diameter dependency ($D^{-0.25}$ and $D^{-0.5}$) and one that follows the modeling of Benz & Asphaug (1999) for icy bodies. They then vary the material strength of the objects between 10^5 and 10^7erg cm^{-3}.

They predict a power law size distribution for large objects, with slope $q_{\rm L} \approx 4.0$, and with a first break around 100 km. The size distribution then departs from power law behavior for all parameter choices, with two to four orders of magnitudes fewer KBOs in the ~ 1 km region than the nominal power law would predict. The

size distribution then follows again a power law, with slope $q_S = 3.5$, in the strength-dominated regime. The BCB09 models are shown in Figure 4.7, left. We simplified the size distribution behavior in the intermediate region with a single power law, though typically the behavior is oscillatory.

These models are all allowed by the TAOS data, partly because of the location of the initial break at $D_b = 100$ and the slope of the large end size distribution. The break location is at the large end of what is allowed by direct observations (indeed outside of the Fraser & Kavelaars (2008) allowed range of $D_b \in [50, 95$ km] with assumption of a 6% albedo). The location of this first break does not evolve in the BCB09 simulations from what is set as an initial condition. Similarly the slope at the large end of the size distribution $q_L = 4.0$, which is slightly shallower than the current best fit value from Fraser & Kavelaars (2008) and Fuentes & Holman (2008) is input as an initial condition and the value hardly changes in the simulation. As the parameters relative to the large size end of the distribution are more firmly pinned down by direct observations, future occultation data will place stronger constraints on the details of the shape of the size distribution below the first break and thus the details of the fragmentation mechanisms, providing information on the internal structure of the KBOs.

4.4.4 Generic 3–regime model: constraints on the intermediate region of the size spectrum

While direct surveys can set constraints on the slope of the size distribution for large KBOs (q_L) and location of the first break in the power law (D_{b1}), our survey provides the only current dataset able to specifically probe what happens after this first break. A simple 3–regime model allows us to parametrize separately

the primordial region, the intermediate region and the fully collisional, strength-dominated regime. Knowing that both the large (gravitationally-dominated) and the small (strength-dominated) regions of the size spectrum are rather insensitive to the details of the internal structure and evolution of the Kuiper belt, it is the intermediate region that contains the most information about the physical details of the KBOs. We grossly simplify the expected structure in the intermediate regime and describe it with a power law. The parameters of one such models would then be three slopes $q_{\rm L}$, $q_{\rm I}$, and $q_{\rm S}$, and two break locations $D_{\rm b1}$ and $D_{\rm b2}$.

We set the slope of the large end of the size spectrum and the location of the first break to the best fit to the data from direct observations: $q_{\rm L} = 4.25$ and $D_{\rm b1} = 75$ km. We model the intermediate region as a plateau, or with a shallow slope: $q_{\rm I} \in [0, 3]$, and the small size end of the spectrum as a power law with slope 3.5 for the strength-dominated, collisionally evolved population. Figure 4.8 shows our 3-regime model (left) and the limit we can set to the intermediate slope, $q_{\rm I}$, and second break location, $D_{\rm b2}$, phase space (right). Any pair of values $q_{\rm I}$ and $D_{\rm b2}$ that fall above the solid line are excluded. At this time we can not only use this result as a guideline in survey design but also for the comparison of any size distribution model with the present TAOS data, particularly as the data from direct surveys help constrain more firmly the large end size slope and location of the first break.

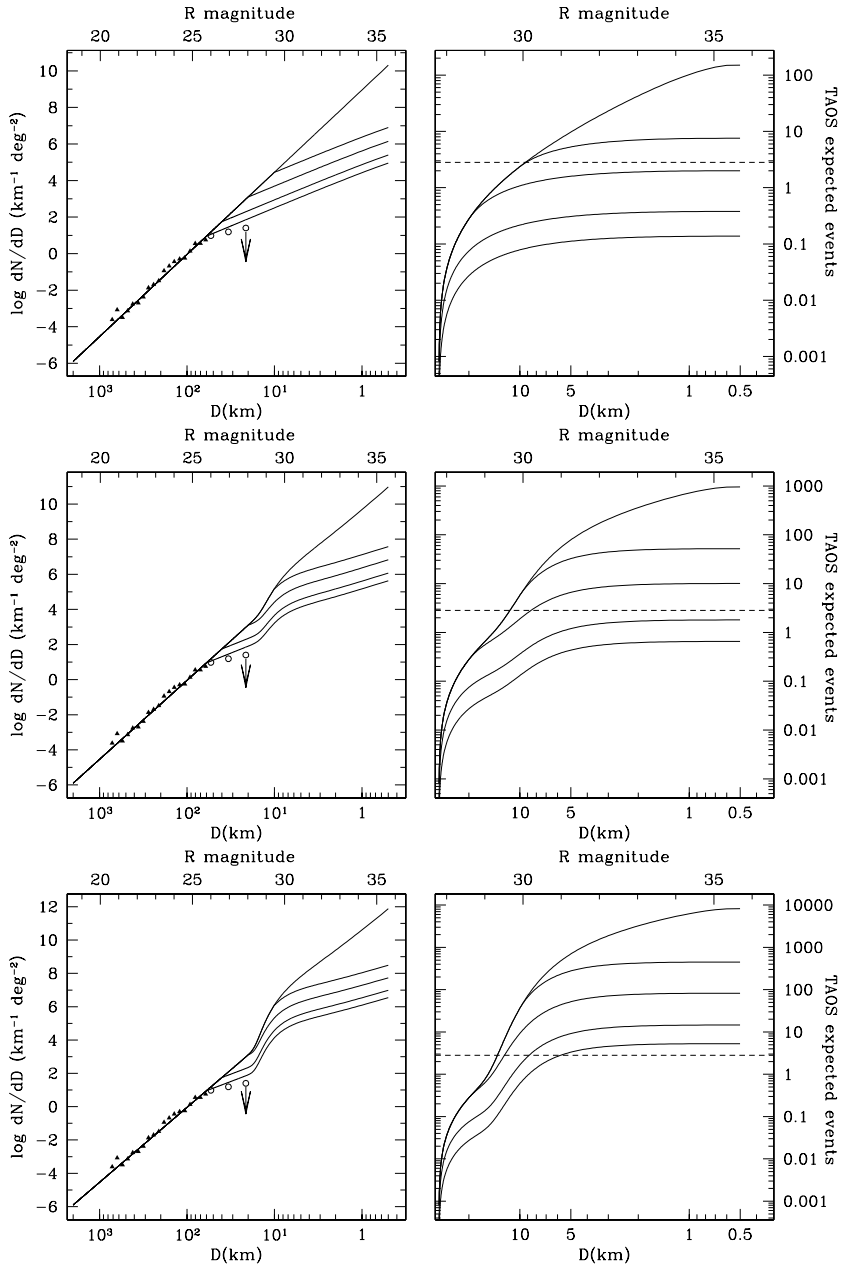

Figure 4.5: KB04 models. The left column shows the differential size distribution, parametrized as two slopes ($q_{\rm L} = 4.5$ and $q_{\rm I} = 2$) and on the right side are the corresponding event rates for the TAOS survey. Symbols are the same as in Figure 4.3. The top row shows the models without bump, the center and bottom panel with a Gaussian bump centered at $\mu_{\rm ex} = 5.5$ km of intensity $I_{\rm ex} = 10$ (top), and $I_{\rm ex} = 100$ (bottom), with $D_{\rm b}$ =60, 40, 20 and 10 km, and no break.

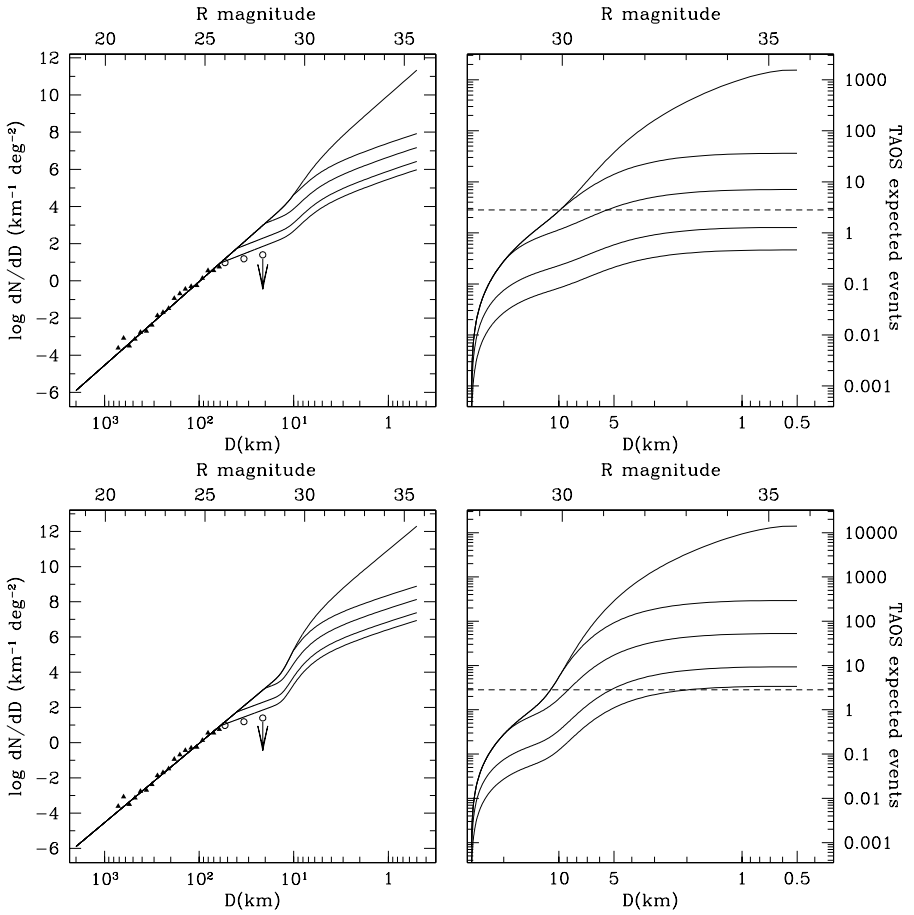

Figure 4.6: Kenyon and Bromley model, as in Figure 4.5 but with Gaussian bump centered at $\mu_{\rm ex} = 1.6$ km, $I_{\rm ex} = 10$, top, and $I_{\rm ex} = 100$, bottom. Right: corresponding number of events in our TAOS survey. Symbols are the same as in Figure 4.3

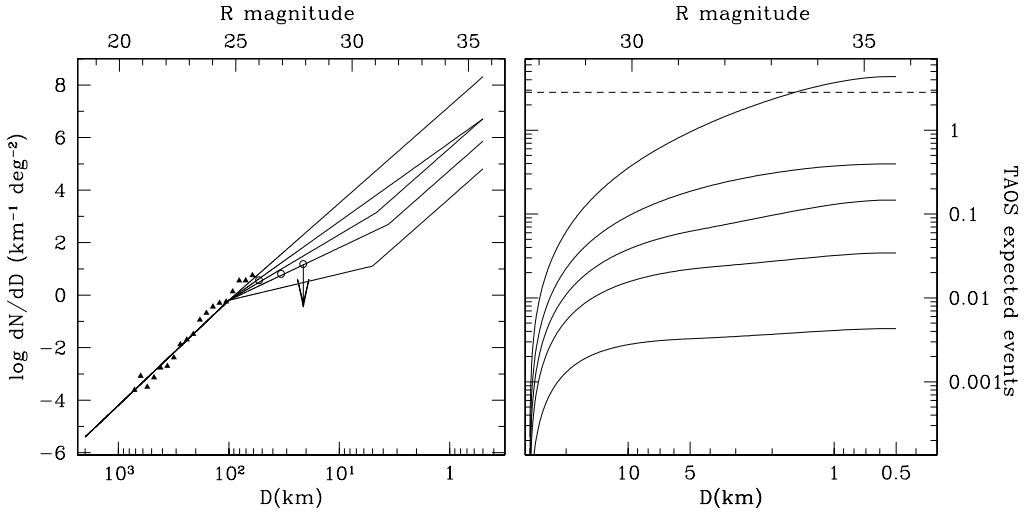

Figure 4.7: Our parametrization of BCB09 models: the models differ in the prescription for fragmentation and all models are parametrized as a series of three slopes. Symbols are the same as in Figure 4.3. The first break points is fixed at 100 km. The slope for the smallest size objects is set to 3.7. The location of he second break and intermediate slope are 5 km and 1.0, 3.6 km and 2.0, 4.6 km and 2.5 and 0.36 km and 3.0. Right: corresponding number of events in our TAOS survey.

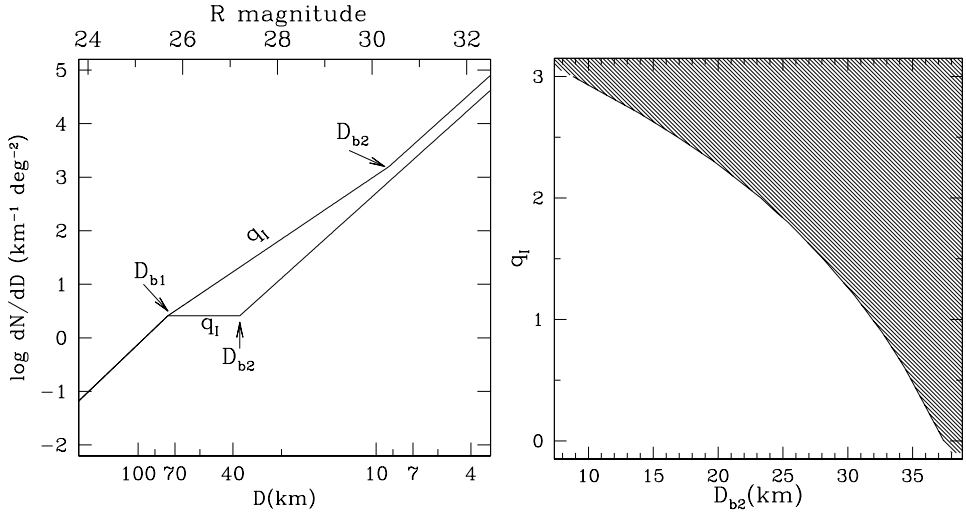

Figure 4.8: Three-slope model described in Section 4.4.4 (left) for the minimum second break location $D_{\rm b2}$ allowed by slopes $q_I = 0$ and 3. Slope–break location phase space for the three-slopes model (right). The region above the line is excluded by our data.

Chapter 5

Exploring the Solar System beyond the Kuiper belt

We explored 5×10^5 star hours of data from the Taiwanese American Occultation Survey (TAOS), the dataset described in Chapter 3, searching for occultations of bright stars by solar system bodies in orbit between 100 and 1000 AU. We found no such event. Our final goal will be to compare our no-detection result with predictions from models of the formation of the Sedna population and of the scattered disk, thus setting upper limits on the number density of Sedna-like and scattered disk objects and constraints on formation evolution scenarios[1].

5.1 Introduction

The outer solar system is populated by icy bodies that formed in the early stages of planetary formation. While direct imaging surveys can probe the classical belt and the resonant population of the Kuiper belt (KB) down to objects as small as tens of kilometers, the outer solar system extends well beyond 50 AU, in various

[1]The work presented in this chapter is the product of a collaboration with the TAOS team.

dynamical families of objects: the scattered disk (SD), extended scatter disk (ESD) and inner and outer Oort cloud. In these regions objects as large as tens, hundreds or even thousands of kilometers in diameter would elude direct detection.

With the term SD we generally refer to the region of orbital space with perihelion $q > 30$ AU and semi-major axis $a > 50$ AU (see for example Gomes et al. 2005b). The inclination distribution of SD objects is larger than that of the classical KB, but generally limited to $i \leq 30°$. These objects originate in the classical KB: with pericenter just outside the orbit of Neptune their orbits evolved on timescales of Gyr through repeated long distance interactions with Neptune (Duncan & Levison, 1997).

With larger inclination and eccentricity distribution than the SD, and extending farther out in the outer solar system, the origin of the ESD is not certain. We generally classify object as ESD objects if $q \geq 38$ AU, thus decoupling them from Neptune. Mechanisms involving mean-motion trapping in conjunction with Kozai chaos have been proposed (Gomes et al., 2005b; Volk & Malhotra, 2009), as well as early stellar encounters, to explain the evolution of planetesimals from the KB or SD into the ESD.

The long period comets that cross the inner solar system provide observational evidence of the existence of an isotropic family of objects extending farther out in the solar system. The Oort cloud formed as gravitational interactions with the giant planets pushed the aphelia of planetesimals from the SD into the region of influence of the Galactic tide ($a \geq 3,000$ AU, Duncan et al. 1987). The Oort cloud comprises two distinct structures: the inner Oort cloud, extending to $20,000$ AU, and the outer Oort cloud, a spherical structure extending as far out as tens of thousands of AU. The long period comets originate from the latter, when the orbit of and Oort cloud object, being far from the influence of the Sun, is perturbed by star

passages. The outer Oort cloud is loosely bound to the Sun, thus a significant loss rate is to be expected; the inner Oort cloud should replenish the comets lost from the outer cloud, though mechanisms for this process are uncertain and might require interactions with external bodies (Brasser et al., 2006).

The discovery of Sedna (2003 VB_{12}, Brown et al. 2004) suggested the intriguing possibility of the existence of a distant population of objects with perihelia as close as a few hundred AU from the Sun, but that spend most of their time far from the region of dynamical influence of Neptune. Sedna ha s perihelion $q = 76.156$ AU, semi-major axis $a = 525.86$ AU, eccentricity $e = 0.855$ and inclination $i = 11.934°$. No mechanism yet has been found to place Sedna on its orbit without invoking the presence of an unobserved perturbing object: an unknown rogue planet or a passing star. Continuing direct and indirect surveys have detected no other object like Sedna (Schwamb et al. 2009, and references therein, Wang et al. 2009 – hereinafter W09).

Morbidelli & Levison (2004) have excluded scenarios where Sedna evolves to its current orbital parameters from the SD or KB under the tidal influence of a massive early cold trans-Neptunian disk. Similarly unlikely are scenarios where Sedna evolves under the influence of Neptune in an early phase when Neptune's orbit had a higher eccentricity. This scenario acts on time scales that are long, while Neptune today has a nearly circular orbit. Also this mechanism generates a larger number of objects in the $50 \leq a \leq 100$ AU, than $a \geq 100$ AU, while both the *detached* object that we know populates the region $a > 200$ AU (Sedna and 2000 CR_{105}). Gladman & Chan (2006) find that the presence of rogue planets in the trans-Neptunian region, ejected from the solar system on time scales of ~ 200 Myr, could raise the perihelia of the SD, thus generating an ESD, and it could also produce objects with large orbital inclinations like 2004 XR190, 2003 UB313, 2000 CR105,

and Sedna.

Another promising scenario sees the solar system forming in an embedded star cluster. The presence of passing stars may explain at once the orbit of Sedna (Morbidelli & Levison, 2004; Brasser et al., 2007; Kaib & Quinn, 2008), the replenishing rate of the outer Oort cloud and the truncation of the Classical KB at 50 AU (Brasser et al., 2007, and references therein).

Each one of these formation and evolution scenarios leaves a distinct mark in the dynamical characteristics of the outer solar system families. Disentangling the different scenario requires however that we further our observational knowledge. Probing these remote regions of the solar system may profoundly impact our understanding of solar system formation, revealing not only details of the interaction among early solar system objects, but as well details of the Sun's birth environment.

Occultation data from the TAOS, Taiwanese American Occultation Survey, have been used to set upper limits to the population of objects in Sedna-like orbits (W09). TAOS was designed to probe the Kuiper Belt population of objects smaller than the current observational limit (diameter $D \lesssim 10$ km). With simultaneous multi-telescope high cadence observations the data collected by TAOS allowed us to produce the strongest upper limits on the small end of the KBO population (Zhang et al., 2008; Bianco et al., 2009b).

Here we present an analysis in progress of 5×10^5 star hours of three-telescope 4 or 5 Hz observations collected between January 2005 and August 2009, data described in Chapter 3. These data, a substantially larger dataset than the one analyzed in W09, are being scanned to detect shallow flux drops affecting a few to a few tens consecutive data points simultaneously in all of our telescopes.

5.2 Search algorithm

The signature of an occultation of a bright star by a body at $\Delta = 100 - 1000$ AU, would appear in a TAOS lightcurve as a shallow flux drop affecting 5-50 consecutive points, depending on the relative velocity and size of the occulter, and possibly displaying prominent diffraction features. We want to scan our lightcurves looking for statistically significant deviations of the flux from the local baseline. We define two windows: a larger *baseline–window* W over which calculate our local mean, $\bar{f_W}$, and local standard deviation, σ_W, and a smaller *event–window* w, of size comparable to the duration of the events we are searching for. We select $W = 61$ time–stamps and $w = 11,\ 17$, and 21 time–stamps.

We first filter our lightcurves, subtracting from each point, i, the local mean $\bar{f_W}$ of the surrounding region, weighted by local the standard deviation σ_W:

$$\bar{f_W}\ (i) = \sum_{j=i-\frac{W}{2}}^{i-\frac{w}{2}} f_j + \sum_{j=i+\frac{w}{2}}^{i+\frac{W}{2}} f_j, \tag{5.1}$$

$$\sigma_W\ (i) = \sqrt{\frac{1}{W-w}\left(\sum_{j=i-\frac{W}{2}}^{i-\frac{w}{2}} \left(f_j - \bar{f_W}\right)^2 + \sum_{j=i+\frac{w}{2}}^{i+\frac{W}{2}} \left(f_j - \bar{f_W}\right)^2\right)}, \tag{5.2}$$

$$h(i) = \frac{f(i) - \bar{f_W}(i)}{\sigma_W(i)}; \tag{5.3}$$

$h(i)$ represents the deviation from the mean in a baseline–window W surrounding a potential event, but disregarding the central w time-stamps that would be impacted by the event itself. The deviation from the mean is here expressed in units of standard deviation σ_W, where σ_W is also calculated over the baseline–window W, disregarding the central w points.

For each event–window size we rank the new lightcurves $h(i)$ for each tele-

scope (A, B and D, see Chapter 3) from the lowest to the highest value, so that the time-stamp with largest deviation from the mean, where the flux is suppressed, would be ranked $r_i = 1$. This algorithm is similar to that used in W09, but it accounts for the non-stationary nature of the noise in our data. The algorithm we implemented here thus allows us to calculate exactly the p-value of each of our *rank triplet*: set of three ranks associated with the same time-stamp for our three telescopes. In absence of events, just like we did in Chapter 3.3.2, we can calculate the probability distribution of the quantity:

$$z(i) \;=\; -\ln \prod_{k=1}^{N_{\rm T}} \left(\frac{r_{ik}}{N_P} \right), \tag{5.4}$$

where $N_{\rm T}$ is the number of telescopes simultaneously observing the star, N_P the number of points in the lightcurve, and r_{ik} the rank of the i-th point in the lightcurve observed by telescope k, and we can compute the probability of a random variable Z arising from this distribution: $P(Z > z(i)) = \xi$. Given the number of points in our dataset we expect $\lesssim 0.2$ false positive events generated by noise fluctuations for a threshold $z_{\rm max} = 3.0 \times 10^{-11}$ (see Section 3.3.2).

Figure 5.1, top, shows occultation lightcurves of objects of $D = 10$ km (left) and $D = 5$ km (right) diameter at $\Delta = 400$ AU, occulting magnitude $R \sim 12$ stars. The bottom panel shows the quantity $z(i)$ for true star lightcurves implanted with the synthetic events shown above, for an event–window size $w = 10$. An event generated by an object as small as 5 or 10 km is obviously visible at $\Delta = 400$ AU. These objects are far beyond the limits of direct observations!

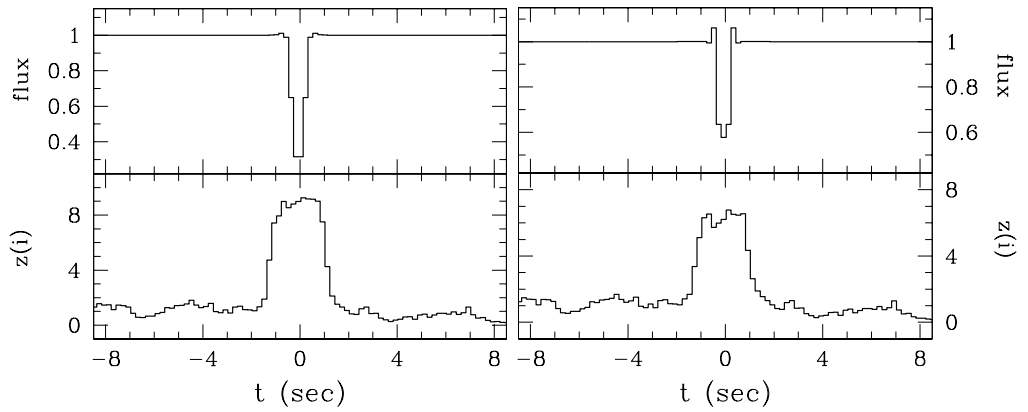

Figure 5.1: Top panel: occultation signature of a $D = 10$ km object (left) and a $D = 5$ km (right) object at $\Delta = 400$ AU occulting a magnitude $R \sim 12$ star. The impact parameter is assumed to be $b = 0$. Bottom panel: product of the ranks of the lightcurves of telescopes A, B, and D in the region implanted with the occultation.

5.3 Event rate calculation for Sedna-like objects

We are interested in assessing the density of objects in Sedna-like orbits. We will test our recovery efficiency for objects in the size range $1 \leq D \leq 30$ km, at distances of 100, 200, 300, 500 and 1000 AU.

For every diameter D and distance Δ in which we are interested, we want to calculate the expected event rate for our survey. This event rate will depend on the relative velocity $v_{\rm rel}(\epsilon, \Delta)$ of the occulter, where ϵ is the elongation of the occulter. To first approximation use Equation 1.8 to estimate the relative velocity of the occulter. This formula neglects the proper motion of the object. We plan on eventually including specific models for the orbital distribution of both Sedna-like and SD objects, thus introducing specific velocity distributions in our estimate of $v_{\rm rel}$.

For a given star lightcurve ($_*$), and an observing angle ϵ_*, we calculate the

expected event rate R_* of occultations as:

$$\frac{d^2R_*(D,\Delta)}{dD\,d\Delta} = \frac{d^2n(D,\Delta)}{dD\,d\Delta}\frac{v_{\rm rel}(\epsilon_*,\Delta)H_*(D,\Delta)}{\Delta^2}, \tag{5.5}$$

where $H_*(D,\Delta)$ is the event cross section, set to the diameter of the first Airy ring (see Nihei et al. 2007 and Section 1.3.1 of this work), and where $n(D,\Delta)$ is the number density of objects with diameter D at distance Δ, which is what we want to constrain based on the number of events detected by our survey.

The number of events expected for our survey is

$$\frac{d^2N_{\rm exp}(D,\Delta)}{dD\,d\Delta} = \sum_* \frac{d^2R_*(D,\Delta)}{dD\,d\Delta}\,E_*\,\eta_*(D,\Delta), \tag{5.6}$$

with E_* the exposure (the duration of the data run) and $\eta_*(D,\Delta)$ is the efficiency of recovery of objects of diameter D at distance Δ in the lightcurve we are analyzing, and the sum is conducted over all our lightcurves. Since we implant exactly one occultation – by an occulter of diameter D at distance Δ – in each one of our lightcurves, the efficiency of recovery assumes value of $\eta_* = 1$ if the event is recovered, or $\eta_* = 0$ if it is not. Denoting the fraction of lightcurves implanted with objects of diameter D with w_D, and with objects at distance Δ with w_Δ, Equation 5.6 takes the form:

$$\frac{d^2N_{\rm exp}(D,\Delta)}{dD\,d\Delta} = \frac{d^2n(D,\Delta)}{dD\,d\Delta}\frac{1}{w_D w_\Delta}\sum_{*,rec}\frac{v_{\rm rel}(\epsilon_*,\Delta)H_*(D,\Delta)E_*}{\Delta^2}, \tag{5.7}$$

where this time the sum is conducted only over the lightcurves with recovered events.

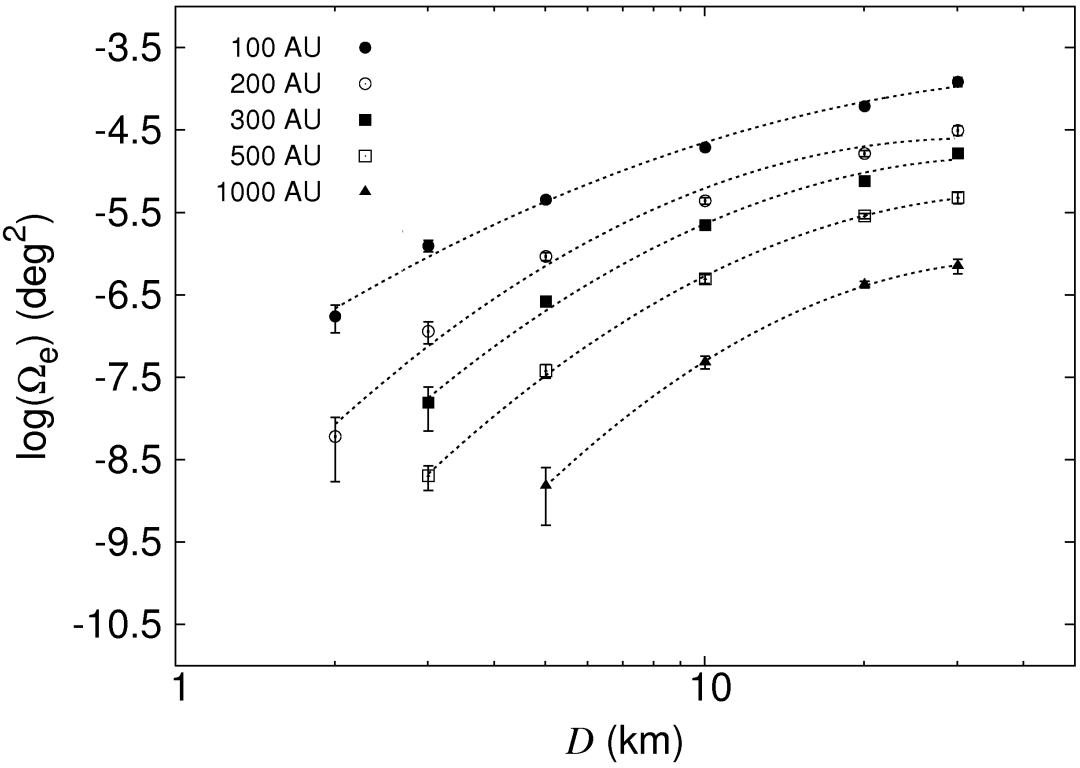

Figure 5.2: Minimum coverage of our survey: the coverage of W09 is projected to account for the increased exposure only.

As seen in Section 4.2 of this work then:

$$\Omega_{\rm e}(D,\Delta) = \frac{1}{w_D w_\Delta} \sum_{*}^{\rm rec} \frac{v_{\rm rel}(\epsilon_*,\Delta) H_*(D,\Delta) E_*}{\Delta^2} \tag{5.8}$$

is the effective coverage of our survey.

Compared to the W09 the exposure of our survey has increased by a factor 2.95. From preliminary tests we expect the modified search algorithm we use here to increase the efficiency of our search, but we are unable to precisely quantify this improvement at this time. Figure 5.2 shows our effective coverage as a function of diameter D separately for all Δ distances tested accounting for the increased exposure but ignoring the increase in efficiency.

5.4 Renewed limits to the Sedna population

In W09 we set upper limits to the population of Sedna-like objects. These limits are reproduced here accounting for the increased coverage of our present survey, but disregarding the expected increase in efficiency. These are therefore conservative upper limits to the Sedna population.

We derive constraints to the number density of Sedna-like objects separately for every distance Δ we tested. We have to assume a functional form for the diameter dependence: a *size distribution*. We assume a simple power law size distribution $n \propto D^{1-q}$ so that:

$$\frac{d\,n}{d\,D} = n_0(q-1)D^{-q}, \tag{5.9}$$

with n_0 the number of objects of diameter $D \geq 1$ km at distance Δ. We expect in our survey

$$N_{\rm exp}(\Delta) = n_0\,(q-1)\int_{D_{\rm min}}^{D_{\rm max}} D^{-q}\Omega_{\rm e}(D,\Delta)\,dD, \tag{5.10}$$

events from objects at distance Δ. Because we recovered *no events* we can exclude at 95% confidence level any value of q that predicts more then 3 events. For values of q ranging from $q = 3.0$ to $q = 6.0$ we thus set upper limits on the number density of objects at distance Δ in Figure 5.3: models above the plotted lines are excluded.

In W09 we derived a lower limit to the density of Sedna-like objects, based on the existence of Sedna: any value of q that predicts fewer than 0.05 objects larger than Sedna is excluded at the 95% confidence level. This correspond to a minimum number density of *Sednas* (i.e. objects larger than $D = 1600$ km at

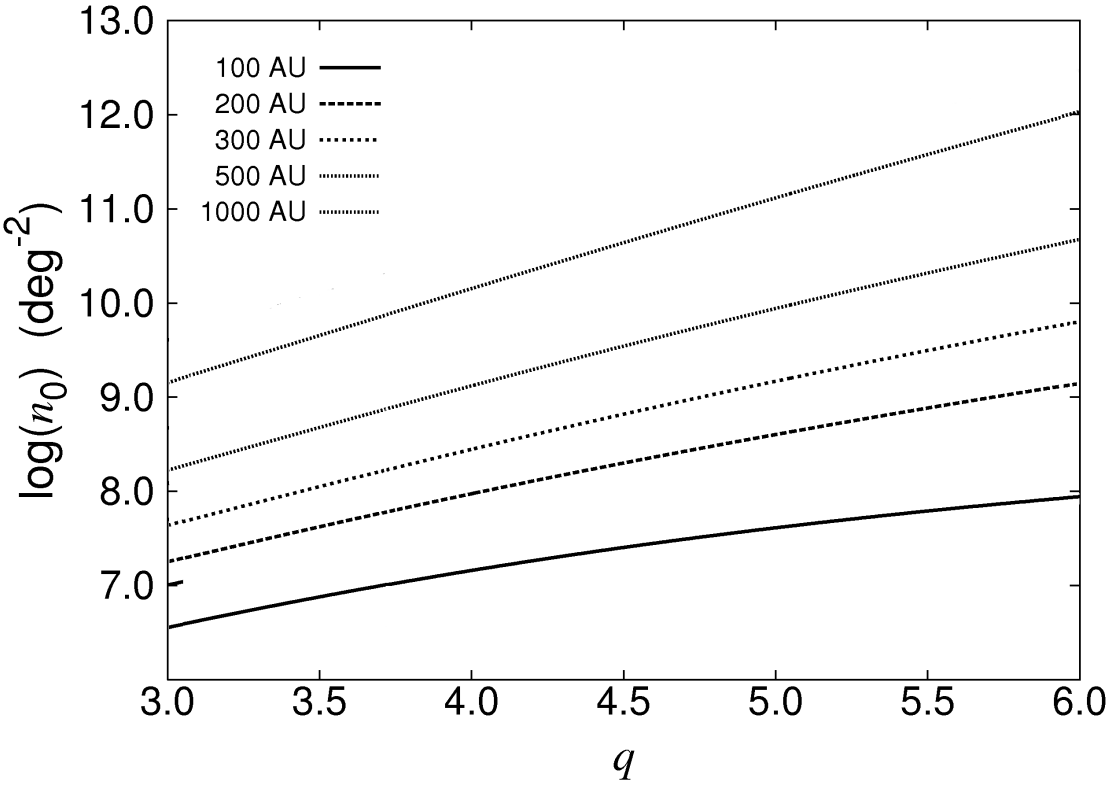

Figure 5.3: Maximum number density of $D \geq 1$ km objects as a function of the slope of a power law size distribution. Distances of 100, 200, 300, 500, and 1000 AU are assumed.

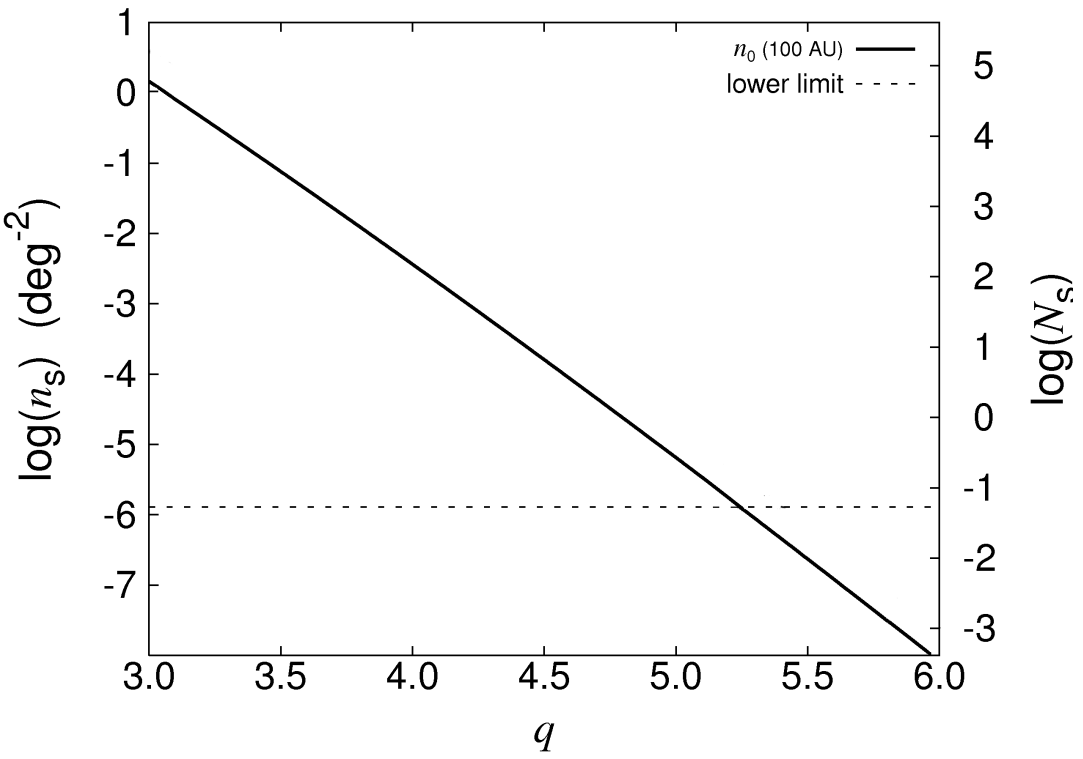

Figure 5.4: Maximum number of density (left axis) and absolute number (right axis) of objects *larger than Sedna* ($D \geq 1600$ km) as a function of the slope of a power law size distribution (solid line). The region above the line is excluded by the TAOS result. The lower limit set by the very existence of Sedna is also plotted (dashed line)

100 AU) $n_s < 1.2 \times 10^{-6}$ deg^{-2}. Combining this lower limit with our upper limits we can state that slopes $q > 5.2$ are excluded at 95% c.l. (see Figure 5.4).

5.5 Future work

So far we reproduced the work done in W09, taking advantage of our increased coverage. We expect to be able to derive more stringent limits due to the increased efficiency of our search algorithm. More interestingly, though, we want to include possible velocity and orbital distributions for both the Sedna-like and Scattered Disk objects.

Chapter 6

Conclusions

I collected and analyzed a large amount of data looking for serendipitous occultations of bright stars by objects in the outer solar system. Occultations would allow us to detect the presence of objects too small or too distant to be observed directly. I found no occultations by outer solar system objects in my datasets and I am able to set upper limits on the KBO population and some constraints on models of the formation and evolution of the outer solar system.

6.1 The MMT/Megacam Survey for small KBOs

I have devised a new observational method which allows fast photometry with large telescopes with standard CCD cameras. I am able to achieve high photometric rates (200 Hz) on tens of targets simultaneously. The data reduction techniques for this kind of data are still under development. The amplitude of the noise is typically larger than the Poisson noise, and it displays obvious deviations from normality. However, I proved this method is suitable for gathering a large amount of precision fast photometric data in few observing hours. I presented a result that lowers the upper limit set by similar occultation surveys by more than

one order of magnitude for KBOs $D \geq 1$ km, and I can push the upper limit to $D \geq 700$ m. I confirmed the result obtained by dedicated Kuiper belt occultation surveys.

The high speed sampling achieved with continuous readout mode will enable the resolution of the diffraction features of any candidate events, which is not possible with the TAOS project due to the lower sampling rate. This will allow us to set tight constraints on the physical characteristics of an occulting system, possibly breaking the degeneracy between impact parameter, size and distance for sub-km KBOs. Furthermore, continuous readout mode enables the simultaneous monitoring of as many as 100 stars, which is a distinct advantage over the surveys of Roques et al. (2006) and Bickerton et al. (2008), where only two stars can be sampled at a time.

This observational technique has proved useful in testing telescope performance and addressing guiding issues and it was used at the MMT to test the drive servos. Furthermore this observational method is a promising technique for ground-based high precision photometry of bright sources with large telescopes as it addresses many issues typically encountered in observing bright targets (Gillon et al., 2008). Saturation is avoided without resorting to refocusing, it involves no overhead due to readout and with a camera like Megacam, with a large field of view, it allows the observation of many stars at a time, guaranteeing the presence of a good number of comparison stars that can be used to achieve high precision relative photometry.

Further improvements in SNR might be achieved: I am exploring a fitting photometry package that uses the Expectation–Minimization algorithm, treating each row as a mixture of Gaussians, to better separate the contribution from different sources. A possible way to address the contamination due to unresolved sources is

to subtract the contribution from known unresolved sources (identified from the stare–mode image, see Section 2.3.1) using the trends identified in the de-trending phase (Section 2.3.1). Another possibility is to de-trend the lightcurves recursively, while allowing a variable phase offset. Finally, it shall be noticed that Megacam will become available for observations at the Magellan Clay Telescope, from where our target fields, at the intersection of the galactic and ecliptic plane, could be observed at a higher elevation. This would help reduce the noise introduced by cross contamination and differential image motion, as the atmospheric effects I encounter observing at high air masses would be reduced.

6.2 The TAOS KBO survey

I presented an analysis of 3.75 years of TAOS data, comprising 5×10^5 star–hours of three-telescope 4 or 5 Hz time series. I searched for occultations of our star targets by KBOs in order to constrain the size distribution of KBOs, particularly in the 1–to–10 km region, which is currently out of reach of direct observation surveys. I described the TAOS data and analyzed the dependence of the efficiency of event recovery on various parameters. Occultations near opposition lead to a higher event rate for TAOS, even after taking into account the increased recovery efficiency for small objects where the angle from opposition is larger and the relative velocity of the KBOs is lower. The largest number of recoveries is obtained for a stellar magnitude $M_{\rm TAOS} \sim 12.5$. Although this magnitude is close to the limiting magnitude of the survey, the abundance of $M_{\rm TAOS} \sim 12.5$ stars in the TAOS fields compensates for the increased SNR, and thus detectability, for brighter targets.

I found no occultation events in our data. This allowed me to set upper limits to the number density of KBOs that are stringent enough to be compared

with the most popular models for the formation and evolution of the Kuiper belt. I considered three theoretical models, Pan & Sari (2005, hereinafter PS05), Kenyon & Bromley (2004, hereinafter KB04), and recent simulations by Benavidez & Campo Bagatin (2009, hereinafter BCB09), all of which describe the present size distribution of the Kuiper belt and I set constraints on these models. This is the first comparison of occultation data with model results.

Our result, particularly when compared with PS05 and KB04, suggests that the Kuiper belt is populated by fragile bodies, and that the effect of the migration of Neptune played an important role in its formation. The models described by BCB09 incorporate specific fragmentation prescriptions (Farinella et al., 1982; Benz & Asphaug, 1999) but do not include a model for Neptune's stirring. The BCB09 models depend on assumptions on the initial conditions: the location of the first break in the power law distribution for large objects and the slope of the power law. With the initial conditions used by the authors ($D_{\rm b} = 100$ km and $q_{\rm L} = 4.0$) TAOS allows all four models presented in BCB09.

Using a simple parametric model, where the size distribution is described by three consecutive power laws, and fixing the slope on the large end size and the location of the first break to the best fit from direct observations ($q_{\rm L} = 4.25$ km, $D_{\rm b1} = 75$ km), and the slope of the small side to that expected from a collisionally evolved strength-dominated population ($q_{\rm s} = 3.5$) I can constrain together the intermediate slope $q_{\rm I}$ and the location of the second break $D_{\rm b2}$, as shown in Figure 4.8. As direct surveys are currently not sensitive to KBOs smaller than $D \sim$ 28 km the TAOS occultation data can for the very first time probe this region of the size spectrum.

I also considered the Jupiter Family Comets. Assuming the JFCs are injected into their present orbits from one of the Kuiper belt populations, Classical Belt, Plutinos, or from the scattered disk, I compared the upper limit derived from

our survey to the estimates of the number of objects derived using the number of JFCs respectively by Levison & Duncan (1997) for a population of cometary precursors entirely in the CB, that of Morbidelli (1997) for Plutinos and of Volk & Malhotra (2008) for a progenitor population in the scattered disk. I can rule out the CB as unique precursor family if the progenitors are $D \geq 3$ km. This preliminary result confirms that occultation surveys can help understanding the origin of JFCs.

TAOS has operated for now over four years observing continuously with three, and now four, 50 cm aperture telescopes. TAOS is only marginally sensitive to sub-km KBO occultations, but we were able to prove that the low sensitivity at sub-km sizes is more than compensated for by the vast exposure of which TAOS is capable.

6.3 The TAOS Sedna and Scattered Disk Survey

The TAOS data is a great resource for probing regions of the outer solar system that are too distant to allow direct detections. At the distance of the scattered disk, extended scattered disk, and Oort cloud, objects as large as even thousands of kilometers would elude direct detection, while occultation have the potential of reaching these remote regions. We are scanning the dataset described in Chapter 3 searching for shallow flux drops affecting several consecutive points, compatible with occultations by objects in orbit between 100 and 1000 AU. We detected no such events in our data.

This work reproduces what was presented by the TAOS collaboration in Wang et al. (2009) with two major improvements. The dataset we analyze here is larger by a factor of ~ 3 than the dataset analyzed in Wang et al. (2009). We upgraded the search algorithm used in Wang et al. (2009). The algorithm we use

here accounts for non stable noise characteristics of our time series and thus it allows us to exactly calculate the probability of a particular configuration of flux values in our lightcurves. Furthermore we expect an increase in recovery efficiency. At this time we are able to estimate a lower limit to our improvement of the result published in Wang et al. (2009).

We want to include realistic models for the distribution of scattered disk objects, and objects in Sedna-like orbits thus possibly setting constraints on the genesis of the orbit of Sedna and on the early evolution of the solar system.

Bibliography

Asphaug, E. & Benz, W. 1996, Icarus, 121, 225

Bailey, M. E. 1976, Nature, 259, 290

Barucci, M. A., Belskaya, I. N., Fulchignoni, M., & Birlan, M. 2005, AJ, 130, 1291

Batten, A. H. 1981, JRASC, 75, 29

Benavidez, P. G. & Campo Bagatin, A. 2009, Planetary and Space Science, 57, 201

Benz, W. & Asphaug, E. 1999, Icarus, 142, 5

Bernstein, G. M. et al. 2004, AJ, 128, 1364

Bertin, E. & Arnouts, S. 1996, A&AS, 117, 393

Bianco, F. B., Protopapas, P., McLeod, B. A., Alcock, C. R., Holman, M. J., & Lehner, M. J. 2009a, AJ, 138, 568

Bianco, F. B. et al. 2009b, AJ, accepted

Bickerton, S. J., Kavelaars, J. J., & Welch, D. L. 2008, AJ, 135, 1039

Bickerton, S. J., Welch, D. L., & Kavelaars, J. J. 2009, AJ, 137, 4270

Born, M. & Wolf, E. 1980, Principles of optics. Electromagnetic theory of propagation, interference and diffraction of light (Oxford: Pergamon Press, 1980, 6th corrected ed.)

Brasser, R., Duncan, M. J., & Levison, H. F. 2006, Icarus, 184, 59

—. 2007, Icarus, 191, 413

Brown, M. E. 2001, AJ, 121, 2804

Brown, M. E., Trujillo, C., & Rabinowitz, D. 2004, ApJ, 617, 645

Brown, M. E., Trujillo, C. A., & Rabinowitz, D. L. 2005, ApJ, 635, L97

Chang, H.-K., Liang, J.-S., Liu, C.-Y., & King, S.-K. 2007, MNRAS, 378, 1287

Chang, H.-K. et al. 2006, Nature, 442, 660

Charnoz, S. & Morbidelli, A. 2007, Icarus, 188, 468

Cutri, R. M. et al. 2003, 2MASS All Sky Catalog of point sources. (IPAC, Pasadena)

Davis, D. R. & Farinella, P. 1997, Icarus, 125, 50

Dohnanyi, J. W. 1969, J. Geophys. Res., 74, 2531

Dravins, D., Lindegren, L., Mezey, E., & Young, A. T. 1997, PASP, 109, 173

—. 1998, PASP, 110, 610

Duncan, M., Quinn, T., & Tremaine, S. 1987, AJ, 94, 1330

Duncan, M. J. & Levison, H. F. 1997, Science, 276, 1670

Duncan, M. J., Levison, H. F., & Budd, S. M. 1995, AJ, 110, 3073

Farinella, P., Paolicchi, P., & Zappala, V. 1982, Icarus, 52, 409

Fraser, W. C. & Kavelaars, J. J. 2008, Icarus, 198, 452

—. 2009, AJ, 137, 72

Fraser, W. C., Kavelaars, J. J., Holman, M. J., Pritchet, C. J., Gladman, B. J., Grav, T., Jones, R. L., Macwilliams, J., & Petit, J.-M. 2008, Icarus, 195, 827

Fuentes, C., Holman, M. J., Trilling, D. E., & Protopapas, P. 2009a, in AAS/Division for Planetary Sciences Meeting Abstracts, Vol. 41, AAS/Division for Planetary Sciences Meeting Abstracts, 62.08

Fuentes, C. I., George, M. R., & Holman, M. J. 2009b, ApJ, 696, 91

Fuentes, C. I. & Holman, M. J. 2008, AJ, 136, 83

Gillon, M., Anderson, D. R., Demory, B. ., Wilson, D. M., Hellier, C., Queloz, D., & Waelkens, C. 2008, ArXiv e-prints, 806

Gladman, B. & Chan, C. 2006, ApJ, 643, L135

Gladman, B., Marsden, B. G., & Vanlaerhoven, C. 2008, Nomenclature in the Outer Solar System, ed. B. H. C. D. P. . M. A. Barucci, M. A., 43–57

Gomes, R., Levison, H. F., Tsiganis, K., & Morbidelli, A. 2005a, Nature, 435, 466

Gomes, R. S., Gallardo, T., Fernández, J. A., & Brunini, A. 2005b, Celestial Mechanics and Dynamical Astronomy, 91, 109

Holman, M. J. & Wisdom, J. 1993, AJ, 105, 1987

Jewitt, D. 2003, Earth Moon and Planets, 92, 465

Jewitt, D., Luu, J., & Trujillo, C. 1998, AJ, 115, 2125

Jones, T. A., Levine, A. M., Morgan, E. H., & Rappaport, S. 2008, ApJ, 677, 1241

Joye, W. A. & Mandel, E. 2003, in Astronomical Society of the Pacific Conference Series, Vol. 295, Astronomical Data Analysis Software and Systems XII, ed. H. E. Payne, R. I. Jedrzejewski, & R. N. Hook, 489–+

Kaib, N. A. & Quinn, T. 2008, Icarus, 197, 221

Kenyon, S. J. & Bromley, B. C. 2001, AJ, 121, 538

—. 2004, AJ, 128, 1916

Kenyon, S. J., Bromley, B. C., O'Brien, D. P., & Davis, D. R. 2008, Formation and Collisional Evolution of Kuiper Belt Objects, ed. M. A. Barucci, H. Boehnhardt, D. P. Cruikshank, & A. Morbidelli, 293–313

Kenyon, S. J. & Luu, J. X. 1999a, AJ, 118, 1101

—. 1999b, ApJ, 526, 465

Kenyon, S. J. & Windhorst, R. A. 2001, ApJ, 547, L69

Kim, D.-W., Protopapas, P., Alcock, C., Byun, Y.-I., & Bianco, F. 2008, ArXiv e-prints, 812

Lehner, M. J. et al. 2009a, in preparation

—. 2009b, PASP, 121, 138

Leinhardt, Z. M. 2008, Physical Effects of Collisions in the Kuiper Belt (Barucci, M. A. and Boehnhardt, H. and Cruikshank, D. P. and Morbidelli, A.), 195–211

Levison, H. F. & Duncan, M. J. 1997, Icarus, 127, 13

Levison, H. F., Morbidelli, A., Vanlaerhoven, C., Gomes, R., & Tsiganis, K. 2008, Icarus, 196, 258

Liang, C. L. et al. 2004, Statistical Science, II, 265

Liu, C.-Y., Chang, H.-K., Liang, J.-S., & King, S.-K. 2008, MNRAS, 388, L44

Lowry, S., Fitzsimmons, A., Lamy, P., & Weissman, P. 2008, Kuiper Belt Objects in the Planetary Region: The Jupiter-Family Comets (The Solar System Beyond Neptune), 397–410

Marsh, T. R. & Dhillon, V. S. 2006, in American Institute of Physics Conference Series, Vol. 848, Recent Advances in Astronomy and Astrophysics, ed. N. Solomos, 808–809

McLeod, B., Geary, J., Ordway, M., Amato, S., Conroy, M., & Gauron, T. 2006, in Scientific Detectors for Astronomy 2005, ed. J. E. Beletic, J. W. Beletic, & P. Amico, 337–+

Mink, D. 2006, in ASP Conf. Ser. 351: Astronomical Data Analysis Software and Systems XV, ed. C. Gabriel, C. Arviset, D. Ponz, & S. Enrique, 204–+

Monet, D. G. et al. 2003, AJ, 125, 984

Morbidelli, A. 1997, Icarus, 127, 1

Morbidelli, A. & Levison, H. F. 2004, AJ, 128, 2564

Morbidelli, A., Levison, H. F., & Gomes, R. 2008, The Dynamical Structure of the Kuiper Belt and Its Primordial Origin, ed. M. A. Barucci, H. Boehnhardt, D. P. Cruikshank, & A. Morbidelli, 275–292

Morbidelli, A., Levison, H. F., Tsiganis, K., & Gomes, R. 2005, Nature, 435, 462

Moro-Martin, A., Wyatt, M. C., Malhotra, R., & Trilling, D. E. 2007, ArXiv Astrophysics e-prints

Nihei, T. C. et al. 2007, AJ, 134, 1596

Nordgren, T. E., Lane, B. F., Hindsley, R. B., & Kervella, P. 2002, AJ, 123, 3380

Oort, J. 1950, Bull. Astron. Inst. Neth., 11, 91

Pan, M. & Sari, R. 2005, Icarus, 173, 342

Rice, J. A. 2006, Mathematical Statistics and Data Analysis, Second Edition (Duxbury Press)

Roques, F., Moncuquet, M., & Sicardy, B. 1987, AJ, 93, 1549

Roques, F. et al. 2006, AJ, 132, 819

Schenk, P. M. & Zahnle, K. 2007, Icarus, 192, 135

Schwamb, M. E., Brown, M. E., & Rabinowitz, D. L. 2009, ApJ, 694, L45

Smith, J. A. et al. 2002, AJ, 123, 2121

Stern, S. A. 1996, AJ, 112, 1203

Tancredi, G., Fernández, J. A., Rickman, H., & Licandro, J. 2006, Icarus, 182, 527

Tsiganis, K., Gomes, R., Morbidelli, A., & Levison, H. F. 2005, Nature, 435, 459

van Belle, G. T. 1999, PASP, 111, 1515

Volk, K. & Malhotra, R. 2008, ApJ, 687, 714

Volk, K. & Malhotra, R. 2009, in AAS/Division for Planetary Sciences Meeting Abstracts, Vol. 41, AAS/Division for Planetary Sciences Meeting Abstracts, 62.03

Wang, J. et al. 2009, AJ, 138, 1893

Write, M. 2007, Interdisciplinary Science Reviews, 32, 1

Young, A. T. 1967, AJ, 72, 747

Zhang, Z.-W. et al. 2008, ApJ, 685, L157

Zhang, Z. W. et al. 2009, PSAP accepted.